Smart Wing Stall Flutter Alleviation

Reza Moosavi*

School of Physics, Engineering & Computer Science

Department of Engineering & Technology

Centre for Engineering Research

University of Hertfordshire

Hertfordshire, Hatfield, AL10 9AB, UK

Abstract: One of classical aeroelastic phenomenon seriously affecting the performance of flexible wings at high angle of attack is stall flutter. This work shows that how the stall flutter phenomenon can be alleviated and eliminated using a small inductor by implementing a piezoelectric patch. The dynamic responses are calculated to analyze the nonlinear characteristics of the aeroelastic system. Parametric study has been performed for different parameters. The main contribution of this work is to represent a way to alleviate or eliminate the stall flutter on a regular 2D wing by using a passive aeroelastic control including piezoelectric patches and shunt circuits in which the size of the required inductance is small. The results indicate a considerable improvement in dynamic aeroelastic behavior of a 2D wing.

Keywords: Smart Wing, Stall Flutter, Piezoelectric Material

Nomenclature

I_α	mass moment of inertia
$\ddot{\alpha}$	pitching acceleration
C_α	pitching structural damping
$\dot{\alpha}$	pitching velocity
K_α	pitching structural stiffness
α	pitching angle

*Assistant Professor in Aerospace Engineering, m.moosavi@herts.ac.uk.ac

β_α	pitch electromechanical coupling
q_α	pitch electric charge
c_m	pitching moment coefficient
a	$a = x_f/b - 1$
x_f	elastic axis
b	half span
c_n	total lift coefficient
L_α	pitch inductance of piezoelectric material
$\ddot{q}_\alpha$	rate of the pitch electrical current
R_α	pitch resistance of piezoelectric material
$\dot{q}_\alpha$	pitch electrical current
$C_{p\alpha}$	pitch capacitance of piezoelectric material
x_p	piezoelectric axis
$x_1 - x_8$	aerodynamic states for unsteady attached flow
x_9	potential normal force coefficient time-delayed version c_n^p, when $x_9 > c_{n_1}$, there is leading edge separation
x_{10}	unsteady trailing edge separation point chordwise position
x_{11}	LEV lift
x_{12}	quasi-steady separation point location time-delayed version, which can affect only the LEV pitching moment
c	chord
α_F	wind-off equilibrium pitch angle
f_n	wind-off natural frequency
M	horizontal airflow Mach number

Δt	default time step
t_f	final time
ε	Runge-Kutta-Fehlberg tolerance
δ	event detection tolerance
ϵ	implicit tolerance
$\alpha(0)$	initial pitch angle
$\dot{\alpha}(0)$	initial pitch velocity

1. Introduction

Nowadays, green aircraft with zero emission is a major priority for the aerospace industry worldwide, which is more efficient, quieter, and cleaner, with low fuel consumption, pollutants emission, and operational costs. In this regard, to have low environmental impact and more sustainable flight, leading aerospace companies such as Airbus and Boeing are trying to study and design new aircraft with new configurations and characteristics [1]. Most of these advanced designs include more flexibility in aircraft structures. In some modern designs, in order to reduce induced drag, wings have long span and made of lighter materials to minimize overall weight, which cause more flexibility in the structure. Having more flexibility leads to sever aeroelastic behavior in the vehicle and strong coupling between aeroelastic behavior and flight dynamics [1, 2].

One of particular interest for aeroelastic investigations is the flutter phenomenon where there is a challenging problem as modeling post-flutter limit-cycle oscillation (LCO). Flutter is a common concern in dynamic aeroelasticity that can affect flight dynamics effectively. This happens when the combine structural and aerodynamics damping becomes negative leading to a self-induced oscillation on the structure. Having nonlinearities in the aerodynamics and structure can create LCO, which may lead to structural failure. Therefore, it is crucial to investigate their occurrence and effects in different flight phases.

The flutter phenomenon can be modeled with linear aerodynamic theories in the frequency domain such as Theodorsen and Garrick ones [3, 4] and in the time domain with Wagner's indicial solution [5]. Since LCOs are very nonlinear, these linear models cannot predict all possible LCOs and their features accurately. One way to fully predict LCOs is to perform extensive flight test, which is a time-consuming and expensive attempt. This problem can arise more in highly flexible aerospace structures like futuristic configurations and designs with large aspect ratio wings or High-Altitude Long Endurance (HALE). Hence, it is necessary to have a nonlinear aeroelastic model to predict all possible LCO aspects properly [6].

One of the very specific oscillations in highly flexible aerospace structures can be caused by dynamic stall. Dynamic stall can lead to stall flutter may seriously affect the performance of flexible wings, blades, and propellers at high angle of attack. The vibrations resulting from the fluid and structure interactions can create flutter phenomenon, which results divergent oscillations with exponentially increasing amplitude. Flow separation does not cause this kind of flutter and hence occurs more frequently [7]. Using linear potential flow theory, the pitch-plunge flutter velocities of two degrees of freedom system can be accurately predicted. However, stall flutter is a nonlinear dynamic aeroelasticity, which includes only one degree of freedom and dynamic large region boundary layer separation and reattachment, knowing as dynamic stall. The critical flutter velocity can be strongly under effect of the equilibrium angle of attack. It has been shown that stall hysteresis correction can help predict stall boundaries and it is possible to have stall flutter even in a purely pitching mode [8-10]. Due to the nonlinearity of unsteady aerodynamic loads, stall flutter may present different dynamic response at different angles of attack and velocities, such as bifurcation, chaotic motion, and multiple equilibrium states [11-14].

Aerodynamic nonlinearity in dynamic stall can make the critical velocity of stall flutter often lower than that of couple mode flutter. Creating a strong vortex close to the leading edge,

known as the dynamic stall vortex (DSV), can characterize dynamic stall [15-17]. Transient additional lift and considerable pitching moment fluctuation can be produced when the DSV moves downstream [18]. Then the trailing edge can be shed off, which can create full flow separation over the suction surface. Deep stall may induce pitching oscillation and energy absorbing from the fluid. LCO with constant amplitude can appear when there are equal energy harvested and dissipated by damping [19]. Many different response mechanisms of the flow induced vibration during deep stall can be analyzed determining the wake flow field diagrams of the trailing edge vortices and the leading edge DSVs [20]. The numerical simulations of dynamic stall results show that the strength, development, and shedding of the DSV can be directly affected by the amplitude angle, reduced frequency, equilibrium angle of attack, fluid flow Mach number, and rotation axis position [21].

Recently, by developing in structural materials rapidly, the aerospace structures become lightweight and more flexible leading to aggravate the destructiveness of stall flutter. Hence, it becomes more important to suppress the flutter amplitudes and delay the flutter boundaries. Since the main reason for stall flutter is the sever pitching moment fluctuation, it is necessary to investigate how to reduce the aerodynamic loads during dynamic stall [22, 23]. Design of highly flexible aerospace structures requires avoiding stall flutter; hence, it needs to predict dynamic stall airloads accurately. Accurate prediction of aeroelastic instabilities and flutter is very necessary in the performance of aerospace vehicles. To reduce design iterative procedure, it needs to perform aeroelastic simulations fast and inexpensively specially in rotary-wing airplanes, which include more complex aeroelastic behavior. An accurate model of the wing or airfoil section unsteady aerodynamic behavior is a prerequisite to any aeroelastic analysis. Implementing Computational Fluid Dynamics (CFD) for obtaining aerodynamic load and Finite Element Method (FEM) for structural dynamics can be expensive and it can require a

considerable run time for some cases even by using High Performance Computing (HPC) resources.

Having an effective system to control and suppress stall flutter can be a crucial element in the aeroelastic design of aerospace structures including fixed-wing and rotary-wing aircraft and flapping-wing micro air vehicle (MAV). The control methods can be passive or active according to requirement of external energy or not. Due to good adaptability of active control, it has been widely investigated. The open-loop control has been studied on the rotational oscillation effect on vortex shedding [24]. Using a rotating oscillating cylinder numerically, drag can effectively reduce [25]. Other open-loop control methods are blowing/suction [26, 27], a synthetic jet [28, 29], streamwise [30], transverse [31], distributed forcing [32], and moving surface boundary-layer [33, 34]. Because the open-loop control consumes large energy, the closed-loop control has been widely investigated due to stronger adaptive ability and low energy consumption. For feedback control, the optimal control [35, 36] and reduced order method [37-39] were used in the early stage. Recently, machine learning method is also implemented for feedback control [40-42]. However, in closed-loop method, control law design is not simple and it requires to be determined by researchers experience in many cases. Since passive control can be simple and low cost, it is used to study Vortex Induced Vibration (VIV). To reduce vibration and drag over a bluff body, different passive control methods are applied as surface modifications with roughness [43, 44], splitter plates [45-48], tripping wires [49, 50], grooves [51-53], Strakes [54], and shrouding [55]. Most passive control methods by changing geometry or the boundary layer characteristics suppress vibration and reduce drag.

Dynamic stall is the phenomenon of periodic separation and reattachment of the flow around a wing during free or forced oscillations. The dynamic stall main features include a) stall delay, a rapidly oscillating wing will stall when the instantaneous angle of attack is higher than the static stall angle, b) leading edge vortex, under certain conditions a large vortical structure is

shed near the leading edge and travels downstream over the airfoil's surface, c) reattachment, the flow can reattach if the instantaneous pitch angle reduces sufficiently.

The first complete dynamic stall models' comparison was carried out by Reddy and Kaza with application to two different aeroelastic systems including the Gormont, Gangwani and Bielawa model and ONERA model [56, 57]. The ONERA model has been applied to a cantilevered rectangular wing and the results have been compared to experimental ones by Dunn and Dugundji [58]. The Gangwani and Bielawa model has been used on a 2D pitching wing by Price and Keleris [59]. Using the ONERA model, the pitch-plunge wing linear aeroelastic stability has been studied by Tang and Dowell [60]. The pitch-plunge wing simulations combined with Gormont's dynamic stall model have been carried out by Li and Fleeter [61]. Using the ONERA model, a pitch-plunge wing in a pulsing free stream has been studied by axman and Venkatesan [62]. The ONERA model has been applied to a 2D blade under pitching and flap-edgewise oscillations by Sakar and Bijl [63]. The pitch-plunge wing has been simulated with Leishman-Beddoes aerodynamics by Galvanetto et al. [64] and a similar analysis for low Mach numbers using the Sheng et al. modification to the Leishman-Beddoes model has been carried out by Shao et al. [65, 66]. Dynamic stall models used by a lot of these authors undergo very complex bifurcations, leading to chaos in many times [59, 61-64]. However, these bifurcations do not necessarily happen in a physical flow because they were not verified against experimental results.

The Leishman-Beddoes model can provide the aerodynamic load coefficients as the normal force coefficient perpendicular to the chord, c_n, the tangential force coefficient along to the chord, c_c, and the pitching moment coefficient around the quarter chord, c_m. In the helicopter community, researchers use routinely the normal and chordwise forces instead of lift; in contrary of the airplane community which uses usually lift.

We consider a wing with NACA 0012 airfoil section forced to undergo pitch oscillations with an amplitude of 10˚ around a mean pitch angle of 12˚ with reduced frequency $k = 0.098$ at a Mach number of 0.3. To present a very specific problem as a 2D wing forced vibration, dynamic stall models were developed. The most validations of such model are about pitch oscillation around the quarter-chord. However, they have also been validated experimentally on linear pitch ramp and some other motions [67-69]. Implementing a semi-empirical dynamic stall model needs effectively an extrapolation since the model was neither developed nor validated for motions applied. Assuming the model can be able to present well sinusoidal pitching motion around the quarter chord, it can also be able to present well all other motions. Semi-empirical dynamic stall models are usually applied to the helicopter rotor blades aeroelasticity because of similarity of the rotor blades behavior to dynamic stall models due to implementing the entire blade sinusoidal motion by the blade root cyclic pitch. This work presents a new approach using small inductance was not previously presented in the literature for stall flutter alleviation and elimination.

2. Methodology

2.1. Smart Wing Dynamic Stall Aeroelastic Simulation

This study investigates the self-excited oscillations of a two-dimensional (2D) smart wing in uniform flow, as shown in Figure 1. The smart wing is free to pitch, α, about the elastic axis at a distance x_f from the leading edge. The pitch stiffness K_α is provided by a spiral spring and the pitch damping C_α is presented by a torsional damper. Using the Lagrange's equations and Kirchhoff's law, the smart wing equations of motion can be written as [66, 67, 70]

$$\begin{cases} I_\alpha \ddot{\alpha} + C_\alpha \dot{\alpha} + K_\alpha \alpha - \beta_\alpha q_\alpha = \frac{1}{2}\rho U^2 c^2 \left(c_m + \frac{1}{2}(a + 1/2) c_n \right) \\ L_\alpha \ddot{q}_\alpha + R_\alpha \dot{q}_\alpha + \frac{1}{C_{p\alpha}} q_\alpha - \beta_\alpha (x_f - x_p)\alpha = 0 \end{cases} \quad (1)$$

where its parameters are defined as below

Table 1 Parameters for smart wing equations of motion

I_α	Mass moment of inertia
$\ddot{\alpha}$	Pitching acceleration
C_α	Pitching structural damping
$\dot{\alpha}$	Pitching velocity
K_α	Pitching structural stiffness
α	Pitching angle
β_α	Pitch electromechanical coupling
q_α	Pitch electric charge
c_m	Pitching moment coefficient
a	$a = x_f/b - 1$
x_f	Elastic axis
b	Half span
c_n	Total lift coefficient
L_α	Pitch inductance of piezoelectric material
$\ddot{q}_\alpha$	Rate of the pitch electrical current
R_α	Pitch resistance of piezoelectric material
$\dot{q}_\alpha$	Pitch electrical current
$C_{p\alpha}$	Pitch capacitance of piezoelectric material
x_p	Piezoelectric axis

Assuming x_1 to x_{12} as the aerodynamic load states which are explained later and $x_{13} = \dot{\alpha}$, $x_{14} = \dot{q}_\alpha$, $x_{15} = \alpha$, and $x_{16} = q_\alpha$, Eq. (1) is written as first-order differential equations, as follows

$$\begin{cases} \dot{x}_{13} = -\dfrac{C_\alpha}{I_\alpha}x_{13} - \dfrac{K_\alpha}{I_\alpha}x_{15} + \dfrac{\beta_\alpha}{I_\alpha}x_{16} - \dfrac{1}{2}\rho U^2 c\, c_n/\cos\alpha \\ \dot{x}_{14} = -\dfrac{R_\alpha}{L_\alpha}x_{14} - \dfrac{1}{C_{p\alpha}L_\alpha}x_{16} + \dfrac{\beta_\alpha}{L_\alpha}(x_f - x_p)x_{15} + \dfrac{1}{2}\rho U^2 c(cc_m + b(a+1/2)c_n) \\ \dot{x}_{15} = x_{13} \\ \dot{x}_{16} = x_{14} \end{cases} \quad (2)$$

The new form of the equation of motion can be written

$$\dot{\mathbf{x}} = \mathbf{f}(\mathbf{x}, \dot{\mathbf{x}}) \quad (3)$$

because of having nonlinear function of $\ddot{\alpha}$.

3. Dynamic Stall Aerodynamic Model

In this work, the Leishman-Beddoes model has been applied to a general pitching aeroelastic smart structure by using the effective angle of attack $\bar{\alpha}$ as the angle between the total chordwise velocity and the total upwash at the quarter-chord, as follows [64, 70]

$$\bar{\alpha} = \tan^{-1}\left(\frac{U\sin\alpha + \dot{h}\cos\alpha - b(a+1/2)\dot{\alpha}}{U\cos\alpha - \dot{h}\sin\alpha}\right) \quad (4)$$

where U is the free-stream airspeed, α is the pitching angle, $\dot{h}$ is the plunge velocity, b is the half chord, $a = x_f/b - 1$, x_f elastic axis, and $\dot{\alpha}$ is the pitching velocity. In other words, using the angle of the triangle whose perpendicular sides are U_c and U_n, $\bar{\alpha}$ can be calculated as shown in Figure 1.

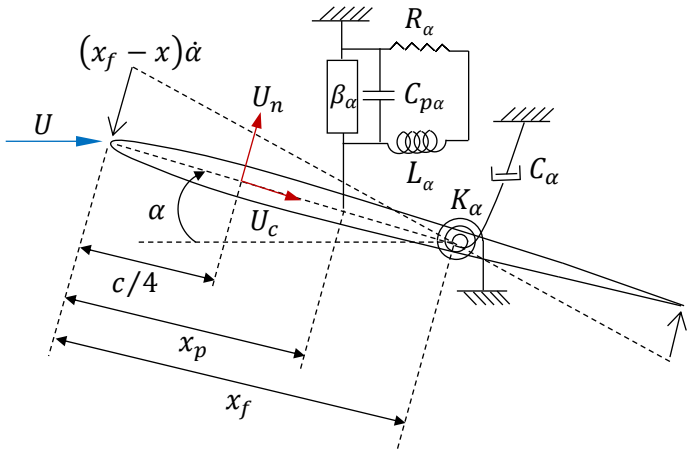

Fig. 1 A 2D smart wing with pitch DOF

The smart wing motion in the Leishman-Beddoes model is describes by $\bar{\alpha}(t)$ and the non-dimensional unsteady pitch rate $q = \dot{\bar{\alpha}}c/U$ where $\dot{\bar{\alpha}}$ is the time derivative of $\bar{\alpha}$ defined as

$$\dot{\bar{\alpha}} = \frac{1}{\tan^2 \bar{\alpha} + 1}\left[\frac{U\sin\alpha + \dot{h}\cos\alpha - b(a+1/2)\dot{\alpha}}{\left(U\cos\alpha - \dot{h}\sin\alpha\right)^2}\left(U\dot{\alpha}\sin\alpha + \ddot{h}\sin\alpha + \dot{h}\dot{\alpha}\cos\alpha\right)\right.$$

$$\left. + \frac{U\dot{\alpha}\cos\alpha + \ddot{h}\cos\alpha - \dot{h}\dot{\alpha}\sin\alpha - b(a+1/2)\ddot{\alpha}}{U\cos\alpha - \dot{h}\sin\alpha}\right] \tag{5}$$

Equation (3) can be written in first order form as

$$\dot{\mathbf{x}} = \mathbf{f}(\mathbf{x}, \dot{x}_{13}, \dot{x}_{14}) \tag{6}$$

where $\mathbf{x}$ is a 16×1 state vector including the 12 Leishman-Beddoes states, $x_{13} = \dot{\alpha}$, $x_{14} = \dot{q}$, $x_{15} = \alpha$, and $x_{16} = q$. The general form of the equations of motion can be represented

$$\boldsymbol{A}\ddot{\boldsymbol{y}} + \boldsymbol{C}\dot{\boldsymbol{y}} + \boldsymbol{E}\boldsymbol{y} = \boldsymbol{F} \tag{7}$$

where $\boldsymbol{A}$ the structural mass and inductance matrix, $\ddot{\boldsymbol{y}} = [\ddot{\alpha} \quad \ddot{q}]^T$ is the pitching acceleration and the rate of the pitch electrical current vector, $\boldsymbol{C}$ is the pitching structural damping and pitch resistance of piezoelectric material matrix, $\dot{\boldsymbol{y}} = [\dot{\alpha} \quad \dot{q}]^T$ is the pitching velocity and pitch electrical current vector, $\boldsymbol{E}$ is the pitching structural stiffness, pitch electromechanical coupling and pitch capacitance of piezoelectric material matrix, $\boldsymbol{y} = [\alpha \quad q]^T$ is the pitching angle and pitch electric charge vector, and $\boldsymbol{F}$ is the aerodynamic load vector. Moreover, $\boldsymbol{A}$, $\boldsymbol{C}$, and $\boldsymbol{E}$ matrices, and $\boldsymbol{F}$ vector are given by Eq. (A.)-(A.) in Appendix.

Considering Eqs. (A.28)-(A.31), the equations of motion, Eq. (7), can be written as

$$\begin{bmatrix}\dot{x}_{13}\\ \dot{x}_{14}\\ \dot{x}_{15}\\ \dot{x}_{16}\end{bmatrix} = \begin{bmatrix}-\boldsymbol{A}^{-1}\boldsymbol{C} & -\boldsymbol{A}^{-1}\boldsymbol{E}\\ \boldsymbol{I} & \boldsymbol{0}\end{bmatrix}\begin{bmatrix}x_{13}\\ x_{14}\\ x_{15}\\ x_{16}\end{bmatrix} + \frac{1}{2}\rho U^2 c\begin{bmatrix}-c_n/\cos\alpha\\ cc_m + b(a+1/2)c_n\\ 0\\ 0\end{bmatrix} \tag{8}$$

Because of the nonlinearity in $\dot{x}_{13}$ due to the nonlinearity in $\dot{\tilde{\alpha}}$, Eq. (5), as $\dot{x}_{13} = \dot{\tilde{\alpha}}$, Eq. (8) needs to be solved iteratively by considering the Runge-Kutta approach and using a simple implicit algorithm as follows,

1. The vectors $\mathbf{x}_i$ and $\dot{\mathbf{x}}_i$ are known at time instance t_i.
2. Substitute $\dot{x}_{13_i}$ in Eq. (6).
3. Evaluate the first guess $\mathbf{x}_{i+1,0}$ and $\dot{\mathbf{x}}_{i+1,0}$ using the Runge-Kutta method.
4. Calculate $J = \left| x_{13_{i+1,0}} - x_{13_i} \right|$ as a convergence criterion.
5. The solution has convergence if $J < \epsilon$, where $\epsilon \ll 1$. Increment i and return to step 1.
6. If $J > \epsilon$, substitute $x_{13_{i+1,0}}$ into Eq. (6) and return to step 3 to calculate the second guess $\mathbf{x}_{i+1,1}$ and $\dot{\mathbf{x}}_{i+1,1}$. Keep repeating until having convergence.

4. Numerical Examples

Consider a smart wing with a pitch degree of freedom and the following characteristics. Previously, there were practical limits in the low frequency range like the one typically existing in aeroelastic phenomena due to the large required inductance in passive aeroelastic control. However, nowadays, it is possible to have a small inductor integrated into a piezopatch dedicated to aeroelastic control [71]. Since standard inductors usually have too large internal resistance for resonant shunt application, they are not a practical component to integrate into a piezopatch. Implementing closed magnetic circuits with high permeability materials allows the design of large inductance inductors with high quality factors.

Table 2 Smart wing characteristics for modal analysis

$c = 0.637$ m	Chord
$x_f = c/3$	Pitch axis
$K_\alpha = 2500$ N/rad	Rotational spring stiffness
$\alpha_F = 10°$	Wind-off equilibrium pitch angle

$f_n = 5$ Hz	Wind-off natural frequency
$M = 0.3$	Horizontal airflow Mach number
$e_\alpha = 7.55 \times 10^{-3}$ C/m	Pitch coupling coefficient of piezoelectric material
$C_{p\alpha} = 34 \times 10^{-10}$ F	Pitch capacitance of piezoelectric material
$L_\alpha = 0.01$ H	Pitch inductance of piezoelectric material
$R_\alpha = 10\ \Omega$	Pitch resistance of piezoelectric material

The pizopatch characteristics as e_α, $C_{p\alpha}$, L_α, and R_α are determined by the experience from the author's previous work on smart wing flutter suppression [72-74] and some try and error process to find optimal values for each of them. The airfoil of the wing is NACA 0012 and its natural frequency is $\omega_n = 2\pi f_n = 10\pi$, the moment of inertia around the pitch axis is $I_\alpha = K_\alpha/\omega_n^2 = 2.533$ N/s^2. A light structural damping with coefficient $c_\alpha = K_\alpha/1000$ has be considered in the system.

Example 1 Smart wing modal analysis

As the first example, we conduct a linear eigen or modal analysis to the system and show its frequencies and mode shapes with and without the pizopatch, as follows.

The smart wing equations of motion in free vibrations are given

$$\begin{cases} I_\alpha \ddot{\alpha} + C_\alpha \dot{\alpha} + K_\alpha \alpha - \beta_\alpha q_\alpha = 0 \\ L_\alpha \ddot{q}_\alpha + R_\alpha \dot{q}_\alpha + \dfrac{1}{C_{p\alpha}} q_\alpha - \beta_\alpha (x_f - x_p)\alpha = 0 \end{cases} \tag{9}$$

where the parameters are defined as before. Equation (9) can be written as first-order differential equations by assuming $x_1 = \dot{\alpha}$, $x_2 = \dot{q}_\alpha$, $x_3 = \alpha$, and $x_4 = q_\alpha$

$$\begin{cases} \dot{x}_1 = -\dfrac{C_\alpha}{I_\alpha} x_1 - \dfrac{K_\alpha}{I_\alpha} x_3 + \dfrac{\beta_\alpha}{I_\alpha} x_4 \\ \dot{x}_2 = -\dfrac{R_\alpha}{L_\alpha} x_2 - \dfrac{1}{C_{p\alpha} L_\alpha} x_4 + \dfrac{\beta_\alpha}{L_\alpha} (x_f - x_p) x_3 \\ \dot{x}_3 = x_1 \\ \dot{x}_4 = x_2 \end{cases} \tag{10}$$

Equation (10) can be rewritten by considering $\boldsymbol{q} = [I_\alpha \quad C_\alpha \quad K_\alpha \quad \beta_\alpha \quad L_\alpha \quad C_{p\alpha} \quad R_\alpha]^T$ and $\mathbf{x} = [x_1 \quad x_2 \quad x_3 \quad x_4]^T$, as follows

$$\dot{\mathbf{x}} = \mathbf{f}(\mathbf{x}, \boldsymbol{q}) = \begin{bmatrix} -\frac{C_\alpha}{I_\alpha} x_1 - \frac{K_\alpha}{I_\alpha} x_3 + \frac{\beta_\alpha}{I_\alpha} x_4 \\ -\frac{R_\alpha}{L_\alpha} x_2 - \frac{1}{C_{p\alpha} L_\alpha} x_4 + \frac{\beta_\alpha}{L_\alpha}(x_f - x_p) x_3 \\ x_1 \\ x_2 \end{bmatrix} \tag{11}$$

where **f** are linear functions, x_1, x_2, x_3, and x_4 are the smart wing states and denote the system's pitching velocity, pitching angle, pitch electrical current, and pitch electric charge responses, respectively. There are four eigenvalues for the single DOF system that indicate the stability of the fixed point. One can obtain the fixed point of the system by solving

$$\mathbf{f}(\mathbf{x}, \boldsymbol{q}) = \mathbf{0} \tag{12}$$

or, equivalently,

$$\dot{\mathbf{x}} = \mathbf{0} \tag{13}$$

Using Eq. (11), it is possible to write Eq. (13) as

$$\dot{\mathbf{x}} = \boldsymbol{A}(\boldsymbol{q})\mathbf{x} \tag{14}$$

where

$$\boldsymbol{A} = \begin{bmatrix} -\frac{C_\alpha}{I_\alpha} & 0 & -\frac{K_\alpha}{I_\alpha} & \frac{\beta_\alpha}{I_\alpha} \\ 0 & \frac{\beta_\alpha}{L_\alpha}(x_f - x_p) & -\frac{R_\alpha}{L_\alpha} & -\frac{1}{C_{p\alpha} L_\alpha} \\ 1 & 0 & 0 & 0 \\ 0 & 1 & 0 & 0 \end{bmatrix} \tag{15}$$

The solution of Eq. (15) can be given [70]

$$\mathbf{x}(t) = \sum_{i=1}^{n} \mathbf{v}_i e^{\lambda_i t} b_i \tag{16}$$

where $\mathbf{v}_i$ is the *i*th eigenvector of $\boldsymbol{A}$, λ_i is the *i*th eigenvalue of $\boldsymbol{A}$, and b_i is the *i*th element of $\boldsymbol{b} = \boldsymbol{V}^{-1}\mathbf{x}_0$, where $\boldsymbol{V}$ is eigenvector of $\boldsymbol{A}$ and $\mathbf{x}_0$ is the initial condition.

The smart wing characteristics are the same mentioned before. In addition, the initial conditions are given as $x_1(0) = 0$ deg/s, $x_2(0) = 0$ A, $x_3(0) = 0.1$ deg, and $x_4(0) = 0$ C. The system response of the smart wing is depicted in Figure 2. The solid line represents the pitching angle of the smart wing and the dashed line shows the pitching angle of the corresponding regular wing. It is clear that the smart wing oscillation can be damped very smoothly in only three period however, the regular wing oscillation can be damped very sharply during many sharp oscillations.

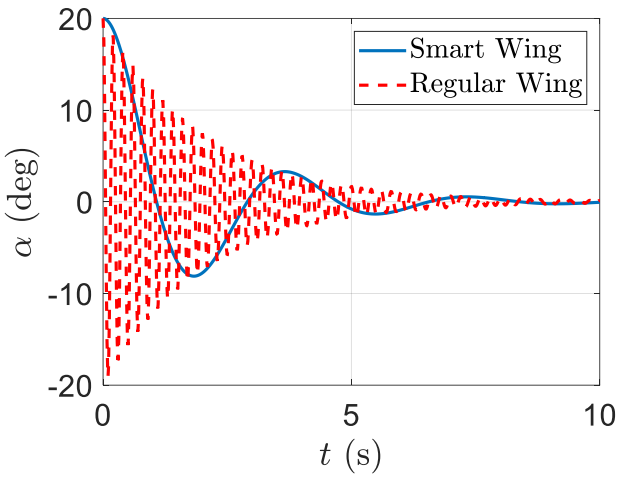

Fig. 2 Pitch angle time response in modal analysis

In addition, the phase plane plot for the pitching velocity and angle has been shown in Figure 3 where the point $(0,0)$ evokes the system trajectory. The initial pitching angle and velocity is the start point of the smart wing trajectory at the far right and the trajectory is turning to the fixed point, $\mathbf{x}_F = \mathbf{0}$, where is the center of the phase plane $(0,0)$.

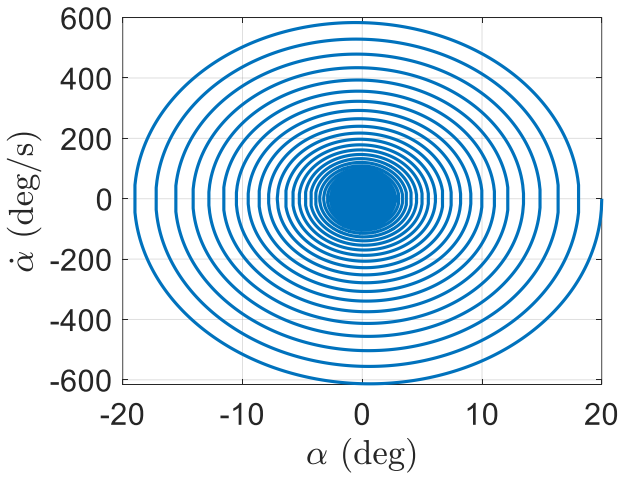

Fig. 3 Phase plane for the pitching velocity and angle in modal analysis

Also, the initial conditions for the electric charge and current which are zeros is the start point for the phase plane for the electrical current and charge. The trajectory is twisting out counter-clockwise until reaching to its maximum values after that it is turning towards the start point (0,0), as indicated in Figure 4.

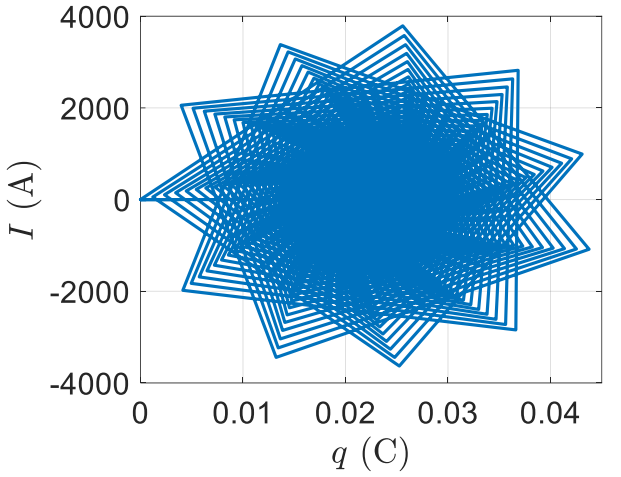

Fig. 4 Phase plane for the electrical current and charge in modal analysis

Example 2 Smart wing bifurcation analysis

In second example, a linear bifurcation analysis about static equilibrium (flutter) is conducted with and without piezo dampener. The differential equations of motion are as follows,

$$\begin{cases} \left(I_\alpha + \rho\pi b^4(1/8 + a^2)\right)\ddot{\alpha} + \left(C_\alpha + 2\rho U\pi b^3 a(a - 1/2)\right)\dot{\alpha} \\ \qquad +\left(K_\alpha + 2\rho U^2\pi b^2 a(a + 1/2)\right)\alpha - \beta_\alpha q_\alpha = 0 \\ L_\alpha\ddot{q}_\alpha + R_\alpha\dot{q}_\alpha + \dfrac{1}{C_{p\alpha}}q_\alpha - \beta_\alpha(x_f - x_p)\alpha = 0 \end{cases} \tag{17}$$

where its parameters are defined in Table 1 and ρ is the air density. For convenience, Eq. (17) can be written as

$$\begin{cases} m\ddot{\alpha} + d\dot{\alpha} + k\alpha - \beta_\alpha q_\alpha = 0 \\ L_\alpha\ddot{q}_\alpha + R_\alpha\dot{q}_\alpha + \dfrac{1}{C_{p\alpha}}q_\alpha - \beta_\alpha(x_f - x_p)\alpha = 0 \end{cases} \tag{18}$$

where $m = I_\alpha + \rho\pi b^4(1/8 + a^2)$, $d = C_\alpha + 2\rho U\pi b^3 a(a - 1/2)$, and $k = K_\alpha + 2\rho U^2\pi b^2 a(a + 1/2)$. Equation (18) is the equations of motion of a simple unforced Duffing oscillator that is very often used in dynamics literature. We can express it in first order

$$\dot{\mathbf{x}} = \mathbf{f}(\mathbf{x}, \dot{\mathbf{x}}) \tag{19}$$

where $x_1 = \dot{\alpha}$, $x_2 = \dot{q}_\alpha$, $x_3 = \alpha$, $x_4 = q_\alpha$, and

$$\mathbf{f}(\mathbf{x}, \dot{\mathbf{x}}) = \begin{pmatrix} -\dfrac{d}{m}x_1 - \dfrac{k}{m}x_3 - \dfrac{\beta_\alpha}{m}x_4 \\ -\dfrac{R_\alpha}{L_\alpha}x_2 - \dfrac{1}{L_\alpha C_{p\alpha}}x_4 - \dfrac{\beta_\alpha}{L_\alpha}(x_f - x_p)x_3 \\ x_1 \\ x_2 \end{pmatrix} \tag{20}$$

The fixed points of the system are obtained by $\mathbf{f}(\mathbf{x}, \dot{\mathbf{x}}) = 0$, which yields $x_1 = 0$ and $x_3 = 0$. Equation (20) can be written as

$$\dot{\mathbf{x}} = \mathbf{f}(\mathbf{x}, \dot{\mathbf{x}}) \approx \boldsymbol{A}_1\mathbf{x} \tag{21}$$

where

$$\boldsymbol{A}_1 = \begin{bmatrix} -\dfrac{d}{m} & 0 & -\dfrac{k}{m} & -\dfrac{\beta_\alpha}{m} \\ 0 & -\dfrac{R_\alpha}{L_\alpha} & -\dfrac{\beta_\alpha}{L_\alpha}(x_f - x_p) & -\dfrac{1}{L_\alpha C_{p\alpha}} \\ 1 & 0 & 0 & 0 \\ 0 & 1 & 0 & 0 \end{bmatrix} \tag{22}$$

The eigenvalues of matrix $\boldsymbol{A}_1$ in Eq. (22) shows the stability of the $\mathbf{x}_F$ fixed point. We consider the same smart wing with characteristics as Table 2 and air density of $\rho = 1.225\ \mathrm{kg/m^3}$ and as the airspeed is changing, we evaluate the position and stability of the fixed points. At the critical airspeed, $\mathbf{x}_F$ is on the point of becoming unstable, as shown in Figure 5. For the smart wing, stable fixed points are indicated by a solid blue line and unstable ones by a solid black line. However, for the regular wing, stable fixed points are denoted by a dashed red line and unstable ones by a dashed green line. A pitchfork bifurcation is occurring at $U = 1166\ \mathrm{m/s}$, as shown in Figure 5 by a blue circle for the smart wing and red triangle for the regular wing. It is clear adding the piezopatch does not affect the bifurcation of the smart wing compared to the regular one.

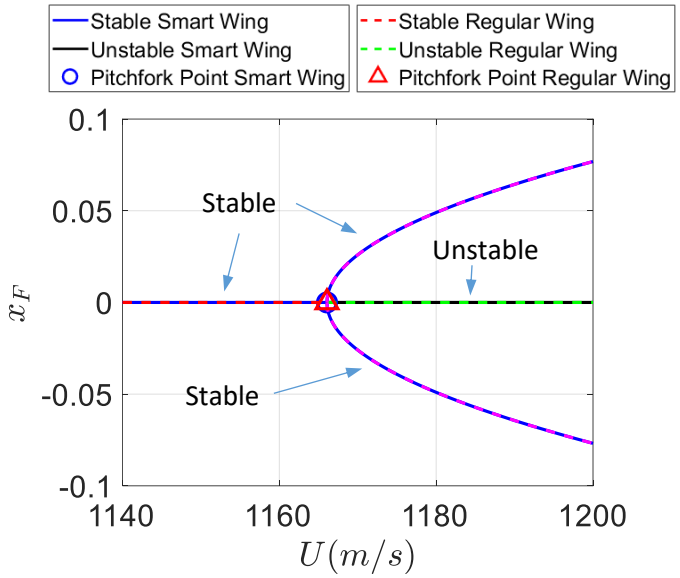

Fig. 5 Bifurcation analysis

Example 3 Smart wing stall flutter alleviation

In third example, we conduct an aeroelastic analysis on the following smart wing, Table 3, to represent the effect of the piezoelectric patch on stall flutter alleviation.

Table 3 Smart wing characteristics for flutter alleviation

$c = 0.637$ m	Chord

$x_f = c/3$	Pitch axis
$K_\alpha = 2500\ \mathrm{N/rad}$	Rotational spring stiffness
$\alpha_F = 10°$	Wind-off equilibrium pitch angle
$f_n = 5\ \mathrm{Hz}$	Wind-off natural frequency
$M = 0.3$	Horizontal airflow Mach number
$e_\alpha = 1.4465 \times 10^{-1}\ \mathrm{C/m}$	Pitch coupling coefficient of piezoelectric material
$C_{p\alpha} = 105 \times 10^{-8}\ \mathrm{F}$	Pitch capacitance of piezoelectric material
$L_\alpha = 0.01\ \mathrm{H}$	Pitch inductance of piezoelectric material
$R_\alpha = 10\ \Omega$	Pitch resistance of piezoelectric material

Using the Runge-Kutta-Fehlberg approach and event detection, one can solve the implicit scheme by considering the following parameters in Table 4

Table 4 Runge-Kutta-Fehlberg Parameters

$\Delta t = 2 \times 10^{-4}\ \mathrm{s}$	Default time step
$t_f = 2\ \mathrm{s}$	Final time
$\varepsilon = 0.1$	Runge-Kutta-Fehlberg tolerance
$\delta = 10^{-16}$	Event detection tolerance
$\epsilon = 10^{-6}$	Implicit tolerance
$\alpha(0) = 20°$	Initial pitch angle
$\dot{\alpha}(0) = 0$	Initial pitch velocity

Note that the aerodynamic states initial values are unknowns, and they cannot be considered all as zero. For instance, x_{10} and x_{12} represent the separation point positions and locate close to 0.05 for a pitch angle of $20°$. The simplest way to find properly the aerodynamic states initial values is to implement Leishman-Beddoes model for a short time as $t_f = 0.2\ \mathrm{s}$, while the structural states are at their initial values. In the full aeroelastic simulation, initial conditions

can be obtained from the aerodynamic states after reaching their converged values at the end of this pre-simulation.

The pre-simulation results are shown in Figure 6 including solid lines for the smart wing and dashed black lines for the regular wing. It indicates all of the aerodynamic states can converge to constant values after 0.2 s. These values can be considered as initial conditions, along with the initial values of the pitch and pitch rate. From Figure 6, it is clear that both smart and regular wings have the same aerodynamic state response during pre-simulation time interval.

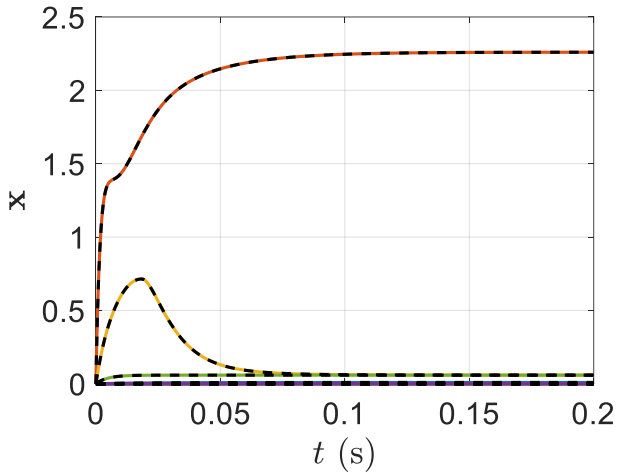

Fig. 6 Aerodynamic state response versus time during pre-simulation, solid lines: smart wing, dashed lines: regular wing

The full aeroelastic simulation is started after resetting time to zero. The time response of the resulting pitch angle is shown in Figure 7 which indicates the stall flutter or LCO. It is clear that using smart material can decrease the maximum pitch angle from 23.5˚ in the regular wing to 20.3˚ in the smart wing which shows the effect of using smart material in decreasing the maximum pitch angle. The response of the regular wing settles onto a limit cycle frequency 5.6 Hz however, the smart wing limit cycle frequency is 5.47 Hz. Reduced frequency of the regular wing is $k = 0.11$ however, the smart wing reduced frequency is $k = 0.098$. Amplitude of the

regular wing is 10.86˚ and its mean is 12.63˚ but the smart wing amplitude is 1.38˚ and its mean is 18.92˚.

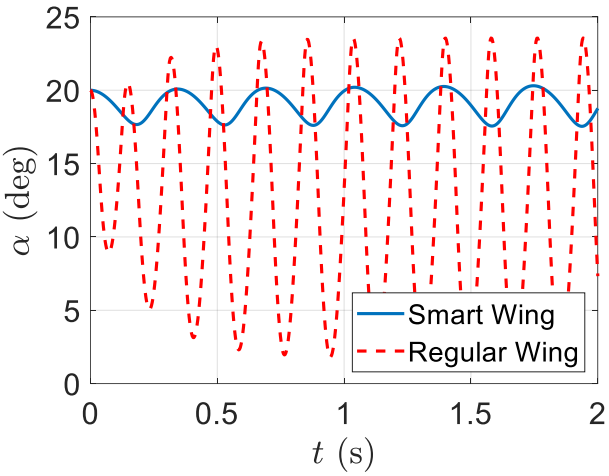

Fig. 7 Pitch angle time response

The load response versus pitch angle during the LCO has been depicted in Figure 8 which shows higher load response in the regular wing rather than the smart wing. In fact, using smart material can reduce the induced lift due to the leading edge vortex and increase the trailing edge vortex effect, as well. The experimental result is from McAlister et al. as a classic reference providing detailed aerodynamic loads on many different wing sections under dynamics stall at different kinematic and flow conditions [75]. The experimental result is for a wing with a NACA 0012 section under forced pitching oscillations with an amplitude of 10˚ around a mean pitch angle of 12˚ with reduced frequency $k = 0.098$ at a Mach number of 0.3. The experimental measured normal force coefficient is around the quarter chord against instantaneous pitch angle and it is also a cycle average. The arrows indicate the direction of the experimental normal force coefficient variation as the pitch angle increases from 4˚ to 22˚ and then back down to 4˚. In the regular wing, the pitch angle increases from 2˚ to 22˚ and then back down to 2˚. However, in the smart wing, the pitch angle increases from 17.4˚ to 20.6˚ then back down to 17.4˚. It means that the smart wing is able to control effectively the pitching

oscillation of the wing during the stall flutter or LCO. The angle of static stall is 12˚ however, it is increased during the oscillation to 16.4˚. The smart wing results shows an increase in the dynamic stall angle due to increasing in the wing oscillation to 20.3˚. The characteristics of the LCO of the regular wing are very similar to the those of the forced oscillation of experimental result in [75], therefore the load response versus the angle of attack plots of the regular wing and experiment resemble closely. The only difference is the fact that the effect of the LEV is stronger in the regular wing because of existing the slightly higher frequency and amplitude. However, due to the lower frequency and amplitude in the smart wing rather than the experiment, the effect of the LEV is weaker in the smart wing.

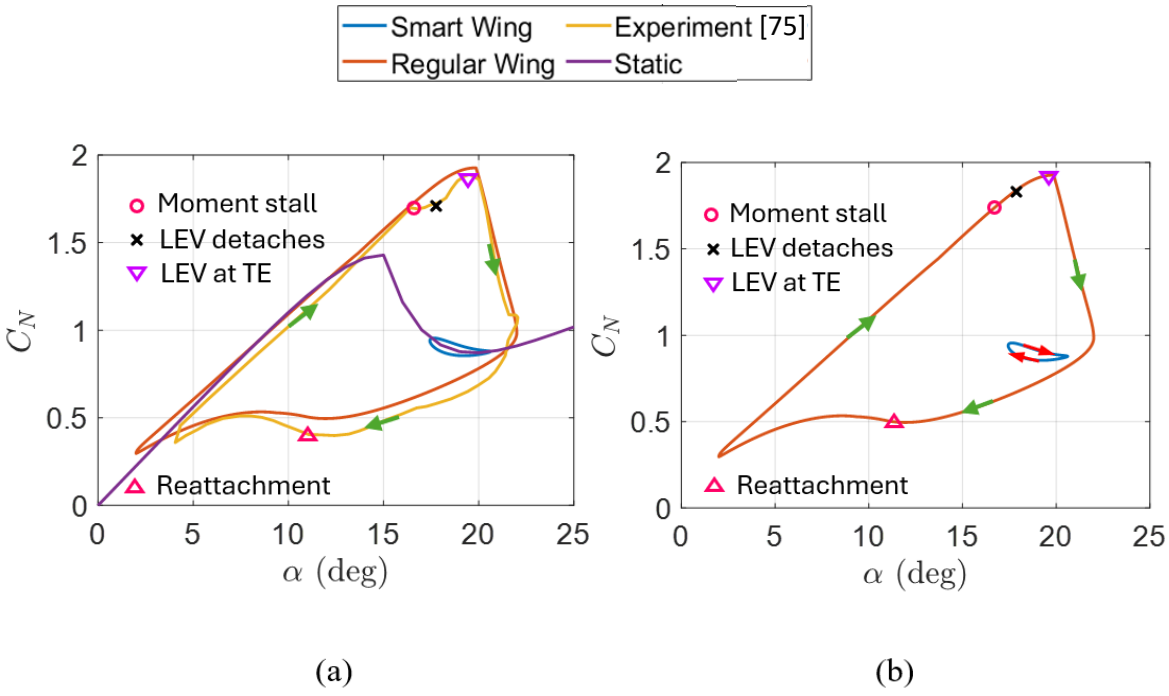

Fig. 8 Load response versus pitch angle: **(a)** smart and regular wings, experiment, and static, **(b)** smart and regular wings

Dynamic lift initially varies linearly with pitch angle with slope equals to that of the static lift curve, as shown in Figure 8. In the experiment, up to $\alpha = 16.4°$, the dynamic lift remains linear which is more than 4° higher than the static stall angle. However, in the regular wing, up to $\alpha = 17°$, the dynamic lift remains linear which is more than 5° higher than the static stall angle.

In the smart wing, the dynamic lift becomes completely nonlinear. Moreover, in both the experiment and regular wing, there are a large amount of increase in the static maximum lift however, in the smart wing, that value decreases considerably. In the experiment, moment stall occurs at $\alpha = 16.4°$ which represents the start of dynamic stall leading to flattening out the lift variation with pitch angle. However, in the regular wing, moment stall appears at $\alpha = 18°$ and in the smart wing, the wing remains always in stall. Furthermore, in the experiment at $\alpha = 17.9°$, the LEV detaches from the leading edge and starts to move down the chord leading to increasing the lift, but in the smart wing, the LEV is always detached from the leading edge and in the regular wing, it happens at $\alpha = 18.5°$. The LEV effect on the aerodynamic loads decreases rapidly such as dropping the lift while there is a fully separated flow on the upper surface of the regular wing. However, those effects on the smart wing are much less in terms of lift dropping and upper surface fully separated flow, as shown in Figure 8. Finally, the regular wing reaches the maximum pitch angle of 22˚ then its pitch angle starts to decrease until reaching the minimum pitch angle of 2˚. However, the smart wing reaches the maximum pitch angle of 20.6˚ then its pitch angle starts to decrease until reaching the minimum pitch angle of 17.4˚. In the regular wing, the flow re-attach again fully by the time $\alpha = 10.7°$ however, in the smart wing, the flow fully attachment never occurs. Table 5 shows the comparison between the smart and regular wings and experimental results for different parameters.

Table 5 Comparison between smart and regular wings and experiment

	Smart Wing	Regular Wing	Experiment
Minimum pitch angle	17.4˚	2˚	4˚
Maximum pitch angle	20.6˚	22˚	22˚
Dynamic stall angle	-	18˚	16.4˚
LEV detaches	-	18.5˚	17.9˚

LEV at TE	-	10.7˚	10.7˚

The stall delay effect occurs due to inviscid and viscous mechanisms. The inviscid flow has a reduction in the adverse pressure gradient over most of the surface of the wing during pitch up in compared to one acting on the static wing surface at the same instantaneous angle of attack. In other words, during moving upward, the boundary layer is further from stall hence stays attached up to higher angles of attack than in the static case [76]. The viscous mechanism is referred to as the leading edge jet or moving wall effect [77]. The boundary layer velocity at the wall of a static wing is zero because of static wall. However, on the pitching up wing, the leading edge is moving up parallel to the boundary layer flow direction. Having nonzero boundary layer speed at the wall can add a considerable momentum input to the boundary layer leading to stall delay. The leading edge jet only has a significant effect very close to the leading edge and in downstream of the leading edge, the leading edge jet add very little momentum to the boundary layer. At the moving down, there is inverted moving wall effect therefore, the flow is forced to separate at the leading edge leading to reattachment delay.

Probably the LEV is the most major difference between static and dynamic stall. There are three main mechanisms for the LEV formation and shedding [78, 79]. The first mechanism which occurs on wings with sharp leading edges is bubble bursting in the leading edge laminar separation. Since the boundary layer near the leading edge is laminar, laminar separation happens first. Then due to becoming turbulent of the separated shear layer and re-attaching again, a separation bubble forms. Increasing the pitch angle leads to bursting the bubble abruptly and creating the LEV that then propagates downstream. The trailing edge separation does not interfere with the LEV formation process, as there is a certain amount of trailing edge separation. The second mechanism is mixed leading edge/trailing edge stall with flow separation occurs first at the trailing edge and starts to move upstream. By increasing the pitch angle, there is an abrupt separation of the turbulent boundary layer on the entire front section

of the wing leading to spreading flow reversal to nearly all the wing upper surface and forming the LEV near the leading edge. The third mechanism is shock-induced separation due to strong shocks occurring at higher Mach numbers near the leading edge. Strong shocks impose very high adverse pressure gradient on the boundary layer leading to forcing separation. At the foot of the last strong shock wave, the LEV creates in oblong shape and initially enveloped in supersonic external flow. Depending to the roughness of the leading edge and the Reynolds number, the shock-induced separation mechanism can interact with the laminar separation bubble bursting mechanism.

The pitching moment versus pitch angle during the LCO is indicated in Figure 9. It is clear that using smart material cannot increase the pitching moment in high pitch angle in comparison with the regular wing one. In other words, the LEV can induce more pitching moment in the regular wing in comparison with the one in the smart wing. Furthermore, the trailing edge vortex effect in inducing pitching moment in the smart wing is lower than the one in the regular wing.

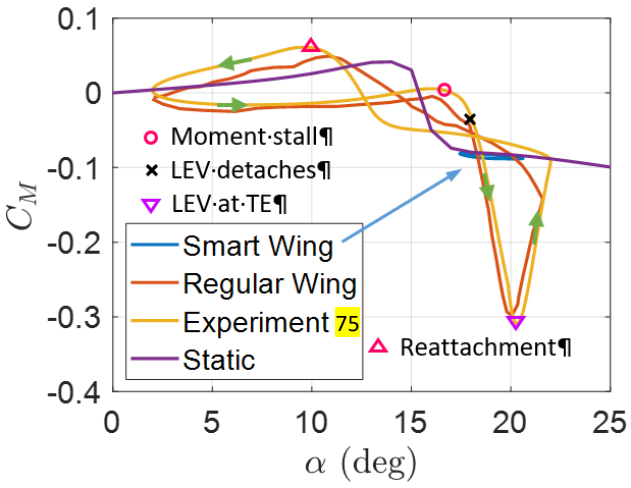

Fig. 9 Pitching moment versus pitch angle

The pitching moment around the pitching axis, x_f, versus pitch angle during the LCO is indicated in Figure 10 which shows implementing smart material can help increase the pitching

moment in high pitch angle due to improving of the leading edge vortex effect and in addition it can reduce the effect of trailing edge, as well. There are some differences between Figure 10 and Figure 9. Both figures for the regular wing include three loops with different relative sizes. However, for the smart wing in Figure 9 there is only one loop but in Figure 10 there are two loops. Considering the aerodynamic work done during a complete cycle as

$$W = \oint c_{m_{x_f}} \, dx \tag{23}$$

there are following distinguish two cases

Case 1- The $c_{m_{x_f}}$ versus α loop has a counter-clockwise direction which includes a negative moment when α increases and vice-versa. There is a negative total work done over the cycle by the structure on the fluid domain. Therefore, the structure loses energy and its motion is damped.

Case 2- The $c_{m_{x_f}}$ versus α loop has a clockwise direction which includes a positive moment when α increases and vice-versa. There is a positive total work done over the cycle by the fluid on the structure domain. Therefore, the structure obtains energy and its motion amplitude is increased.

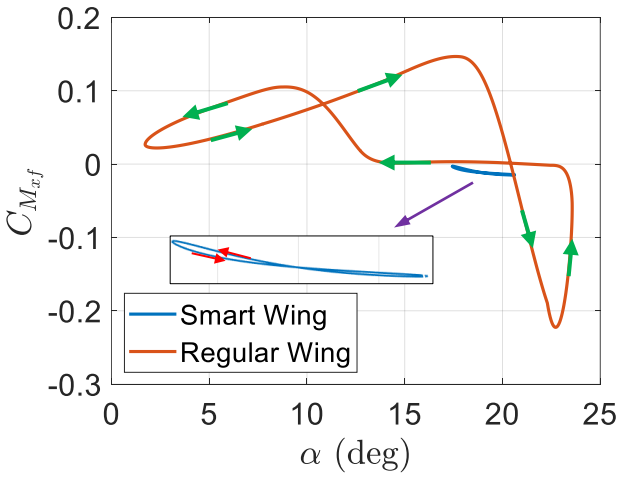

Fig. 10 Pitching moment around the pitching axis versus pitch angle

The two outer loops in Figure 10 have counter-clockwise directions however, the inner loop posses a clockwise direction. The total work done over the cycle is positive because the inner loop is bigger than the two outer combined. Hence, the fluid is performing work on the structure leading to sustain the stall flutter or limit cycle.

In contrast, in Figure 9, the total work done by the pitching moment around the aerodynamic center is negative since the inner loop is smaller than the two outer ones. In fact, if the pitch axis is moved to the quarter-chord, the stall flutter or LCO would be removed the motion would be damped.

The pitching velocity versus pitch angle has been depicted in Figure 11 where the system trajectory starts from the point (20,0) according to the initial condition of the system. The smart wing trajectory starts from the initial pitch angle and pitching velocity in the inner part and the trajectory is turning to the outer part where the stall flutter or LCO occurs as shown in Figure 11.

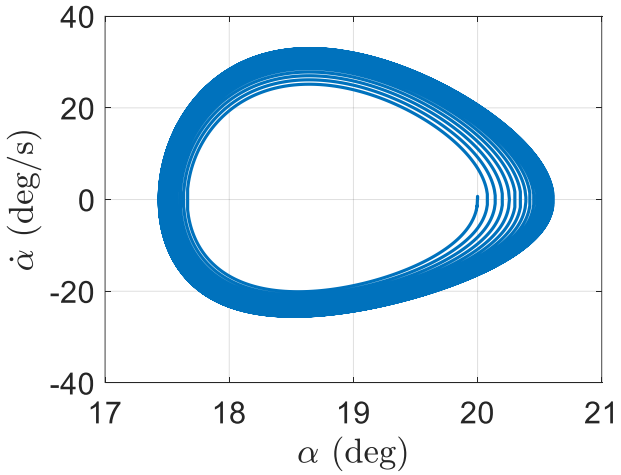

Fig. 11 Phase plane for pitching velocity versus pitch angle

The start point of the phase plane for the electric current and charge starts from the zero initial conditions for the electric charge and current, as shown in Figure 12. The trajectory twists in clockwise until reaching its limit value in the stall flutter or LCO.

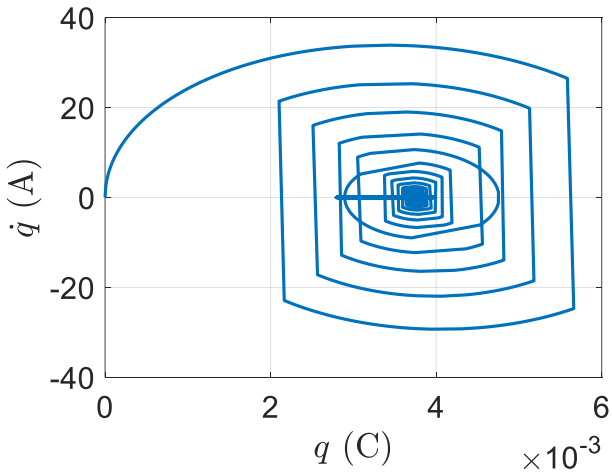

Fig. 12 Phase plane for pitch electric current versus pitch electric charge

Example 4 Smart wing stall flutter elimination

As fourth example, we conduct an aeroelastic analysis on the same smart wing for example 3 except the pitching coupling coefficient of piezoelectric material which is $e_\alpha = 1.463 \times 10^{-1}$ C/m to represent the effect of the piezoelectric patch on stall flutter elimination. Using the Runge-Kutta-Fehlberg approach and event detection, one can solve the implicit scheme by considering the same parameters of Table 4. As mentioned in example 3, we need note that the aerodynamic states initial values are unknowns, and they cannot be considered all as zero. For instance, x_{10} and x_{12} represent the separation point positions and locate close to 0.05 for a pitch angle of 20°. The simplest way to find properly the aerodynamic states initial values is to implement Leishman-Beddoes model for a short time as $t_f = 0.2$ s, while the structural states are at their initial values. In the full aeroelastic simulation, initial conditions can be obtained from the aerodynamic states after reaching their converged values at the end of this pre-simulation.

The pre-simulation results are shown in Figure 13 including solid lines for the smart wing and dashed black lines for the regular wing. It indicates all of the aerodynamic states can converge to constant values after 0.2 s. These values can be considered as initial conditions, along with

the initial values of the pitch and pitch rate. From Figure 13, it is clear that both smart and regular wings have the same aerodynamic state response during pre-simulation time interval.

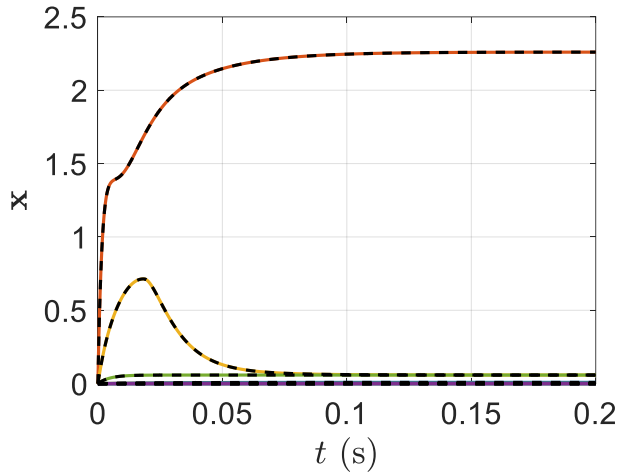

Fig. 13 Aerodynamic state response versus time during pre-simulation, solid lines: smart wing, dashed lines: regular wing

The full aeroelastic simulation is started after resetting time to zero. The time response of the resulting pitch angle is shown in Figure 14 which indicates the stall flutter or LCO. It is clear that using smart material can decrease the maximum pitch angle from 23.5˚ in the regular wing to 19.9˚ in the smart wing which shows the effect of using smart material in decreasing the maximum pitch angle. The response of the regular wing settles onto a limit cycle frequency 5.6 Hz however, the smart wing has no limit cycle.

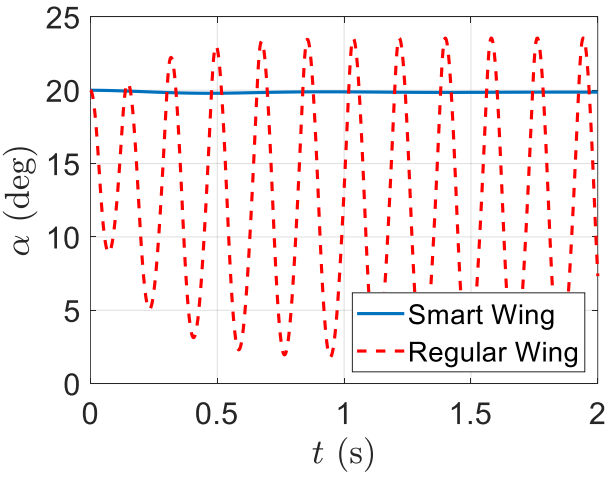

Fig. 14 Pitch angle time response

The load response versus pitch angle during the LCO has been depicted in Figure 15 which shows higher load response in the regular wing rather than the smart wing. In fact, using smart material due to no oscillation load response value becomes one point, as shown in Figure 15. In the smart wing, the pitch angle remains around 19.9˚ since there is no oscillatory motion. It means that the smart wing is able to eliminate effectively the pitching oscillation of the wing during the stall flutter or LCO.

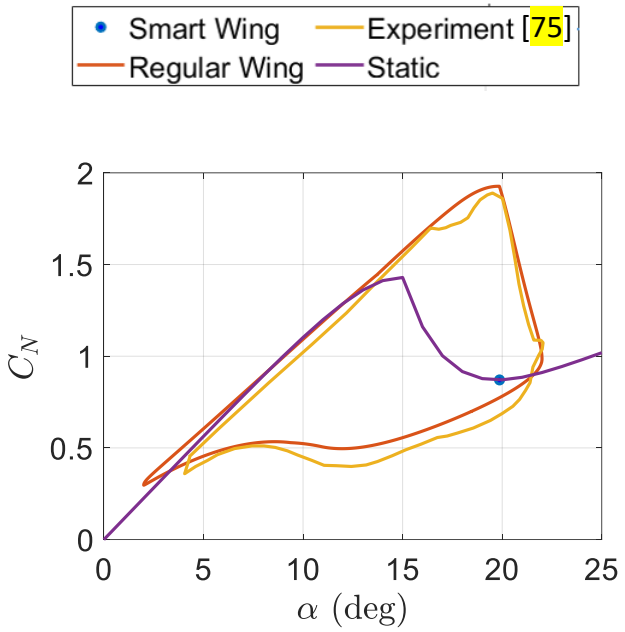

Fig. 15 Load response versus pitch angle: smart and regular wings, experiment, and static

In the smart wing, due to having a constant pitch angle, there is no dynamic lift. Moreover, in both the experiment and regular wing, there are a large amount of increase in the static maximum lift however, in the smart wing, that value decreases considerably. In the experiment, moment stall occurs at $\alpha = 16.4°$ which represents the start of dynamic stall leading to flattening out the lift variation with pitch angle. However, in the regular wing, moment stall appears at $\alpha = 18°$ and in the smart wing, the wing remains always in stall. Furthermore, in the smart wing, the LEV is always detached from the leading edge.

The pitching moment versus pitch angle during the LCO is indicated in Figure 16. It is clear that using smart material cannot increase the pitching moment in high pitch angle in comparison with the regular wing one. In other words, the LEV can induce more pitching moment in the regular wing in comparison with the one in the smart wing. Furthermore, the trailing edge vortex effect in inducing pitching moment in the smart wing is lower than the one in the regular wing.

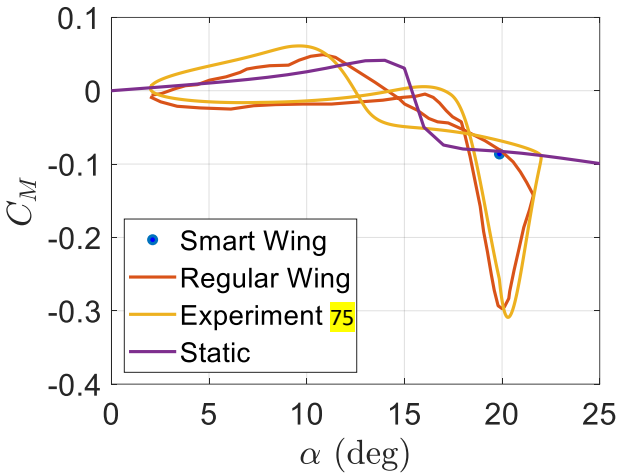

Fig. 16 Pitching moment versus pitch angle

The pitching moment around the pitching axis, x_f, versus pitch angle during the LCO is indicated in Figure 17 which shows implementing smart material to eliminate stall flutter cannot help increase the pitching moment in high pitch angle due to not improving of the leading edge vortex effect and in addition it cannot reduce the effect of trailing edge, as well. There are some differences between Figure 17 and Figure 16. Both figures for the regular wing include three loops with different relative sizes. However, for the smart wing in both Figures 16 and 17, there is no loop since there is no oscillation.

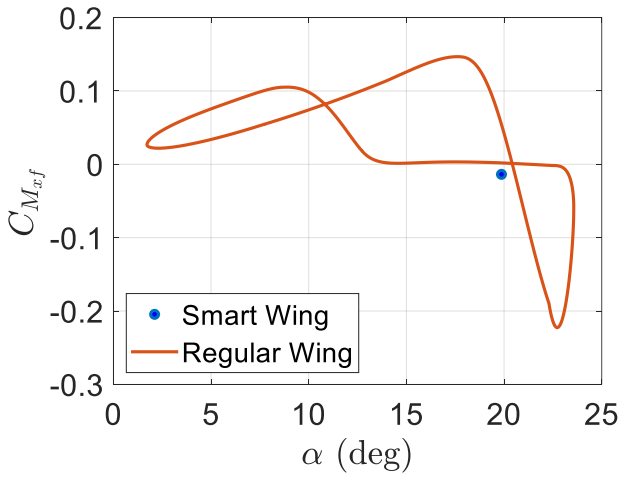

Fig. 17 Pitching moment around the pitching axis versus pitch angle

The pitching velocity versus pitch angle has been depicted in Figure 18 where the system trajectory starts from the point (20,0) according to the initial condition of the system. The smart wing trajectory starts from the initial pitch angle and pitching velocity in the inner part and the trajectory is turning to the outer part where the stall flutter or LCO occurs as shown in Figure 18.

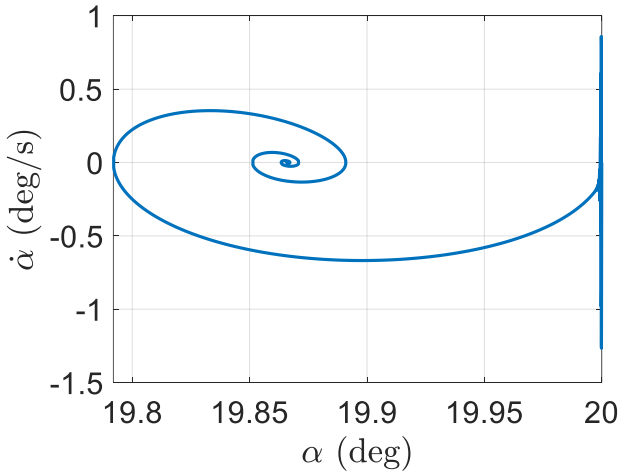

Fig. 18 Phase plane for pitching velocity versus pitch angle

The start point of the phase plane for the electric current and charge starts from the zero initial conditions for the electric charge and current, as shown in Figure 19. The trajectory twists in clockwise until reaching its limit value in the stall flutter or LCO.

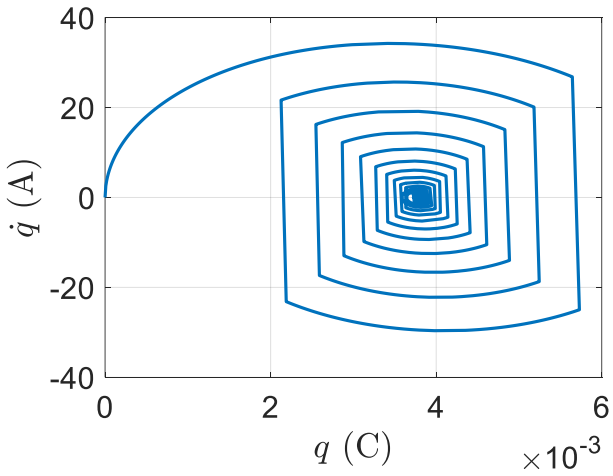

Fig. 19 Phase plane for pitch electric current versus pitch electric charge

5. Parametric Study for Stall Flutter Alleviation and Elimination

In this section, effects of different parameters of the smart wing on stall flutter alleviation are investigated. According to the smart wing configuration shown in Figure 1, we consider the parameters as x_p, piezoelectric axis, β_α, pitch electromechanical coupling, L_α, pitch inductance of piezoelectric material, R_α, pitch resistance of piezoelectric material, and C_{p_α}, pitch capacitance of piezoelectric material.

5.1 Effect of x_p on stall flutter alleviation and elimination

As the first parameter, we consider x_p with different values as $0.095c, 0.096c, 0.097c, 0.098c, 0.099c$, and $0.1c$, where c represents the chord length of the wing. Having different locations for the shunt piezoelectric patch cannot create any difference on the smart wing pre-simulation results obtaining the aerodynamic state initial values discussed in Section 4, as indicated in Figure 20.

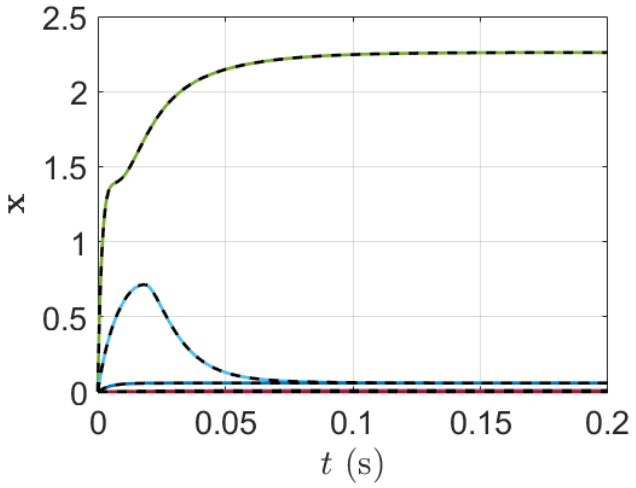

Fig. 20 Aerodynamic state response versus time during pre-simulation for different x_p location, solid lines: smart wing, dashed lines: regular wing

It is clear that changing the location of the piezoelectric patch does not change the aerodynamic state response versus time during pre-simulation as all of the aerodynamic states converge to constant values after 0.2 s, as shown in Figure 20. In other words, both smart and regular wings have the same aerodynamic state response during pre-simulation time interval. Furthermore, pitch angle time response of the smart wing changes with respect to the locations of the piezoelectric patch which indicates pitch angle time response of the smart wing is dependent on the location of the piezoelectric patch, as shown in Figure 21. Having piezoelectric patch at location of $0.095c$ can eliminate the LCO effectively. However, by moving the location towards $0.1c$, the amplitude of LCO is increased gradually.

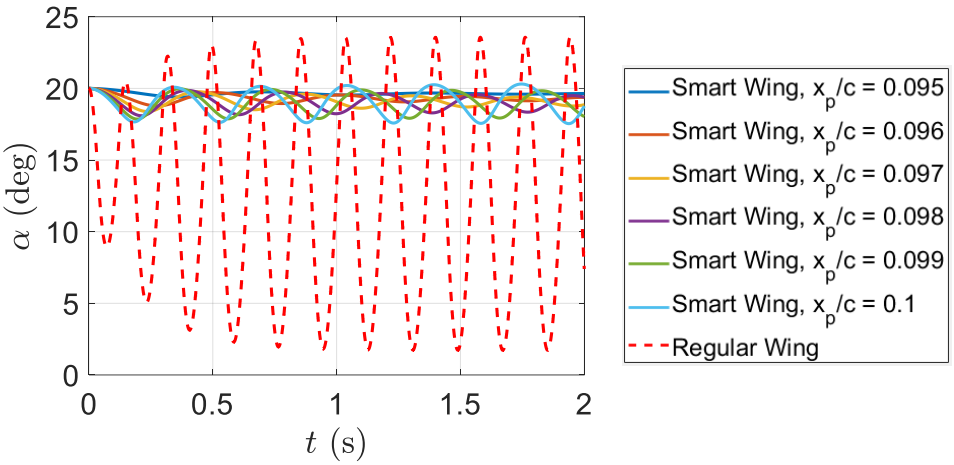

Fig. 21 Pitch angle time response for different x_p location

Also, the load response versus pitch angle during the LCO has been depicted in Figure 22 for different locations of the piezoelectric patch which indicates the load response of the smart wing is dependent on the location of the piezoelectric patch.

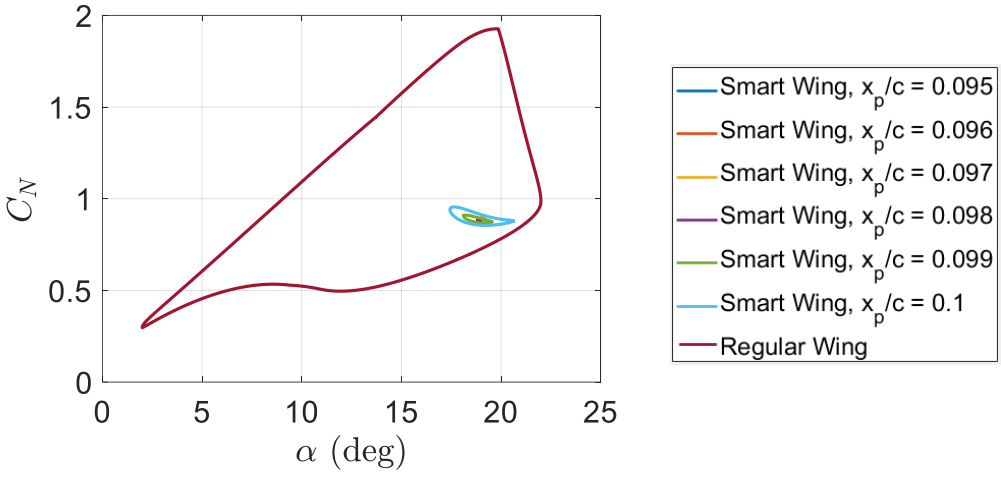

Fig. 22 Load response versus pitch angle for different x_p location

Moreover, the pitching moment versus pitch angle during the LCO has been shown in Figure 23 for different locations of the piezoelectric patch which indicates the pitching moment of the smart wing is dependent on the location of the piezoelectric patch.

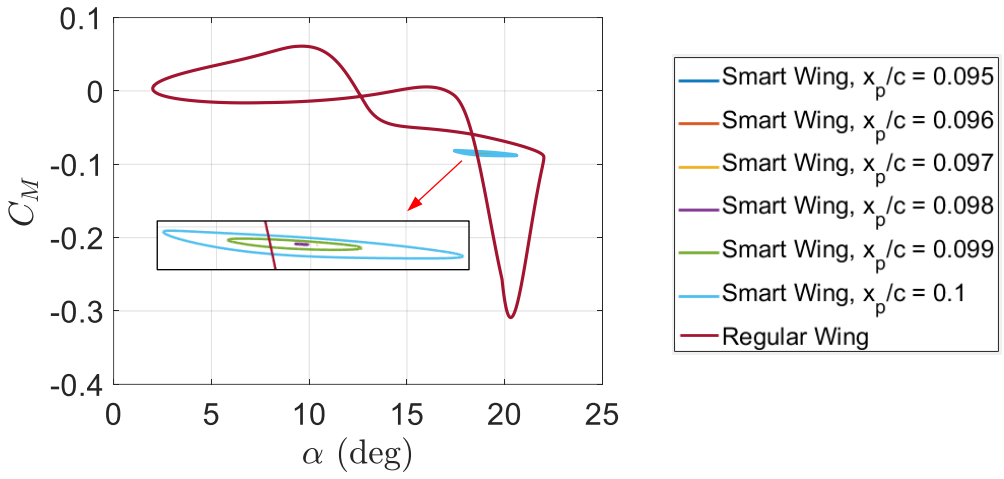

Fig. 23 Pitching moment versus pitch angle for different x_p location

The pitching moment around the pitching axis versus pitch angle during the LCO has also been depicted in Figure 24 for different locations of the piezoelectric patch which indicates the pitching moment around the pitching axis of the smart wing is dependent on the location of the piezoelectric patch.

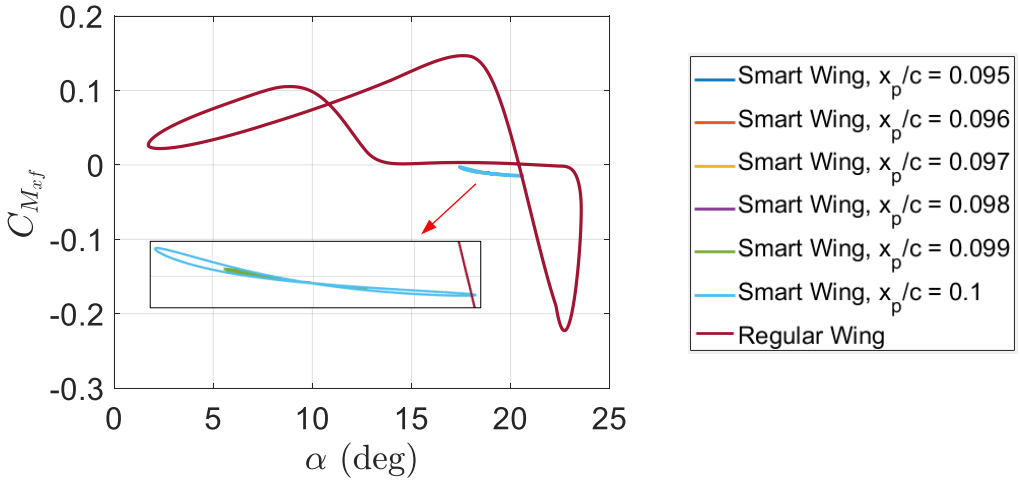

Fig. 24 Pitching moment around the pitching axis versus pitch angle for different x_p location

Furthermore, the phase plane for pitching velocity versus pitch angle during the LCO has been shown in Figure 25 for different locations of the piezoelectric patch which indicates the phase plane for pitching velocity of the smart wing is dependent on the location of the piezoelectric patch.

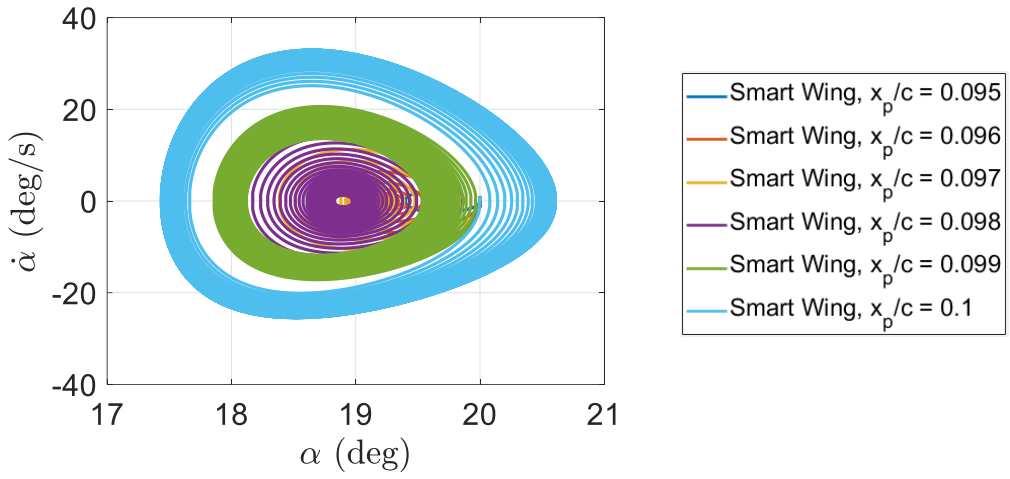

Fig. 25 Phase plane for pitching velocity versus pitch angle for different x_p location

Finally, the phase plane for pitch electric current versus pitch electric charge during the LCO has been depicted in Figure 26 for different locations of the piezoelectric patch which indicates the load response of the smart wing is almost independent on the location of the piezoelectric patch.

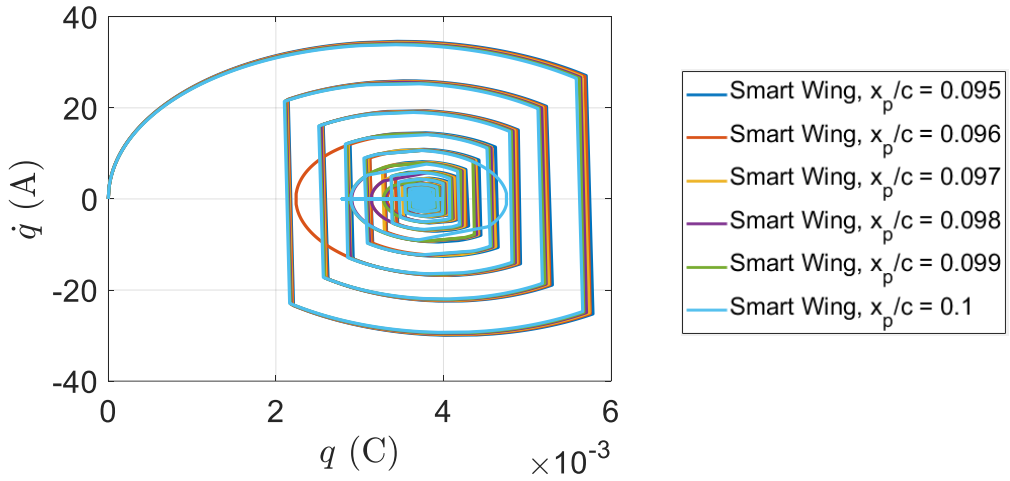

Fig. 26 Phase plane for pitch electric current versus pitch electric charge for different x_p location

5.2 Effect of L_α on stall flutter alleviation and elimination

As the second parameter, we consider L_α with different values as 0.01, 0.05, 0.1, 0.5, and 1 H. However, having different pitch inductance of piezoelectric material for the shunt piezoelectric patch cannot create any difference on the smart wing pre-simulation results obtaining the aerodynamic state initial values discussed in Section 4, as indicated in Figure 27.

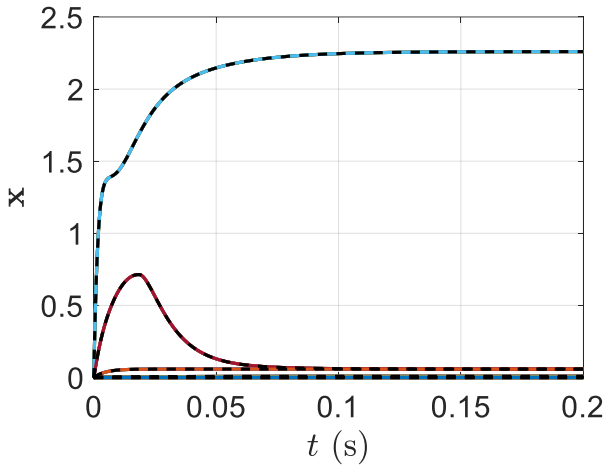

Fig. 27 Aerodynamic state response versus time during pre-simulation for different L_α, solid lines: smart wing, dashed lines: regular wing

It is clear that changing the pitch inductance of the piezoelectric patch does not change the aerodynamic state response versus time during pre-simulation as all of the aerodynamic states converge to constant values after 0.2 s, as shown in Figure 27. In other words, both smart and regular wings have the same aerodynamic state response during pre-simulation time interval. Furthermore, pitch angle time response of the smart wing does not change with respect to the pitch inductance of the piezoelectric patch which indicates pitch angle time response of the smart wing is independent on the pitch inductance of the piezoelectric patch, as shown in Figure 28.

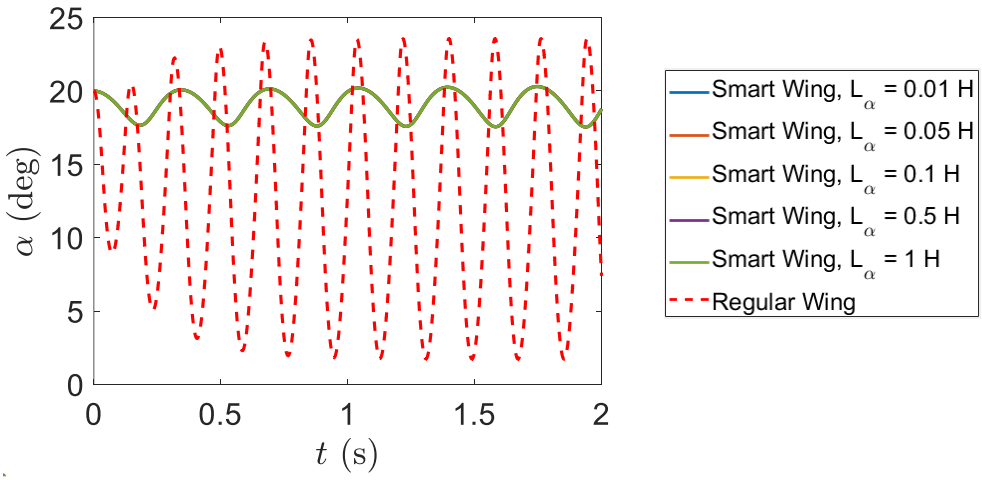

Fig. 28 Pitch angle time response for different L_α

Also, the load response versus pitch angle during the LCO has been depicted in Figure 29 for different pitch inductance of the piezoelectric patch which indicates the load response of the smart wing is independent on the pitch inductance of the piezoelectric patch.

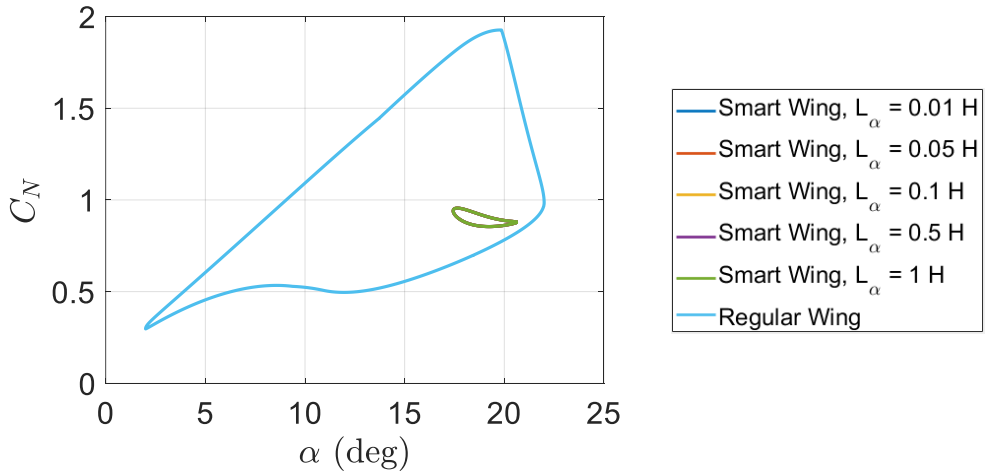

Fig. 29 Load response versus pitch angle for different L_α

Moreover, the pitching moment versus pitch angle during the LCO has been shown in Figure 30 for different pitch inductance of the piezoelectric patch which indicates the pitching moment of the smart wing is not dependent on the pitch inductance of the piezoelectric patch.

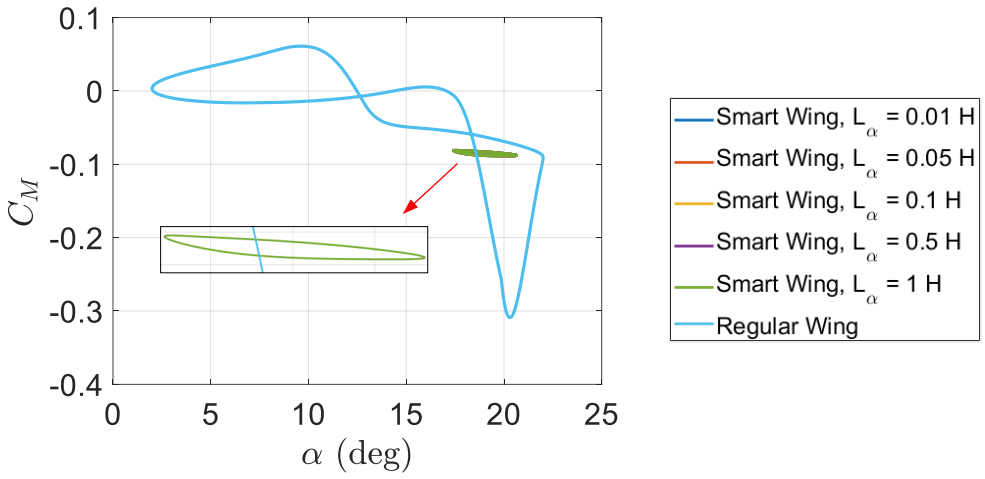

Fig. 30 Pitching moment versus pitch angle for different L_α

The pitching moment around the pitching axis versus pitch angle during the LCO has also been depicted in Figure 31 for different pitch inductance of the piezoelectric patch which indicates the pitching moment around the pitching axis of the smart wing is independent on the pitch inductance of the piezoelectric patch.

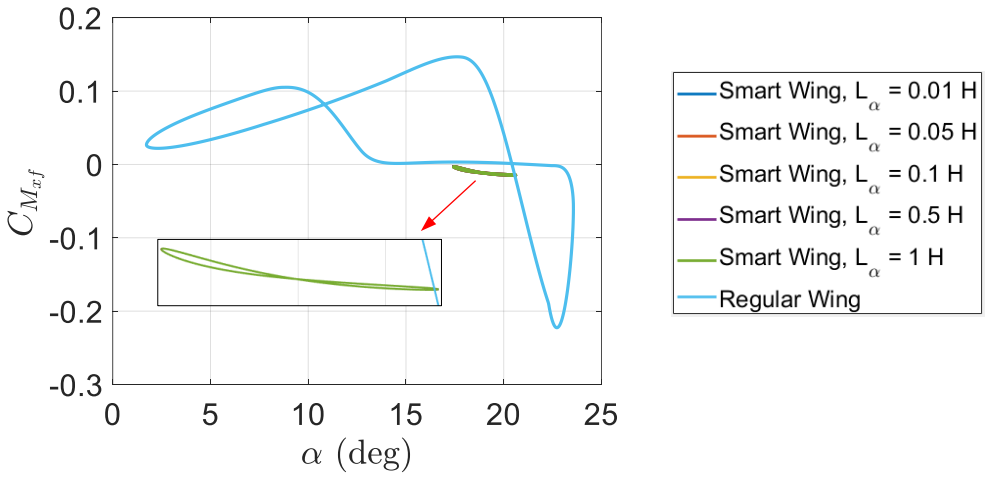

Fig. 31 Pitching moment around the pitching axis versus pitch angle for different L_α

Furthermore, the phase plane for pitching velocity versus pitch angle during the LCO has been shown in Figure 32 for different pitch inductance of the piezoelectric patch which indicates the phase plane for pitching velocity of the smart wing is not dependent on the pitch inductance of the piezoelectric patch.

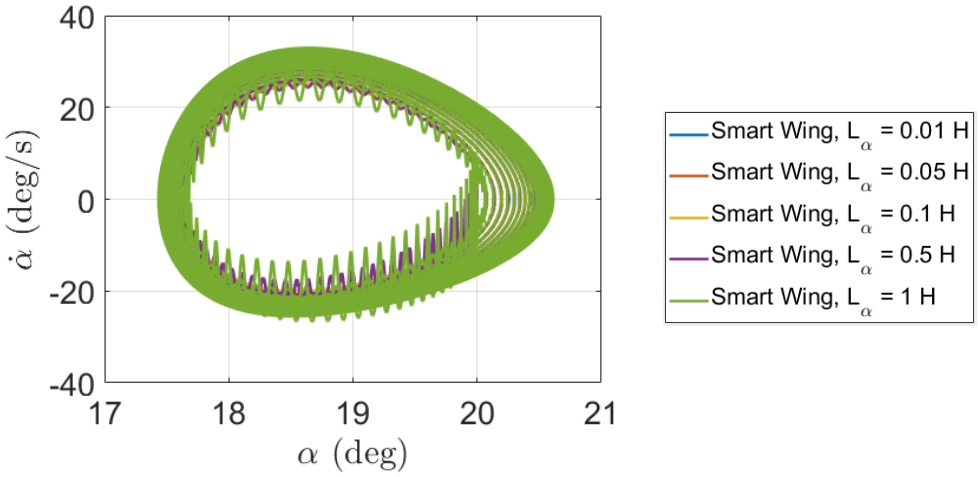

Fig. 32 Phase plane for pitching velocity versus pitch angle for different L_α

Finally, the phase plane for pitch electric current versus pitch electric charge during the LCO has been depicted in Figure 33 for different pitch inductance of the piezoelectric patch which indicates the load response of the smart wing is dependent on the pitch inductance of the piezoelectric patch.

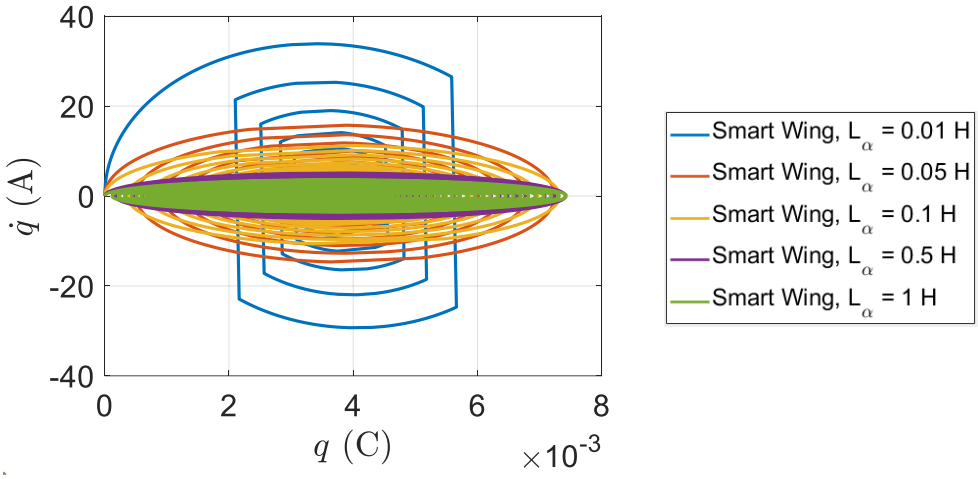

Fig. 33 Phase plane for pitch electric current versus pitch electric charge for different L_α

5.3 Effect of e_α on stall flutter alleviation and elimination

As the third parameter, we consider e_α with different values as 1.4455×10^{-1}, 1.446×10^{-1}, 1.4465×10^{-1}, and 1.447×10^{-1} C/m. However, having different pitch coupling coefficient of piezoelectric material for the shunt piezoelectric patch cannot create any difference on the

smart wing pre-simulation results obtaining the aerodynamic state initial values discussed in Section 4, as indicated in Figure 34.

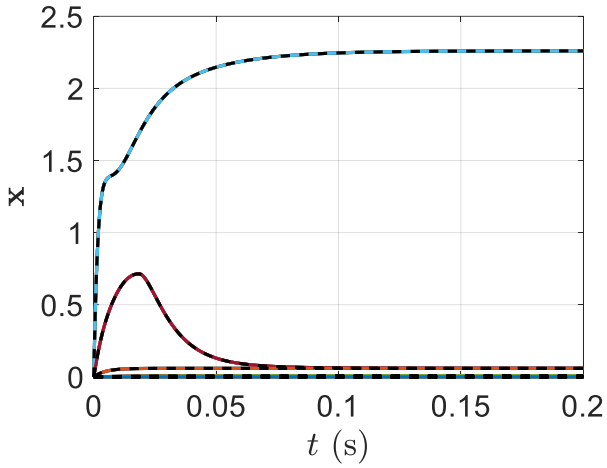

Fig. 34 Aerodynamic state response versus time during pre-simulation for different e_α

It is clear that changing the pitch coupling coefficient of the piezoelectric patch does not change the aerodynamic state response versus time during pre-simulation as all of the aerodynamic states converge to constant values after 0.2 s, as shown in Figure 34. In other words, both smart and regular wings have the same aerodynamic state response during pre-simulation time interval. Furthermore, pitch angle time response of the smart wing changes slightly with respect to the pitch coupling coefficient of the piezoelectric patch which indicates pitch angle time response of the smart wing is slightly dependent on the pitch coupling coefficient of the piezoelectric patch, as shown in Figure 35.

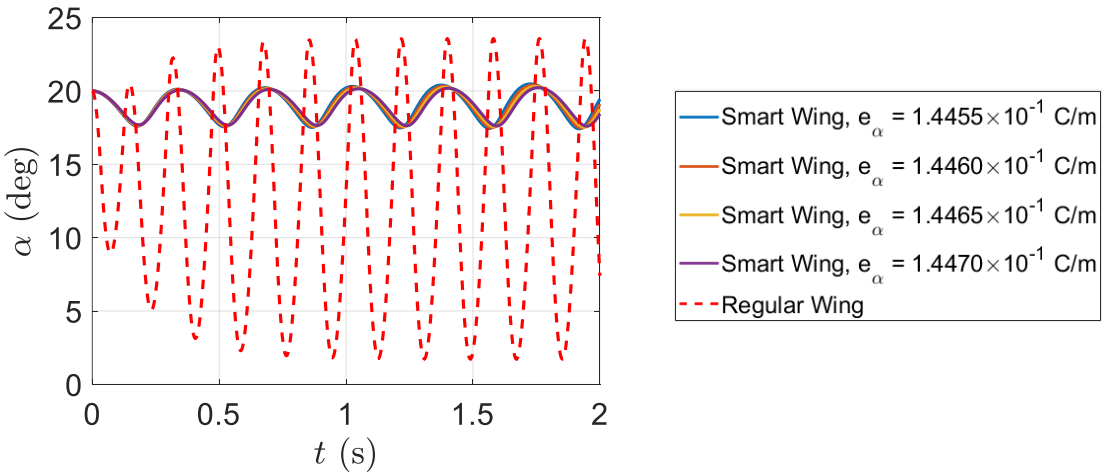

Fig. 35 Pitch angle time response for different e_α

Also, the load response versus pitch angle during the LCO has been depicted in Figure 36 for different pitch coupling coefficient of the piezoelectric patch which indicates the load response of the smart wing is slightly dependent on the pitch coupling coefficient of the piezoelectric patch.

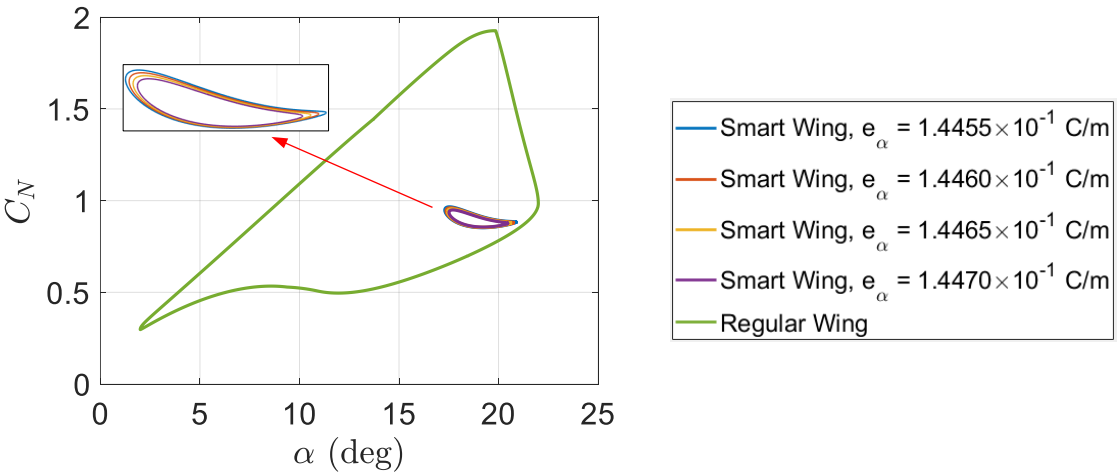

Fig. 36 Load response versus pitch angle for different e_α

Moreover, the pitching moment versus pitch angle during the LCO has been shown in Figure 37 for different pitch coupling coefficient of the piezoelectric patch which indicates the

pitching moment of the smart wing is slightly dependent on the pitch coupling coefficient of the piezoelectric patch.

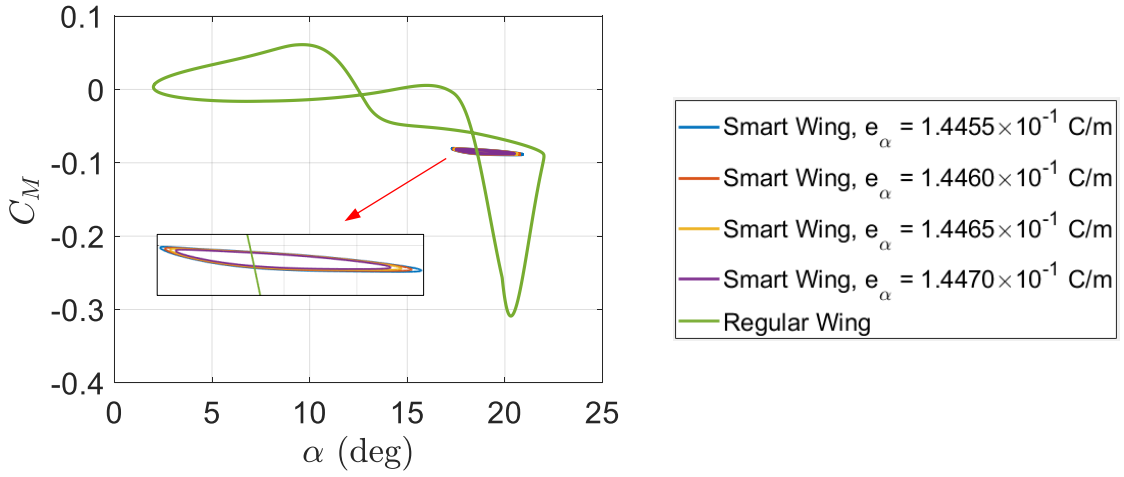

Fig. 37 Pitching moment versus pitch angle for different e_α

The pitching moment around the pitching axis versus pitch angle during the LCO has also been depicted in Figure 38 for different pitch coupling coefficient of the piezoelectric patch which indicates the pitching moment around the pitching axis of the smart wing is slightly dependent on the pitch coupling coefficient of the piezoelectric patch.

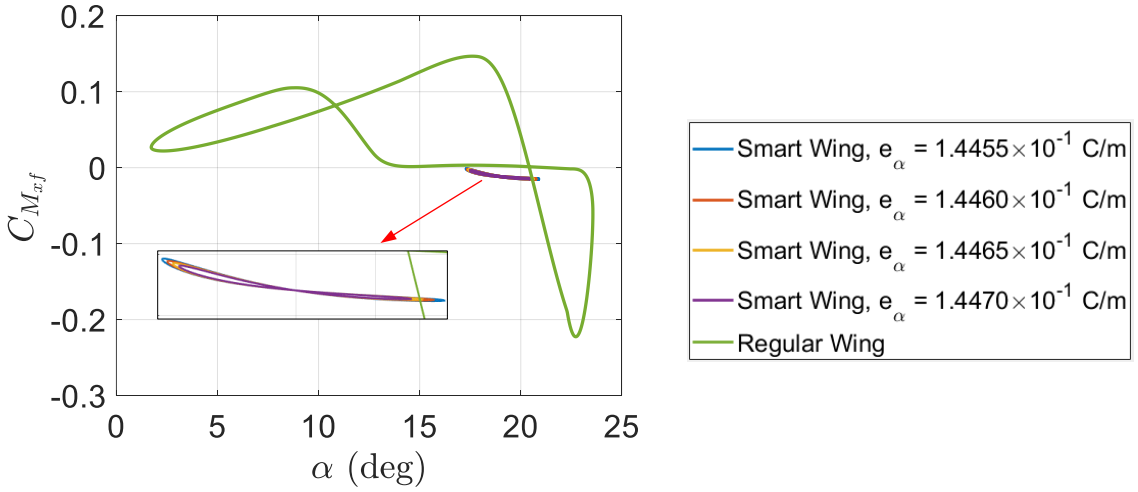

Fig. 38 Pitching moment around the pitching axis versus pitch angle for different e_α

Furthermore, the phase plane for pitching velocity versus pitch angle during the LCO has been shown in Figure 39 for different pitch coupling coefficient of the piezoelectric patch which indicates the phase plane for pitching velocity of the smart wing is dependent on the pitch coupling coefficient of the piezoelectric patch.

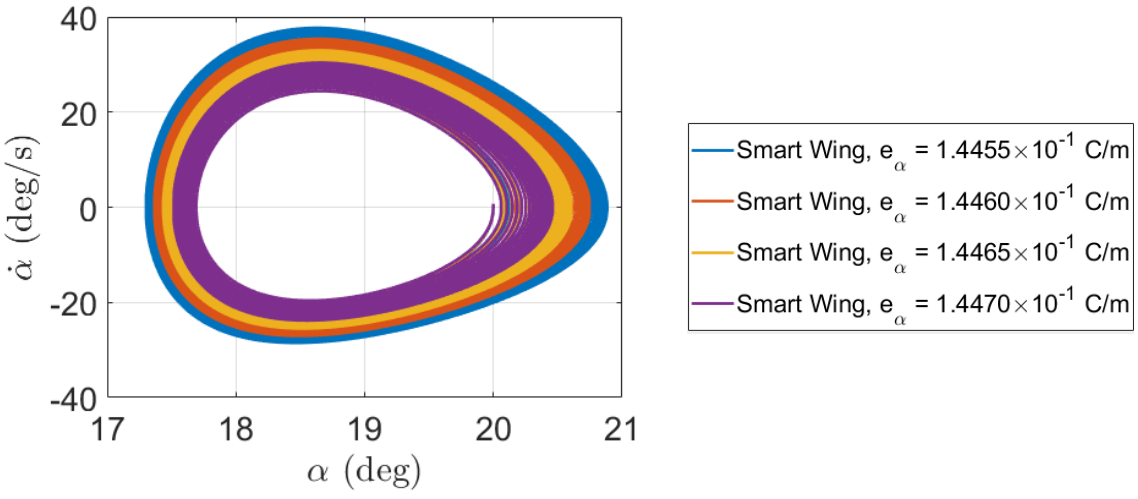

Fig. 39 Phase plane for pitching velocity versus pitch angle for different e_α

Finally, the phase plane for pitch electric current versus pitch electric charge during the LCO has been depicted in Figure 40 for different pitch coupling coefficient of the piezoelectric patch which indicates the load response of the smart wing is independent on the pitch coupling coefficient of the piezoelectric patch.

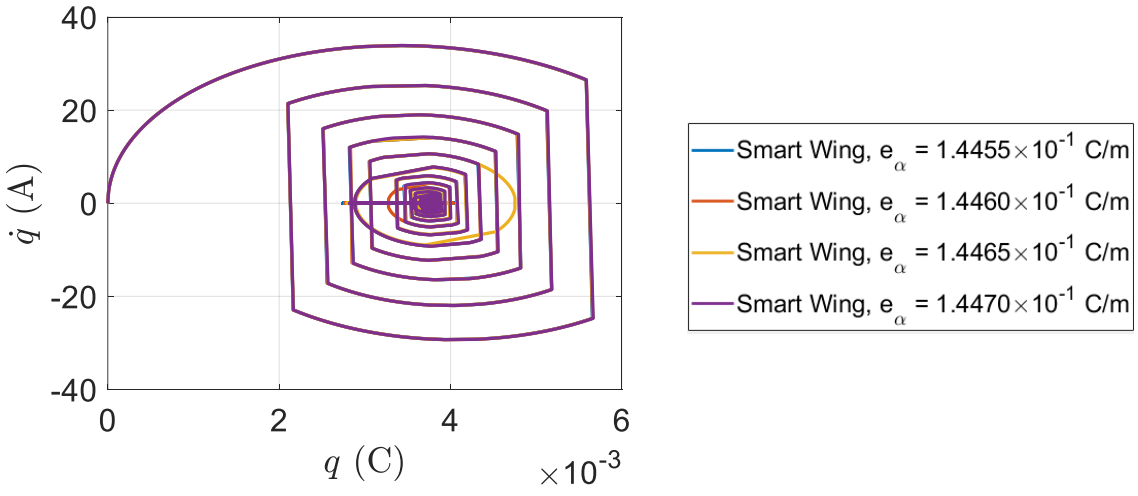

Fig. 40 Phase plane for pitch electric current versus pitch electric charge for different e_α

5.4 Effect of $C_{P\alpha}$ on stall flutter alleviation and elimination

As the fourth parameter, we consider $C_{p\alpha}$ with different values as 104×10^{-8}, 104.5×10^{-8}, 105×10^{-8}, 105.5×10^{-8}, and 106×10^{-8} F. However, having different pitch capacitance of piezoelectric material for the shunt piezoelectric patch cannot create any difference on the smart wing pre-simulation results obtaining the aerodynamic state initial values discussed in Section 4, as indicated in Figure 41.

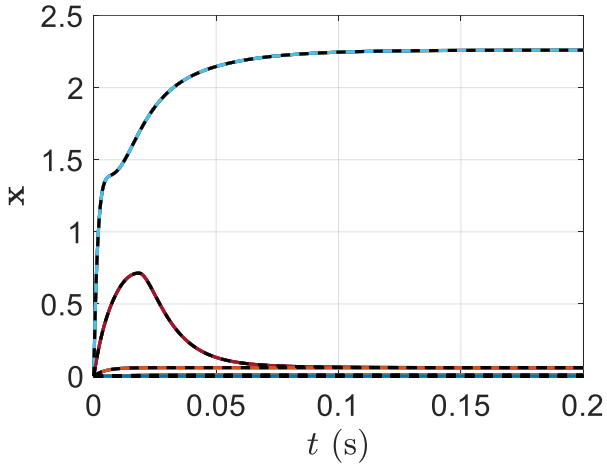

Fig. 41 Aerodynamic state response versus time during pre-simulation for different $C_{p\alpha}$

It is clear that changing the pitch coupling coefficient of the piezoelectric patch does not change the aerodynamic state response versus time during pre-simulation as all of the aerodynamic states converge to constant values after 0.2 s, as shown in Figure 41. In other words, both smart and regular wings have the same aerodynamic state response during pre-simulation time interval. Furthermore, pitch angle time response of the smart wing changes with respect to the pitch capacitance of the piezoelectric patch which indicates pitch angle time response of the smart wing is dependent on the pitch capacitance of the piezoelectric patch, as shown in Figure 42.

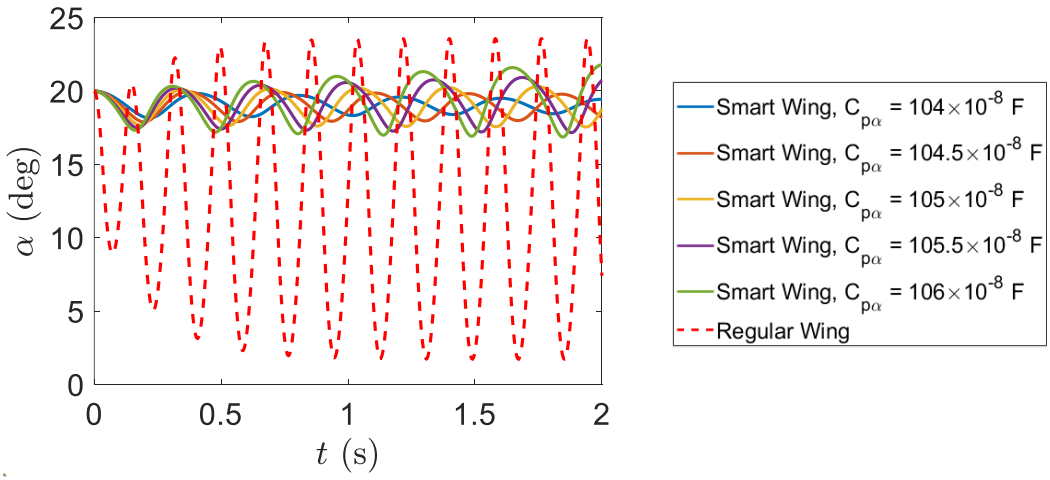

Fig. 42 Pitch angle time response for different $C_{p\alpha}$

Also, the load response versus pitch angle during the LCO has been depicted in Figure 43 for different pitch capacitance of the piezoelectric patch which indicates the load response of the smart wing is dependent on the pitch capacitance of the piezoelectric patch.

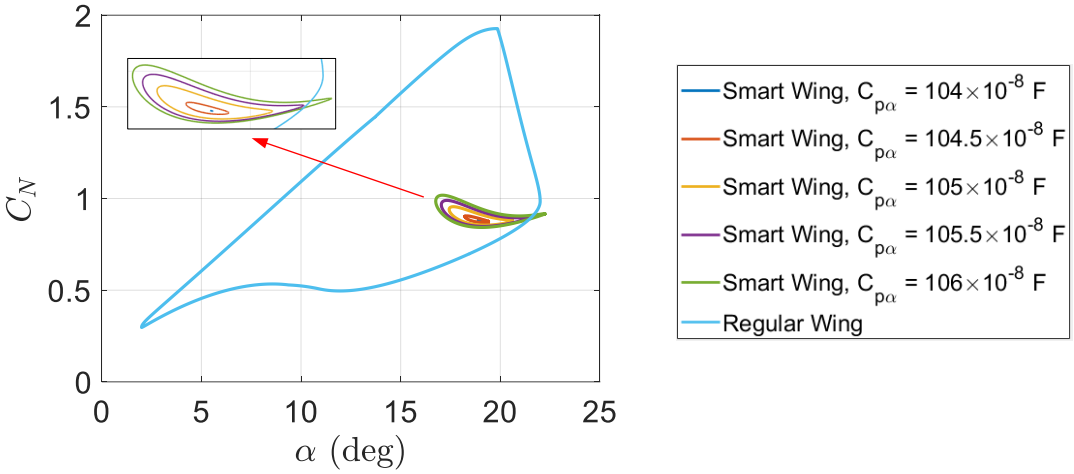

Fig. 43 Load response versus pitch angle for different $C_{p\alpha}$

Moreover, the pitching moment versus pitch angle during the LCO has been shown in Figure 44 for different pitch capacitance of the piezoelectric patch which indicates the pitching moment of the smart wing is dependent on the pitch capacitance of the piezoelectric patch.

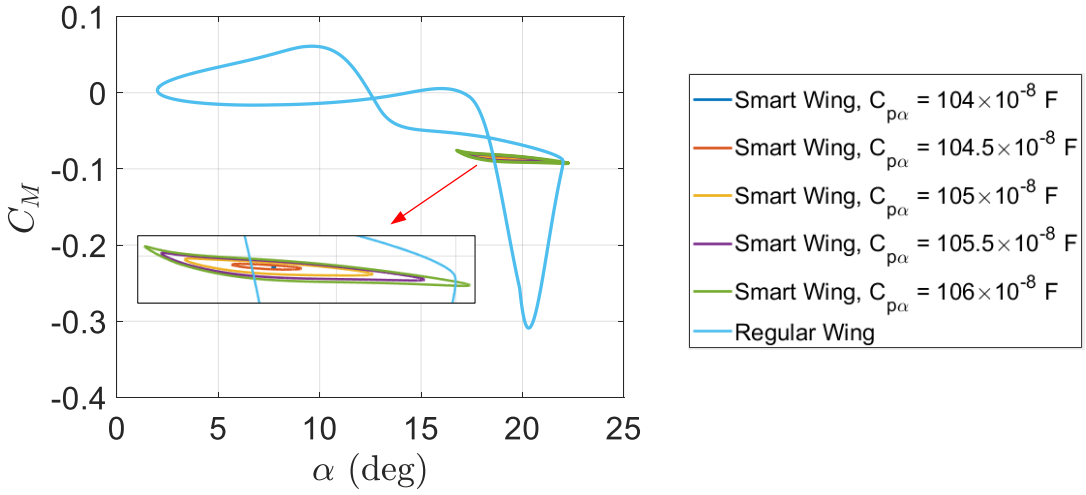

Fig. 44 Pitching moment versus pitch angle for different $C_{p\alpha}$

The pitching moment around the pitching axis versus pitch angle during the LCO has also been depicted in Figure 45 for different pitch capacitance of the piezoelectric patch which indicates the pitching moment around the pitching axis of the smart wing is dependent on the pitch capacitance of the piezoelectric patch.

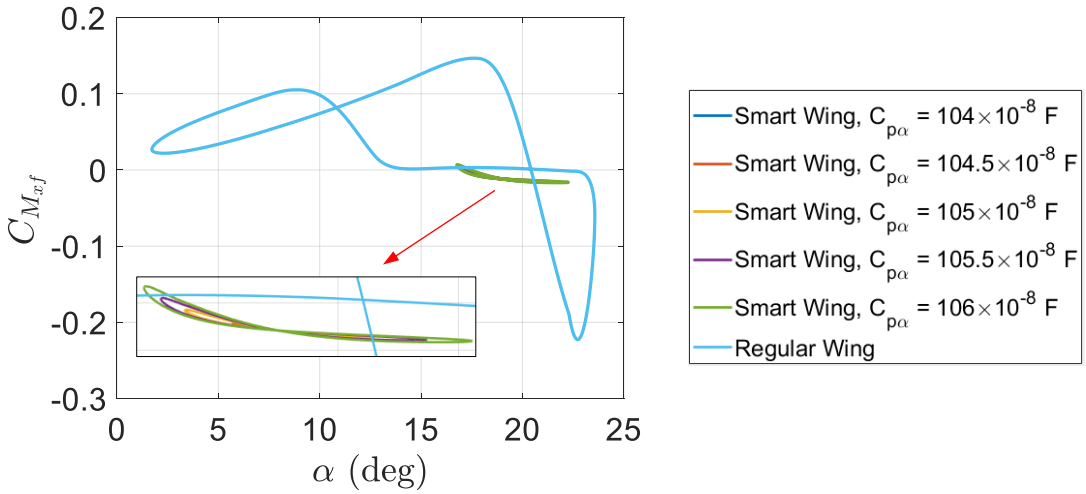

Fig. 45 Pitching moment around the pitching axis versus pitch angle for different $C_{p\alpha}$

Furthermore, the phase plane for pitching velocity versus pitch angle during the LCO has been shown in Figure 46 for different pitch capacitance of the piezoelectric patch which indicates

the phase plane for pitching velocity of the smart wing is dependent on the pitch capacitance of the piezoelectric patch.

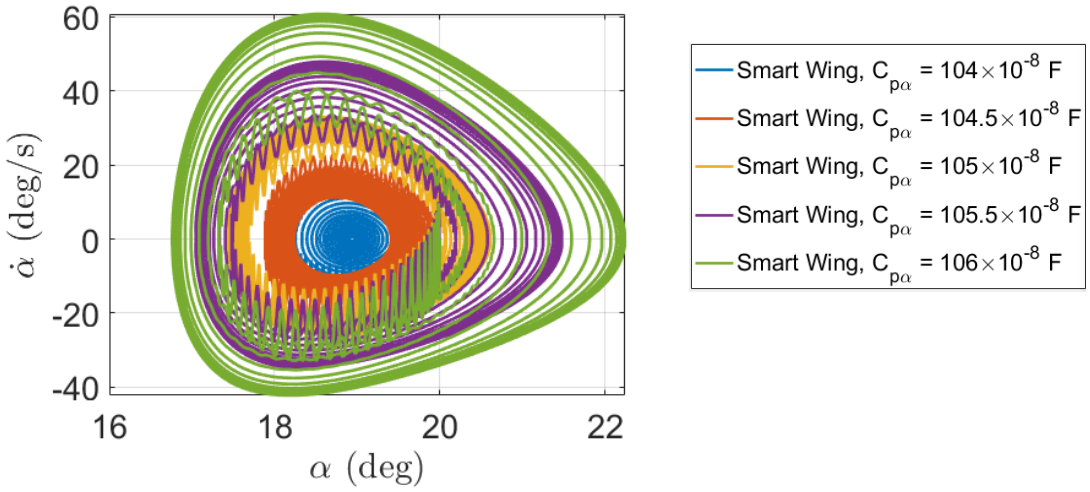

Fig. 46 Phase plane for pitching velocity versus pitch angle for different $C_{p\alpha}$

Finally, the phase plane for pitch electric current versus pitch electric charge during the LCO has been depicted in Figure 47 for different pitch capacitance of the piezoelectric patch which indicates the load response of the smart wing is independent on the pitch capacitance of the piezoelectric patch.

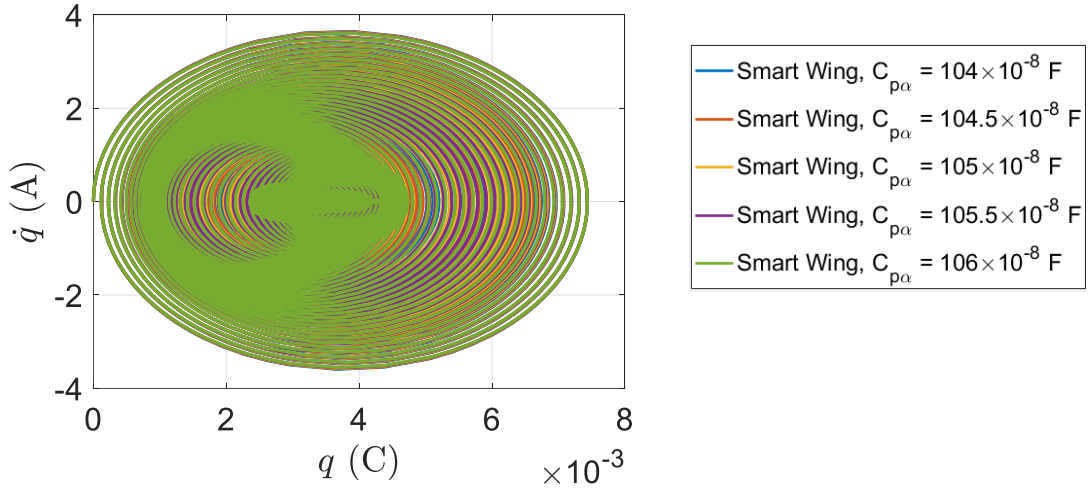

Fig. 47 Phase plane for pitch electric current versus pitch electric charge for different $C_{p\alpha}$

5.5 Effect of R_α on stall flutter alleviation and elimination

As the fifth parameter, we consider R_α with different values as 5, 10, 15, 20, and 25 Ω. However, having different pitch resistance of piezoelectric material for the shunt piezoelectric patch cannot create any difference on the smart wing pre-simulation results obtaining the aerodynamic state initial values discussed in Section 4, as indicated in Figure 48.

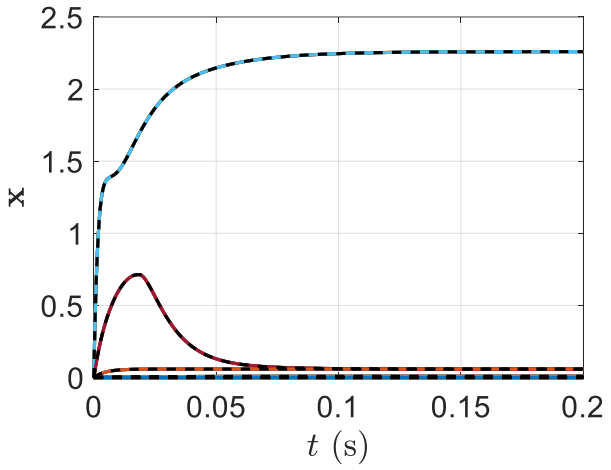

Fig. 48 Aerodynamic state response versus time during pre-simulation for different R_α

It is clear that changing the pitch coupling coefficient of the piezoelectric patch does not change the aerodynamic state response versus time during pre-simulation as all of the aerodynamic states converge to constant values after 0.2 s, as shown in Figure 48. In other words, both smart and regular wings have the same aerodynamic state response during pre-simulation time interval. Furthermore, pitch angle time response of the smart wing does not change with respect to the pitch resistance of the piezoelectric patch which indicates pitch angle time response of the smart wing is independent on the pitch resistance of the piezoelectric patch, as shown in Figure 49.

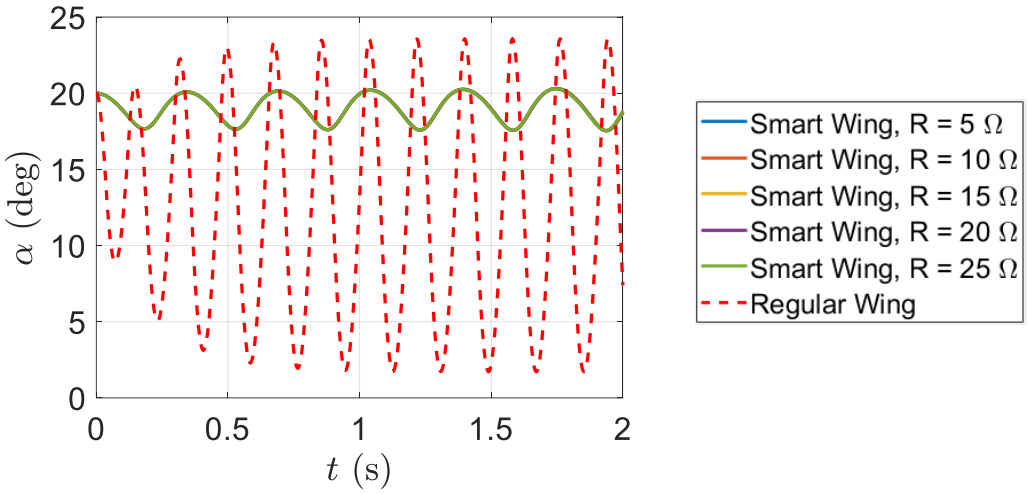

Fig. 49 Pitch angle time response for different R_α

Also, the load response versus pitch angle during the LCO has been depicted in Figure 50 for different pitch resistance of the piezoelectric patch which indicates the load response of the smart wing is independent on the pitch resistance of the piezoelectric patch.

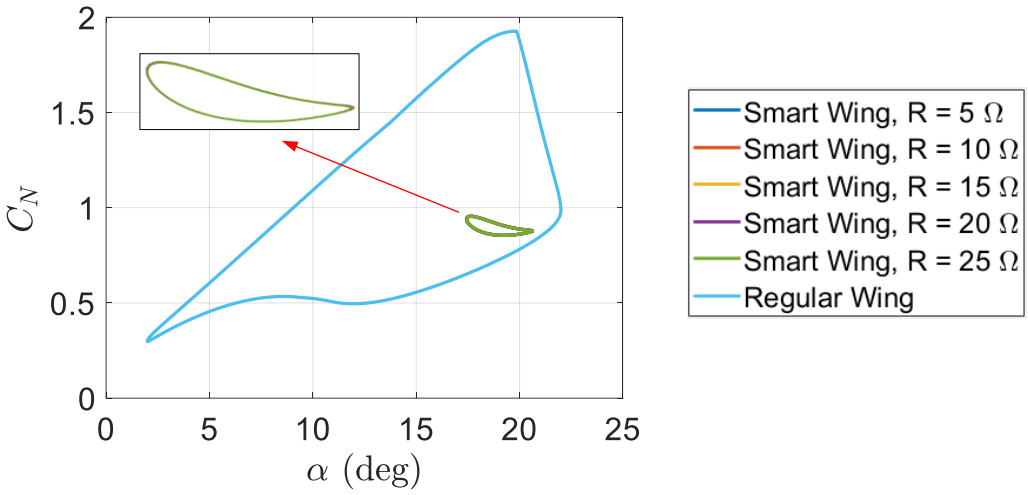

Fig. 50 Load response versus pitch angle for different R_α

Moreover, the pitching moment versus pitch angle during the LCO has been shown in Figure 51 for different pitch resistance of the piezoelectric patch which indicates the pitching moment of the smart wing is not dependent on the pitch resistance of the piezoelectric patch.

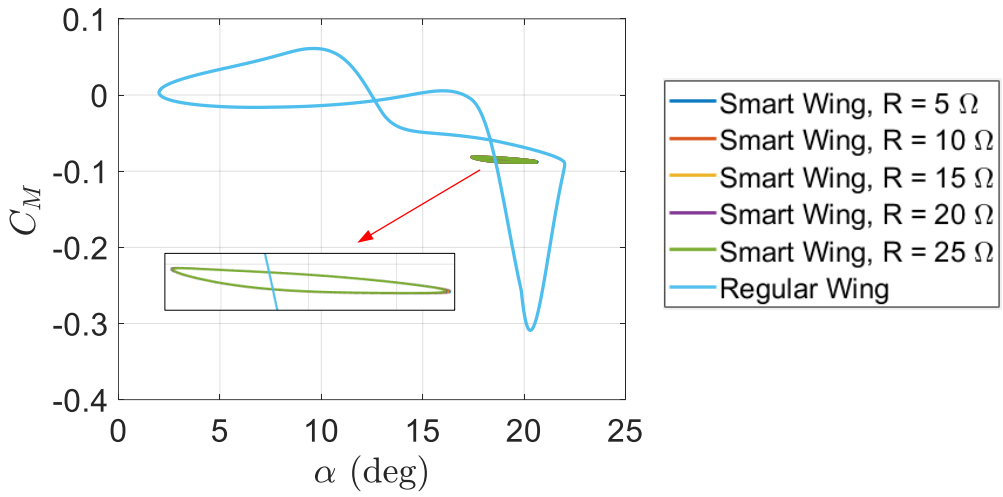

Fig. 51 Pitching moment versus pitch angle for different R_α

The pitching moment around the pitching axis versus pitch angle during the LCO has also been depicted in Figure 52 for different pitch resistance of the piezoelectric patch which indicates the pitching moment around the pitching axis of the smart wing is independent on the pitch resistance of the piezoelectric patch.

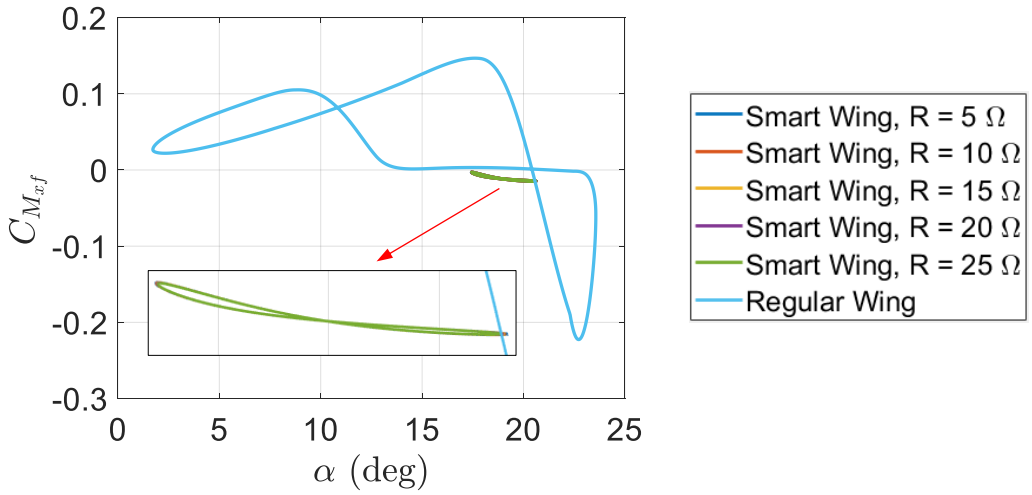

Fig. 52 Pitching moment around the pitching axis versus pitch angle for different R_α

Furthermore, the phase plane for pitching velocity versus pitch angle during the LCO has been shown in Figure 53 for different pitch resistance of the piezoelectric patch which indicates the

phase plane for pitching velocity of the smart wing is not dependent on the pitch resistance of the piezoelectric patch.

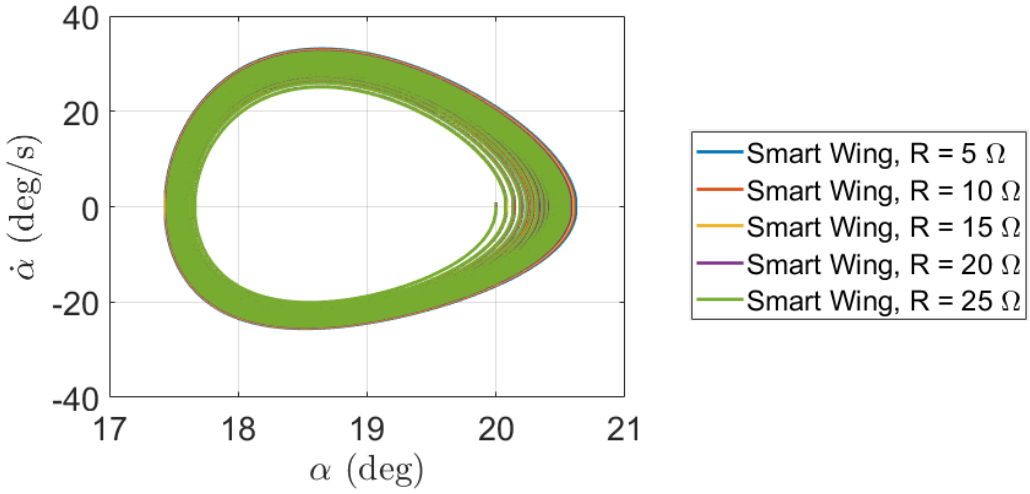

Fig. 53 Phase plane for pitching velocity versus pitch angle for different R_α

Finally, the phase plane for pitch electric current versus pitch electric charge during the LCO has been depicted in Figure 54 for different pitch resistance of the piezoelectric patch which indicates the load response of the smart wing is independent on the pitch resistance of the piezoelectric patch.

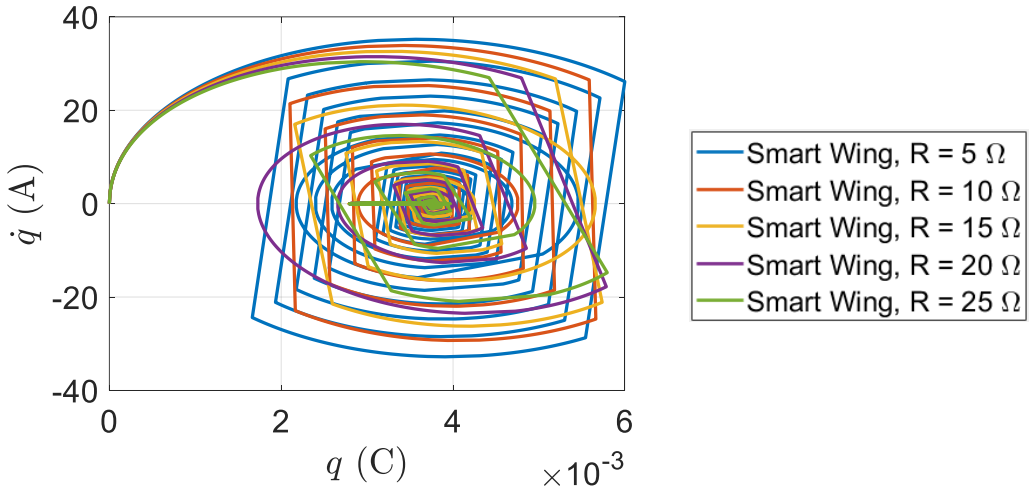

Fig. 54 Phase plane for pitch electric current versus pitch electric charge for different R_α

In summary, according to the parametric study results, only phase plane can be affected with respect to different parameters value. However, other results remain unchanged, as shown in this sub-section.

5.6 Effect of electrical system frequency on stall flutter alleviation and elimination

As the sixth parameter, we consider the effect of the electrical system frequency which needs to derive first the equations of motion for the electrical system, as follows

$$\begin{cases} \ddot{\alpha} + 2\zeta\omega_n\dot{\alpha} + {\omega_n}^2\alpha - \dfrac{\beta_\alpha}{I_\alpha}q_\alpha = \dfrac{1}{2}\dfrac{\rho U^2 c^2}{I_\alpha}\left(c_m + \dfrac{1}{2}(a+1/2)c_n\right) \\ \ddot{q}_\alpha + 2\zeta_e\omega_e\dot{q}_\alpha + {\omega_e}^2 q_\alpha - C_{p_\alpha}\beta_\alpha{\omega_e}^2\left(x_f - x_p\right)\alpha = 0 \end{cases} \tag{24}$$

where $\zeta = C_\alpha/\left(2\sqrt{K_\alpha I_\alpha}\right)$ is the structural damping ratio, ω_n the structural natural frequency, ζ_e the electrical damping ration, and ω_e the electrical natural frequency. Assuming x_1 to x_{12} as the aerodynamic load states which are explained later and $x_{13} = \dot{\alpha}$, $x_{14} = \dot{q}_\alpha$, $x_{15} = \alpha$, and $x_{16} = q_\alpha$, Eq. (24) is written as first-order differential equations, as follows

$$\begin{cases} \dot{x}_{13} = -2\zeta\omega_n x_{13} - {\omega_n}^2 x_{15} + \dfrac{\beta_\alpha}{I_\alpha}x_{16} - \dfrac{1}{2}\dfrac{\rho U^2 c}{I_\alpha}c_n/\cos\alpha \\ \dot{x}_{14} = -2\zeta_e\omega_e x_{14} - {\omega_e}^2 x_{16} + C_{p_\alpha}\beta_\alpha{\omega_e}^2\left(x_f - x_p\right)x_{15} \\ \qquad\qquad + \dfrac{1}{2}\dfrac{\rho U^2 c}{I_\alpha}(cc_m + b(a+1/2)c_n) \\ \dot{x}_{15} = x_{13} \\ \dot{x}_{16} = x_{14} \end{cases} \tag{25}$$

The new form of the equation of motion can be written as Eq. (3) because of having nonlinear function of $\ddot{\alpha}$. Equation (3) can be written in first order form as Eq. (6), where **x** is a 16×1 state vector including the 12 Leishman-Beddoes states, $x_{13} = \dot{\alpha}$, $x_{14} = \dot{q}$, $x_{15} = \alpha$, and $x_{16} = q$. The general form of the equations of motion can be represented as Eq. (7), where $\boldsymbol{A}$ the structural mass and inductance matrix, $\dot{\boldsymbol{y}} = [\ddot{\alpha} \quad \ddot{q}]^T$ is the pitching acceleration and the rate of the pitch electrical current vector, $\boldsymbol{C}$ is the pitching structural damping and pitch resistance of piezoelectric material matrix, $\boldsymbol{y} = [\dot{\alpha} \quad \dot{q}]^T$ is the pitching velocity and pitch electrical current

vector, $\boldsymbol{E}$ is the pitching structural stiffness, pitch electromechanical coupling and pitch capacitance of piezoelectric material matrix, $\boldsymbol{y} = [\alpha \quad q]^T$ is the pitching angle and pitch electric charge vector, and $\boldsymbol{F}$ is the aerodynamic load vector. Moreover, $\boldsymbol{A}$, $\boldsymbol{C}$, and $\boldsymbol{E}$ matrices, and $\boldsymbol{F}$ vector are given by

$$\boldsymbol{A} = \begin{bmatrix} 1 & 0 \\ 0 & 1 \end{bmatrix} \tag{26}$$

$$\boldsymbol{C} = \begin{bmatrix} 2\zeta\omega_n & 0 \\ 0 & 2\zeta_e\omega_e \end{bmatrix} \tag{27}$$

$$\boldsymbol{E} = \begin{bmatrix} {\omega_n}^2 & -\dfrac{\beta_\alpha}{I_\alpha} \\ -C_{p\alpha}\beta_\alpha{\omega_e}^2(x_f - x_p) & {\omega_e}^2 \end{bmatrix} \tag{28}$$

$$\boldsymbol{F} = \frac{1}{2}\frac{\rho U^2 c}{I_\alpha}\begin{bmatrix} -c_n/\cos\alpha \\ cc_m + b(a+1/2)c_n \end{bmatrix} \tag{29}$$

Considering Eqs. (26)-(29), the equations of motion, Eq. (25), can be written as

$$\begin{bmatrix} \dot{x}_{13} \\ \dot{x}_{14} \\ \dot{x}_{15} \\ \dot{x}_{16} \end{bmatrix} = \begin{bmatrix} -\boldsymbol{A}^{-1}\boldsymbol{C} & -\boldsymbol{A}^{-1}\boldsymbol{E} \\ \boldsymbol{I} & \boldsymbol{0} \end{bmatrix}\begin{bmatrix} x_{13} \\ x_{14} \\ x_{15} \\ x_{16} \end{bmatrix} + \frac{1}{2}\frac{\rho U^2 c}{I_\alpha}\begin{bmatrix} -c_n/\cos\alpha \\ cc_m + b(a+1/2)c_n \\ 0 \\ 0 \end{bmatrix} \tag{30}$$

Because of the nonlinearity in $\dot{x}_{13}$, Eq. (30) needs to be solved iteratively by considering the Runge-Kutta approach and using a simple implicit algorithm, as explained previously.

We conduct an aeroelastic analysis on the following smart wing, Table 6, to represent the effect of the piezoelectric patch on stall flutter alleviation.

Table 6 Smart wing characteristics for electrical system

$\omega_n = 2500\ \mathrm{N/rad}$	Structural natural frequency
$\zeta = 0.0157$	Structural damping ratio
$I_\alpha = 2.5330\ \mathrm{N/s^2}$	Mass moment of inertia
$\beta_\alpha = 1.2438 \times 10^5\ \mathrm{C/mF}$	Pitch electromechanical coupling

$\omega_e = 9272.783982$ rad/s	Electrical natural frequency
$\zeta_e = 0.0539$	Electrical damping ration

We consider the electrical natural frequency, ω_e, with different values as 9260, 9270, 9272.783982, 9280, and 9280 rad/s. However, having different electrical natural frequency of piezoelectric material for the shunt piezoelectric patch cannot create any difference on the smart wing pre-simulation results obtaining the aerodynamic state initial values discussed in Section 4, as indicated in Figure 55.

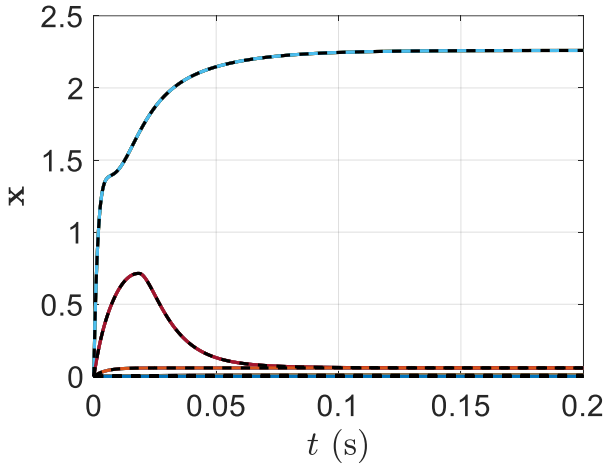

Fig. 55 Aerodynamic state response versus time during pre-simulation for different ω_e

It is clear that changing the different electrical natural frequency of the piezoelectric patch does not change the aerodynamic state response versus time during pre-simulation as all of the aerodynamic states converge to constant values after 0.2 s, as shown in Figure 55. In other words, both smart and regular wings have the same aerodynamic state response during pre-simulation time interval. Furthermore, pitch angle time response of the smart wing does not change with respect to the electrical natural frequency of the piezoelectric patch which indicates pitch angle time response of the smart wing is independent of the electrical natural frequency of the piezoelectric patch, as shown in Figure 56.

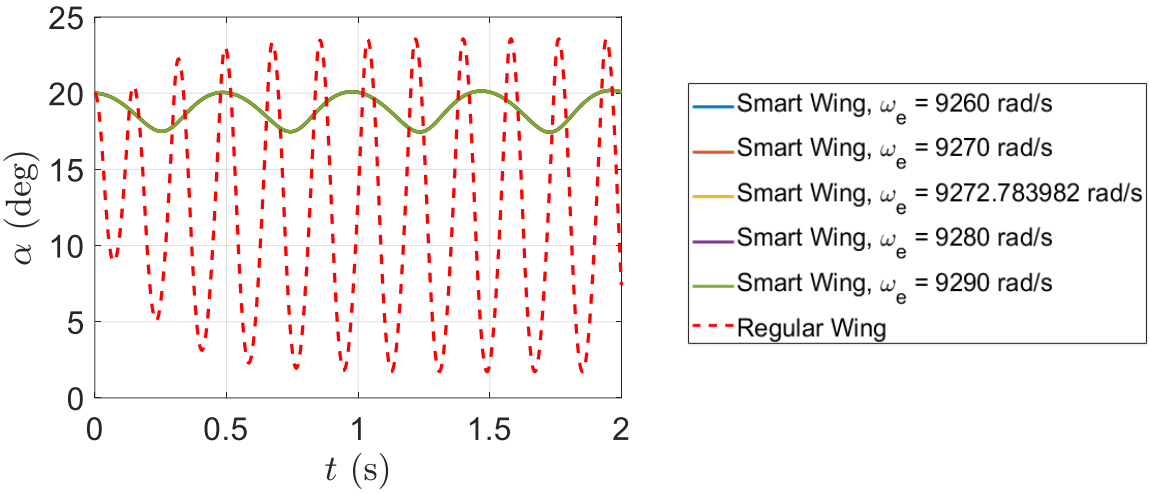

Fig. 56 Pitch angle time response for different ω_e

Also, the load response versus pitch angle during the LCO has been depicted in Figure 57 for different electrical natural frequency of the piezoelectric patch which indicates the load response of the smart wing is independent on the electrical natural frequency of the piezoelectric patch.

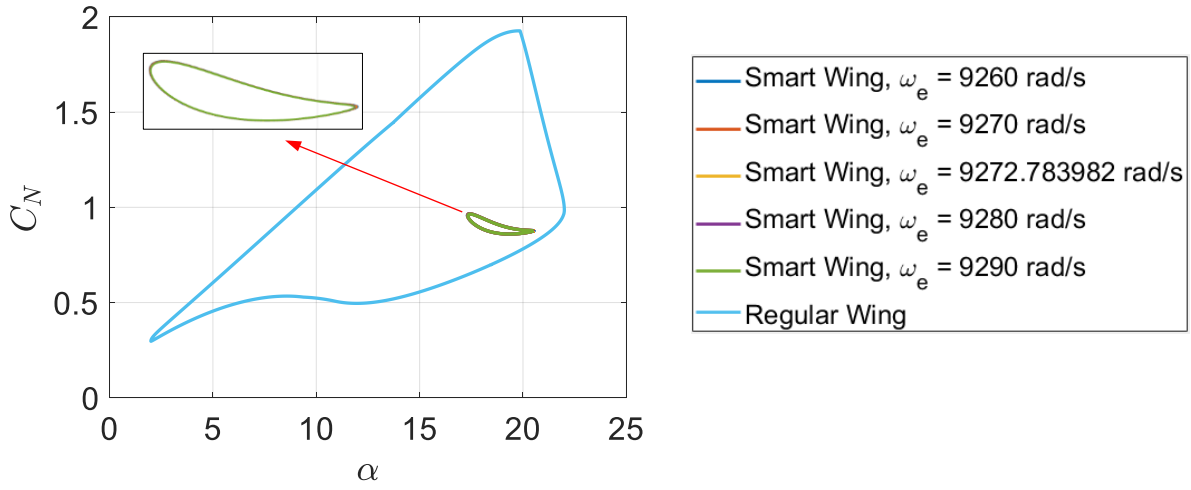

Fig. 57 Load response versus pitch angle for different ω_e

Moreover, the pitching moment versus pitch angle during the LCO has been shown in Figure 58 for the different electrical natural frequency of the piezoelectric patch which indicates the

pitching moment of the smart wing is not dependent on the electrical natural frequency of the piezoelectric patch.

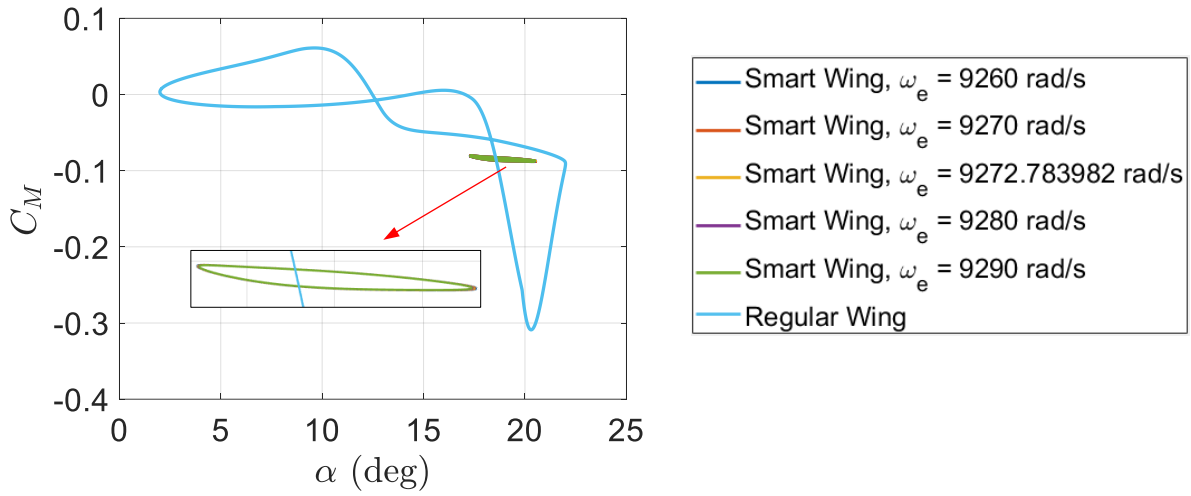

Fig. 58 Pitching moment versus pitch angle for different ω_e

The pitching moment around the pitching axis versus pitch angle during the LCO has also been depicted in Figure 59 for different electrical natural frequency of the piezoelectric patch which indicates the pitching moment around the pitching axis of the smart wing is independent on the electrical natural frequency of the piezoelectric patch.

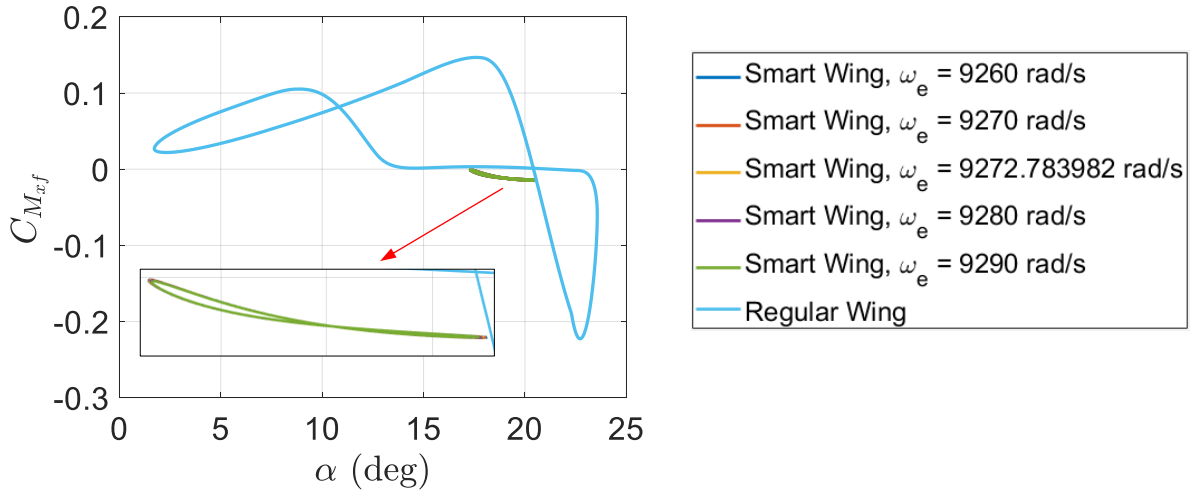

Fig. 59 Pitching moment around the pitching axis versus pitch angle for different ω_e

Furthermore, the phase plane for pitching velocity versus pitch angle during the LCO has been shown in Figure 60 for different electrical natural frequency of the piezoelectric patch which indicates the phase plane for pitching velocity of the smart wing is not dependent on the electrical natural frequency of the piezoelectric patch.

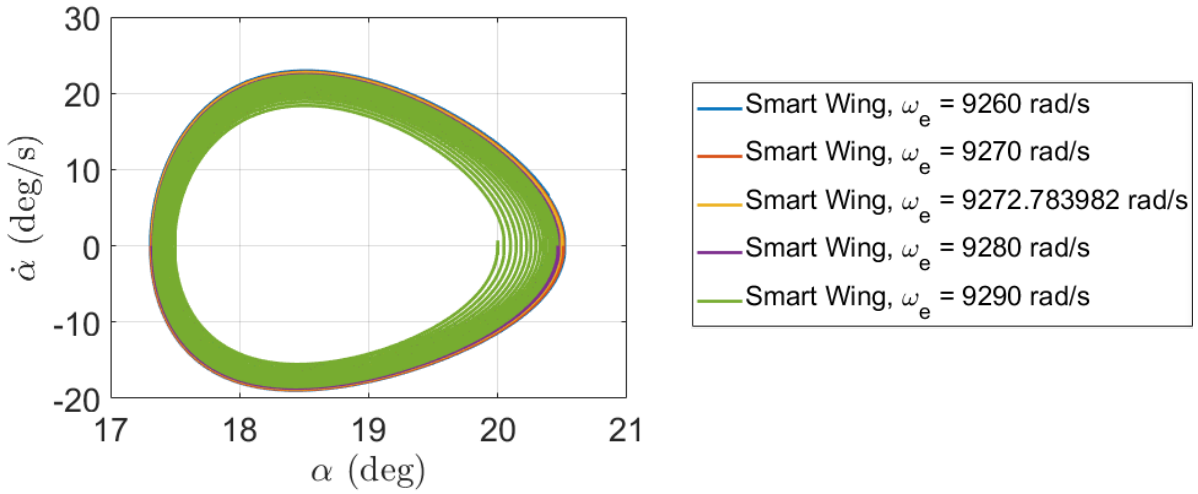

Fig. 60 Phase plane for pitching velocity versus pitch angle for different ω_e

Finally, the phase plane for pitch electric current versus pitch electric charge during the LCO has been depicted in Figure 61 for different electrical natural frequency of the piezoelectric patch which indicates the load response of the smart wing is independent on the electrical natural frequency of the piezoelectric patch.

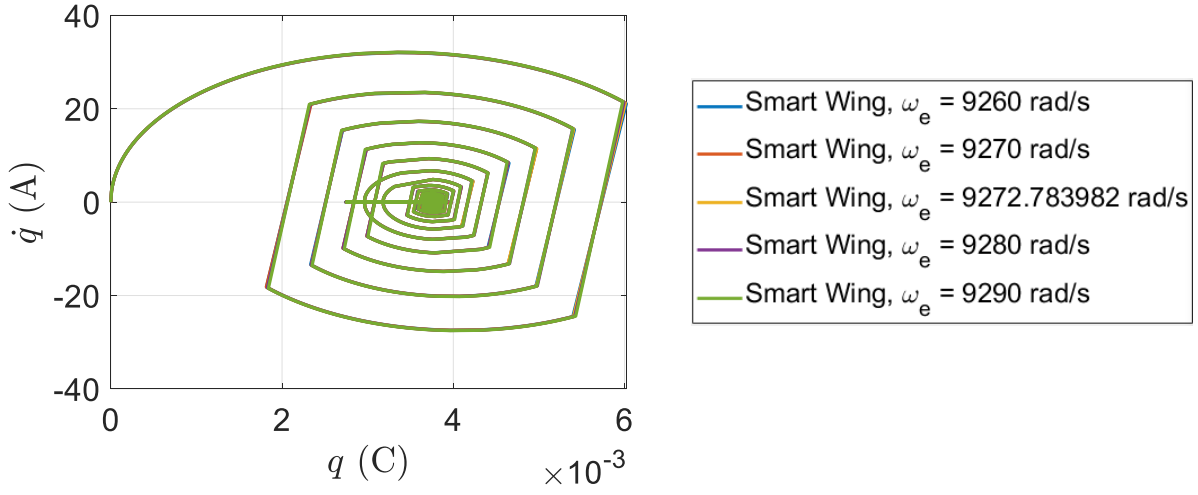

Fig. 61 Phase plane for pitch electric current versus pitch electric charge for different ω_e

In summary, according to the parametric study results, the electrical natural frequency results cannot be affected with respect to different parameters values and remain unchanged, as shown in this sub-section.

5.7 Effect of electrical system damping on stall flutter alleviation and elimination

As the seventh parameter, we consider the effect of the electrical system frequency by considering the electrical damping, ζ_e, with different values as 0.0519, 0.0529, 0.0539, 0.0549, and 0.0559. However, having different electrical damping of piezoelectric material for the shunt piezoelectric patch cannot create any difference on the smart wing pre-simulation results obtaining the aerodynamic state initial values discussed in Section 4, as indicated in Figure 62.

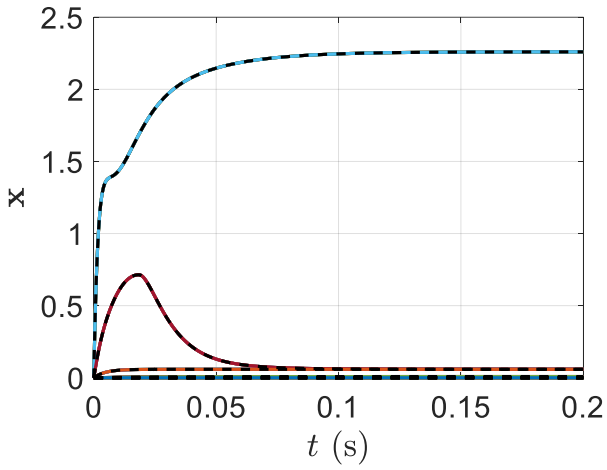

Fig. 62 Aerodynamic state response versus time during pre-simulation for different ζ_e

It is clear that changing the different electrical damping of the piezoelectric patch does not change the aerodynamic state response versus time during pre-simulation as all of the aerodynamic states converge to constant values after 0.2 s, as shown in Figure 63. In other words, both smart and regular wings have the same aerodynamic state response during pre-simulation time interval. Furthermore, pitch angle time response of the smart wing does not

change with respect to the electrical damping of the piezoelectric patch which indicates pitch angle time response of the smart wing is independent on the electrical damping of the piezoelectric patch, as shown in Figure 63.

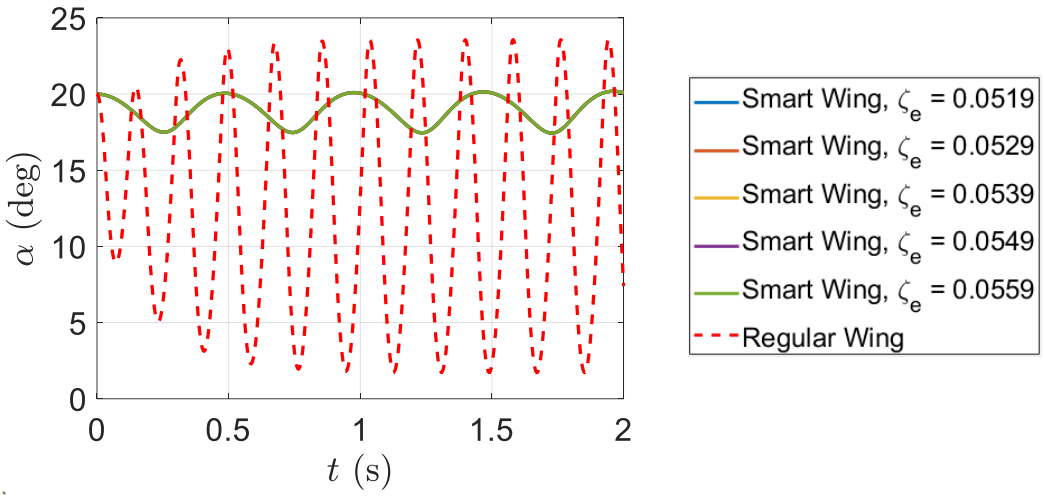

Fig. 63 Pitch angle time response for different ζ_e

Also, the load response versus pitch angle during the LCO has been depicted in Figure 64 for different electrical damping of the piezoelectric patch which indicates the load response of the smart wing is independent on the electrical damping of the piezoelectric patch.

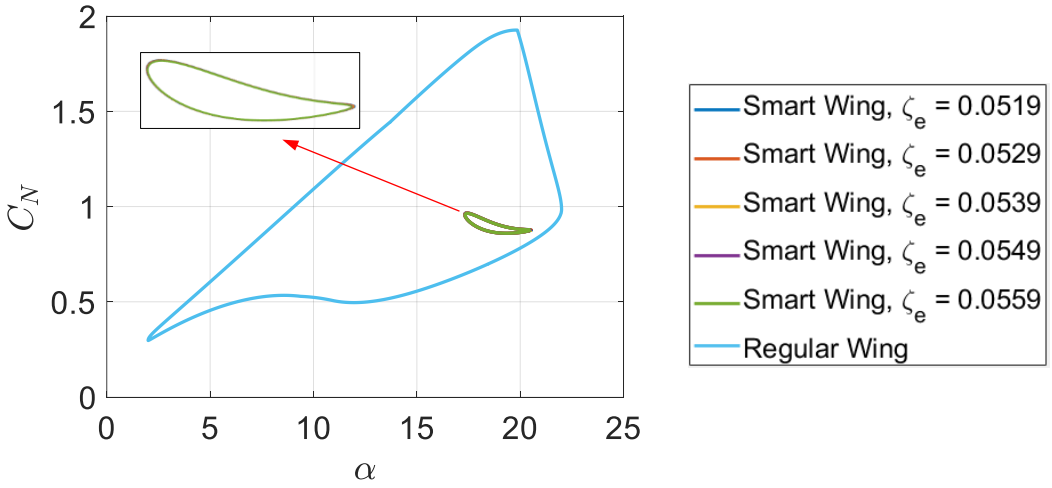

Fig. 64 Load response versus pitch angle for different ζ_e

Moreover, the pitching moment versus pitch angle during the LCO has been shown in Figure 65 for the different electrical dampening of the piezoelectric patch which indicates the pitching moment of the smart wing is not dependent on the electrical dampening of the piezoelectric patch.

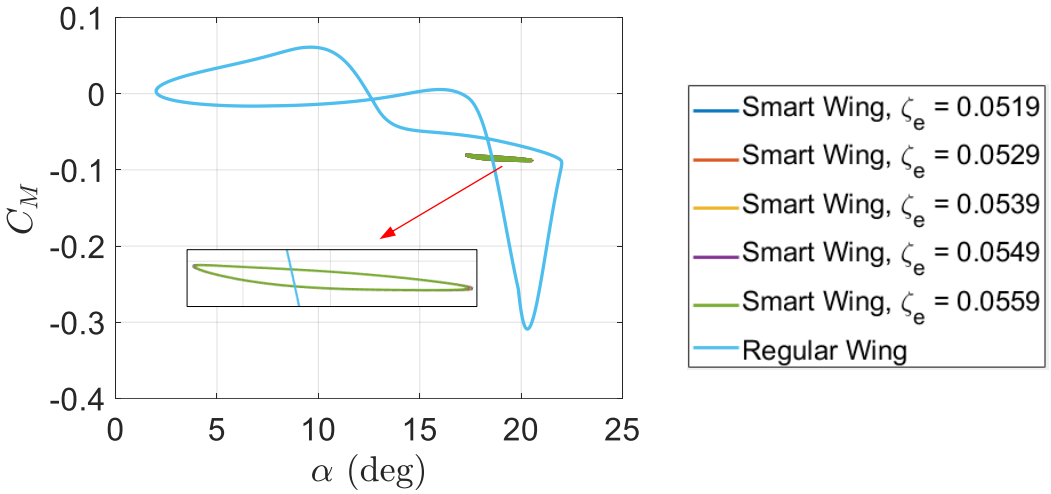

Fig. 65 Pitching moment versus pitch angle for different ζ_e

The pitching moment around the pitching axis versus pitch angle during the LCO has also been depicted in Figure 66 for different electrical damping of the piezoelectric patch which indicates the pitching moment around the pitching axis of the smart wing is independent on the electrical damping of the piezoelectric patch.

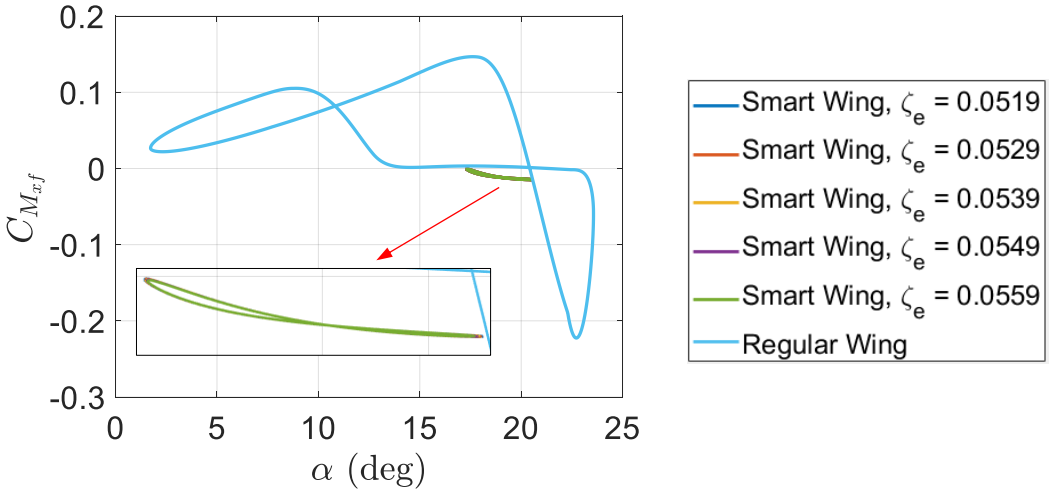

Fig. 66 Pitching moment around the pitching axis versus pitch angle for different ζ_e

Furthermore, the phase plane for pitching velocity versus pitch angle during the LCO has been shown in Figure 67 for different electrical damping of the piezoelectric patch which indicates the phase plane for pitching velocity of the smart wing is not dependent on the electrical damping of the piezoelectric patch.

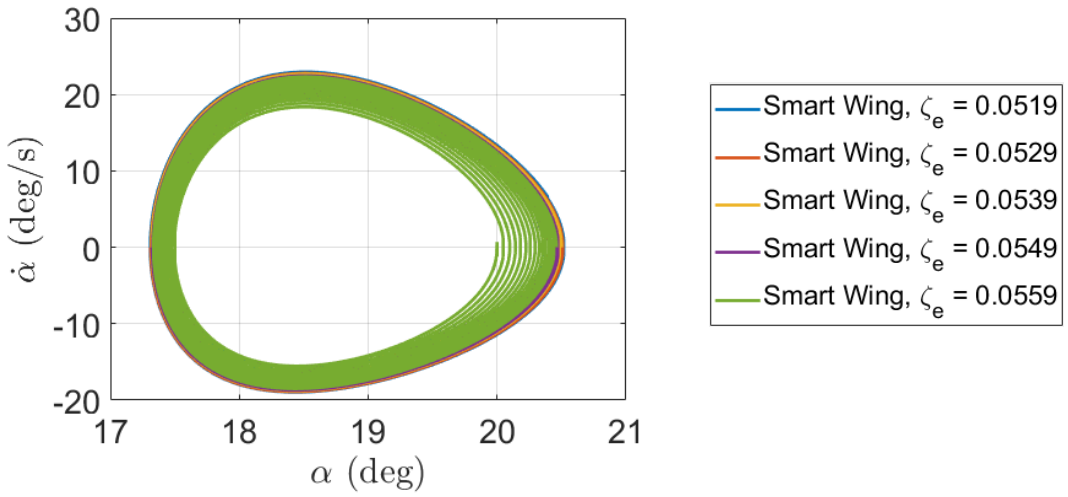

Fig. 67 Phase plane for pitching velocity versus pitch angle for different ζ_e

Finally, the phase plane for pitch electric current versus pitch electric charge during the LCO has been depicted in Figure 68 for different electrical damping of the piezoelectric patch which indicates the load response of the smart wing is independent on the electrical damping of the piezoelectric patch.

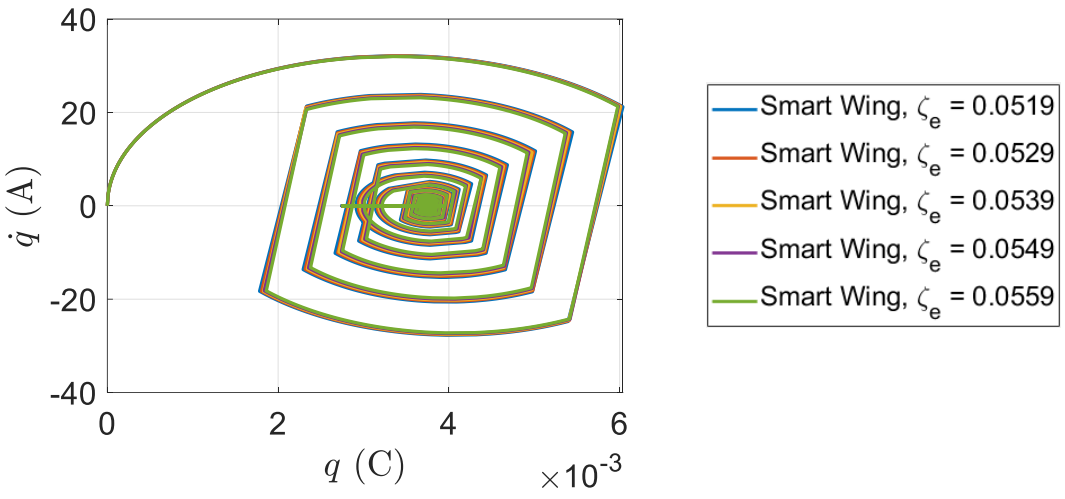

Fig. 68 Phase plane for pitch electric current versus pitch electric charge for different ζ_e

In summary, according to the parametric study results, the electrical system results cannot be affected with respect to different electrical damping values and remain unchanged, as shown in this sub-section.

5.8 Effect of electrical system impedance on stall flutter alleviation and elimination

As the eighth parameter, we consider the effect of the electrical system impedance, $z = V/I = 1/R_\alpha$, by considering different values as 0.1, 0.2, 0.3, 0.4, and 0.5. However, having different impedance of piezoelectric material for the shunt piezoelectric patch cannot create any difference on the smart wing pre-simulation results obtaining the aerodynamic state initial values discussed in Section 4, as indicated in Figure 69.

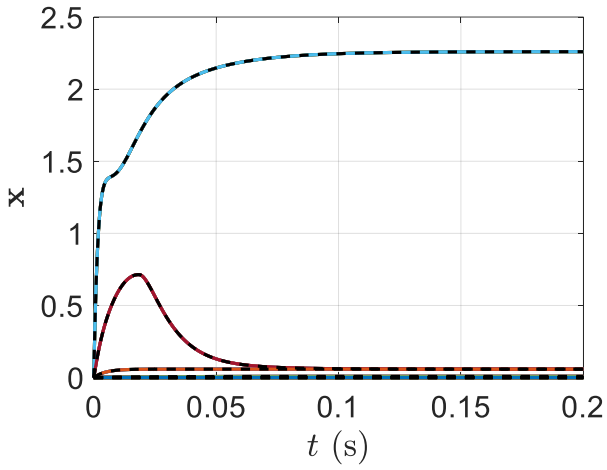

Fig. 69 Aerodynamic state response versus time during pre-simulation for different *z*

It is clear that changing the different impedance of the piezoelectric patch does not change the aerodynamic state response versus time during pre-simulation as all of the aerodynamic states converge to constant values after 0.2 s, as shown in Figure 69. In other words, both smart and regular wings have the same aerodynamic state response during pre-simulation time interval. Furthermore, pitch angle time response of the smart wing does not change with respect to the impedance of the piezoelectric patch which indicates pitch angle time response of the smart wing is independent on the impedance of the piezoelectric patch, as shown in Figure 70.

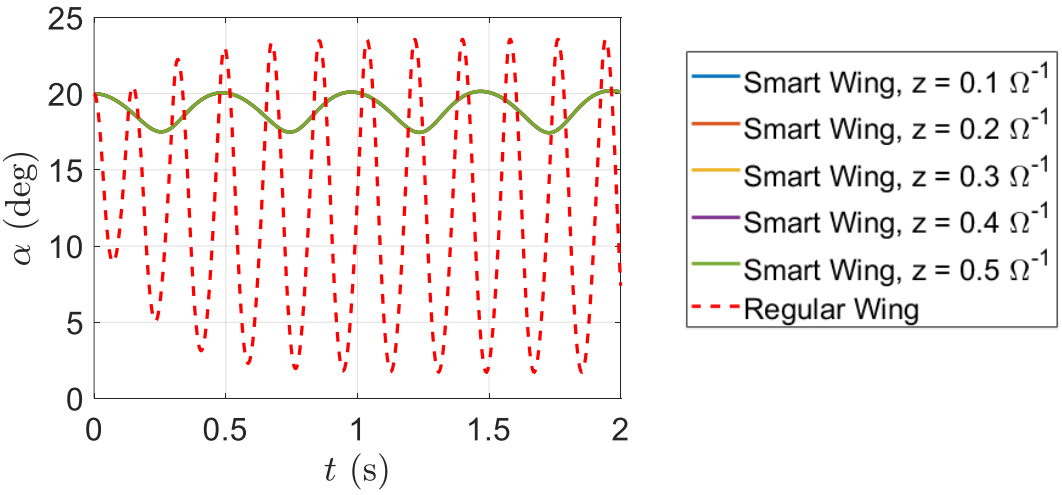

Fig. 70 Pitch angle time response for different *z*

Also, the load response versus pitch angle during the LCO has been depicted in Figure 71 for different impedance of the piezoelectric patch which indicates the load response of the smart wing is independent on the impedance of the piezoelectric patch.

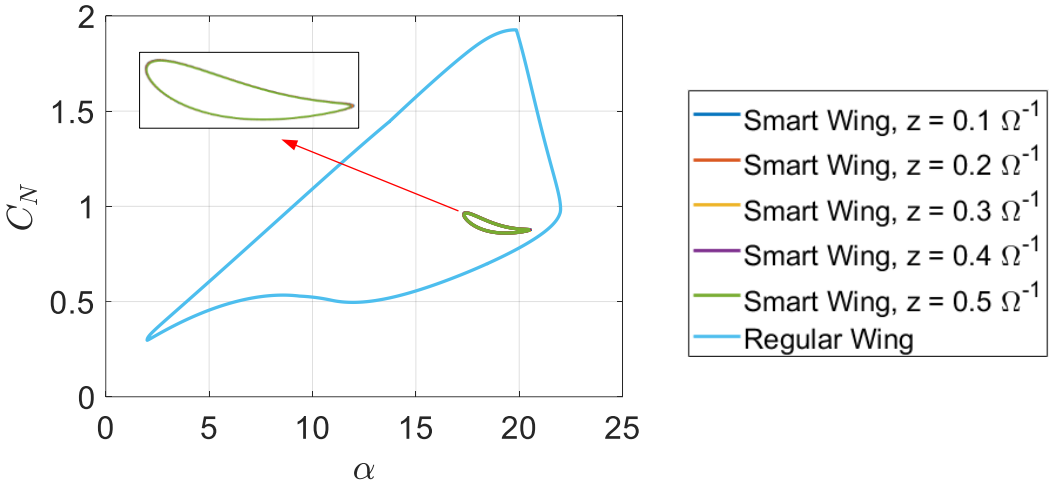

Fig. 71 Load response versus pitch angle for different *z*

Moreover, the pitching moment versus pitch angle during the LCO has been shown in Figure 72 for the different impedance of the piezoelectric patch which indicates the pitching moment of the smart wing is not dependent on the impedance of the piezoelectric patch.

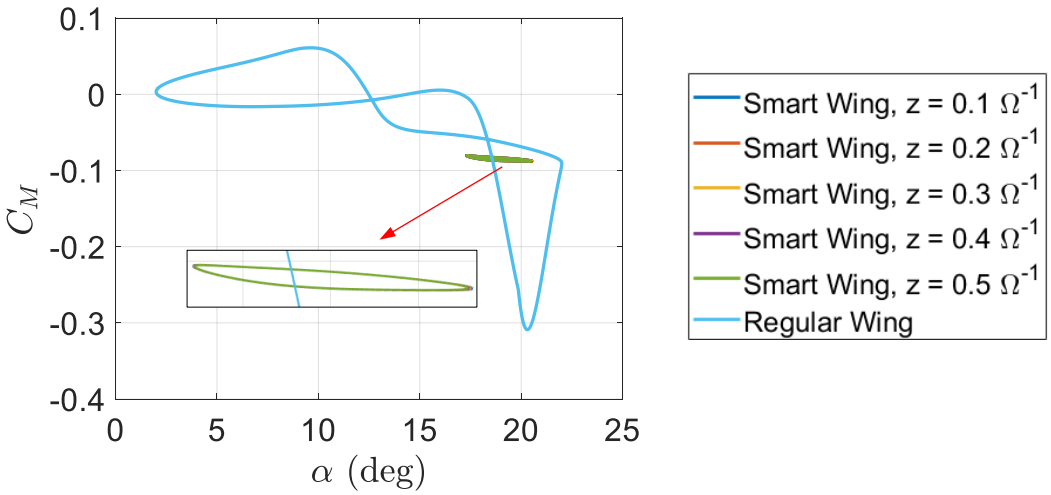

Fig. 72 Pitching moment versus pitch angle for different *z*

The pitching moment around the pitching axis versus pitch angle during the LCO has also been depicted in Figure 73 for different impedance of the piezoelectric patch which indicates the pitching moment around the pitching axis of the smart wing is independent on the impedance of the piezoelectric patch.

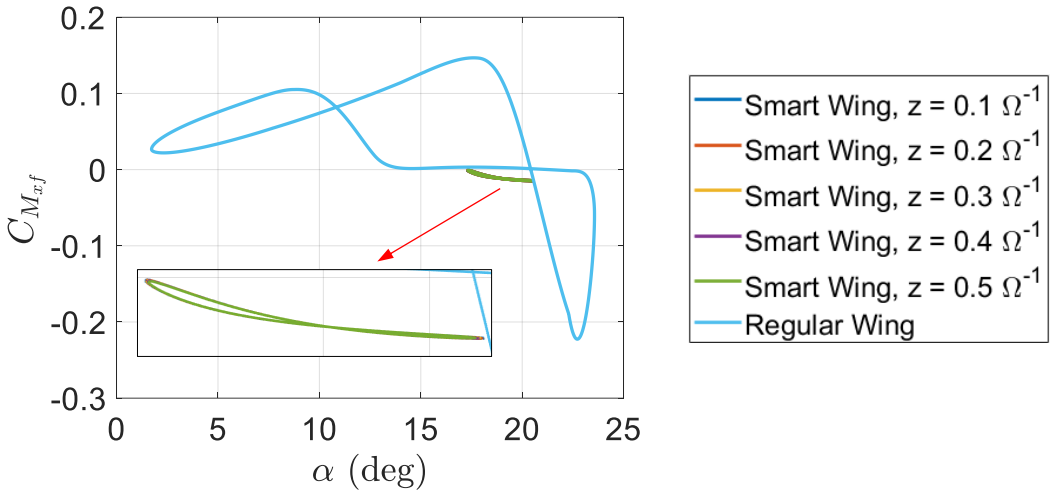

Fig. 73 Pitching moment around the pitching axis versus pitch angle for different *z*

Furthermore, the phase plane for pitching velocity versus pitch angle during the LCO has been shown in Figure 74 for different impedance of the piezoelectric patch which indicates the phase plane for pitching velocity of the smart wing is not dependent on the impedance of the piezoelectric patch.

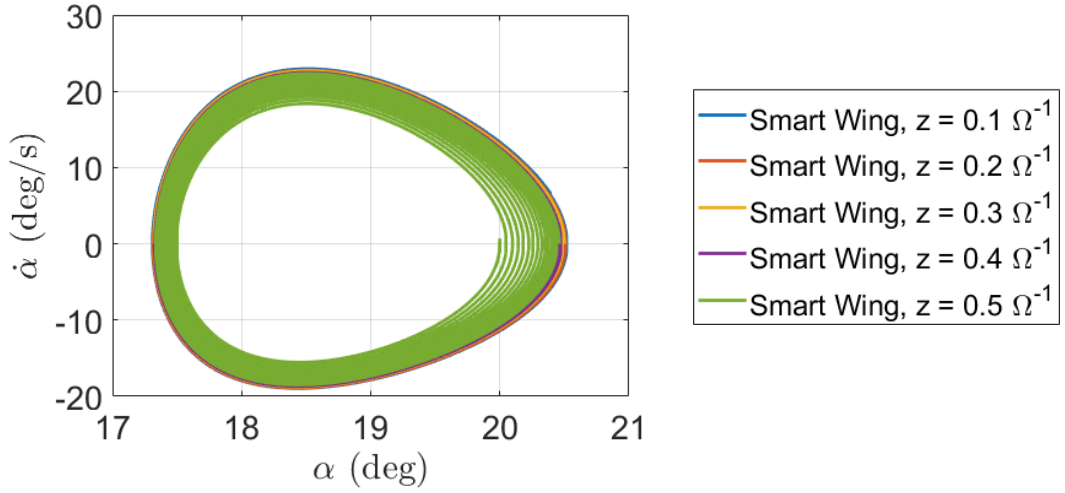

Fig. 74 Phase plane for pitching velocity versus pitch angle for different z

Finally, the phase plane for pitch electric current versus pitch electric charge during the LCO has been depicted in Figure 75 for different impedance of the piezoelectric patch which indicates the load response of the smart wing is independent on the impedance of the piezoelectric patch.

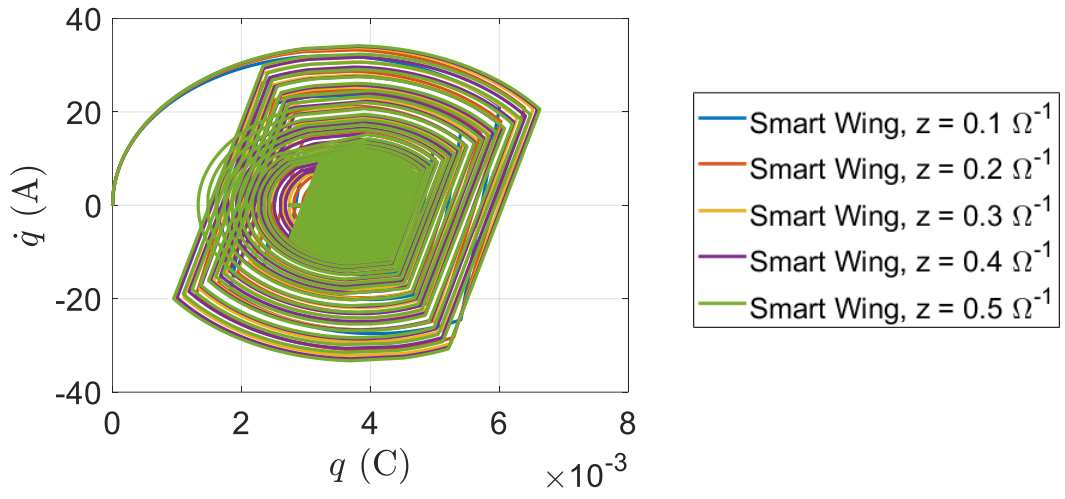

Fig. 75 Phase plane for pitch electric current versus pitch electric charge for different z

In summary, according to the parametric study results, the electrical system results cannot be affected with respect to different impedance values and remain unchanged, as shown in this sub-section.

5.9 Effect of electrical system coupling on stall flutter alleviation and elimination

As the ninth parameter, we consider the effect of the electrical system coupling, β_α, by considering different values as 1.2418×10^5, 1.2428×10^5, 1.2438×10^5, 1.2448×10^5, and 1.2458×10^5 C/mF. However, having different coupling of piezoelectric material for the shunt piezoelectric patch cannot create any difference on the smart wing pre-simulation results obtaining the aerodynamic state initial values discussed in Section 4, as indicated in Figure 76.

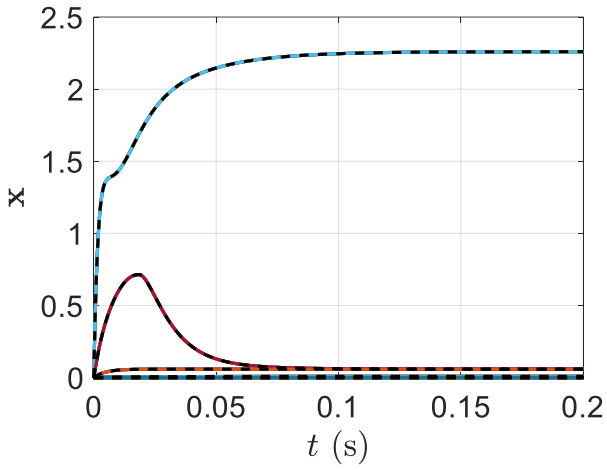

Fig. 76 Aerodynamic state response versus time during pre-simulation for different β_α

It is clear that changing the different coupling of the piezoelectric patch does not change the aerodynamic state response versus time during pre-simulation as all of the aerodynamic states converge to constant values after 0.2 s, as shown in Figure 76. In other words, both smart and regular wings have the same aerodynamic state response during pre-simulation time interval. Furthermore, pitch angle time response of the smart wing change with respect to the coupling of the piezoelectric patch which indicates pitch angle time response of the smart wing is dependent on the coupling of the piezoelectric patch, as shown in Figure 77.

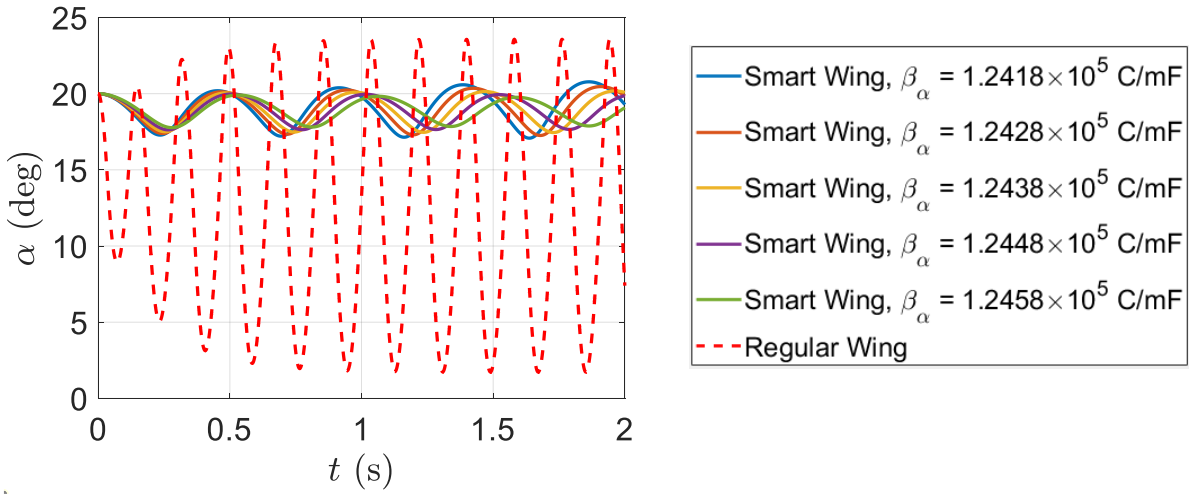

Fig. 77 Pitch angle time response for different β_α

Also, the load response versus pitch angle during the LCO has been depicted in Figure 78 for different coupling of the piezoelectric patch which indicates the load response of the smart wing is dependent on the coupling of the piezoelectric patch.

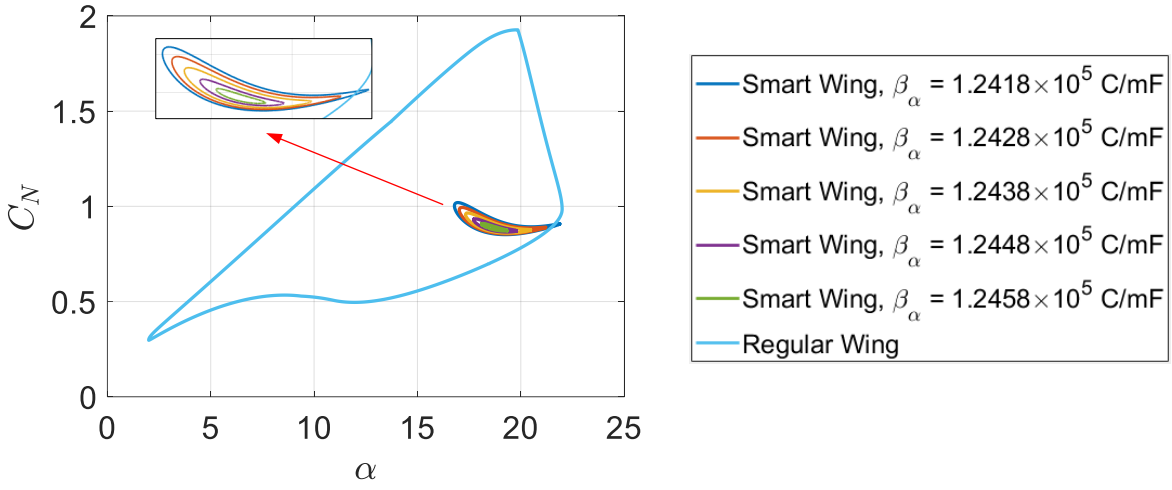

Fig. 78 Load response versus pitch angle for different β_α

Moreover, the pitching moment versus pitch angle during the LCO has been shown in Figure 79 for the different coupling of the piezoelectric patch which indicates the pitching moment of the smart wing is dependent on the coupling of the piezoelectric patch.

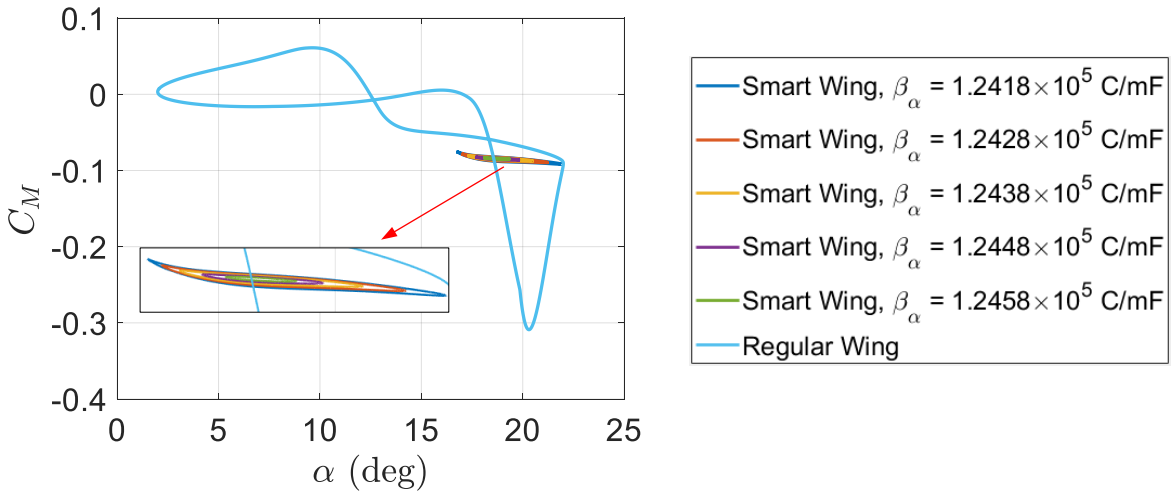

Fig. 79 Pitching moment versus pitch angle for different β_α

The pitching moment around the pitching axis versus pitch angle during the LCO has also been depicted in Figure 80 for different coupling of the piezoelectric patch which indicates the pitching moment around the pitching axis of the smart wing is dependent on the coupling of the piezoelectric patch.

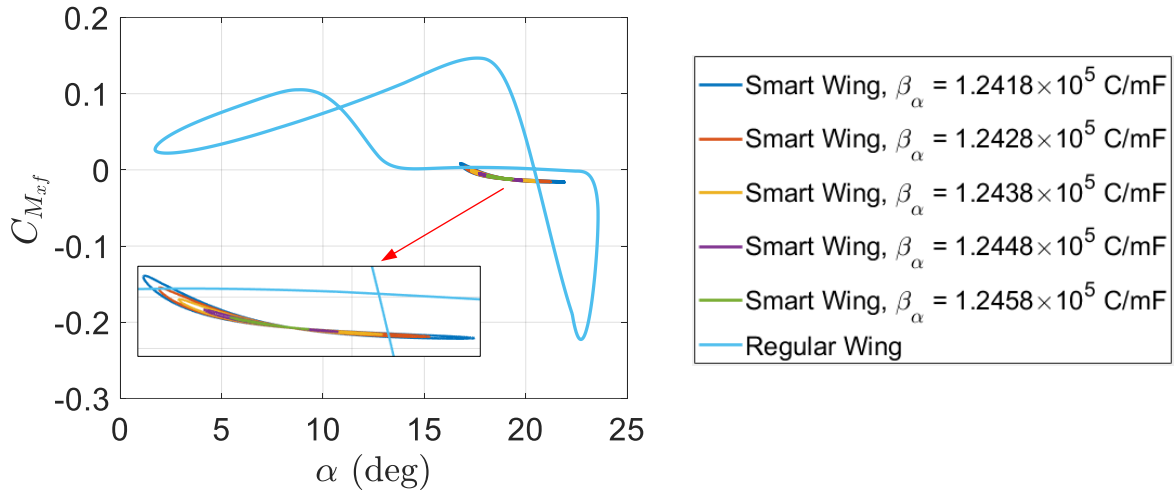

Fig. 80 Pitching moment around the pitching axis versus pitch angle for different β_α

Furthermore, the phase plane for pitching velocity versus pitch angle during the LCO has been shown in Figure 81 for different coupling of the piezoelectric patch which indicates the phase plane for pitching velocity of the smart wing is dependent on the coupling of the piezoelectric patch.

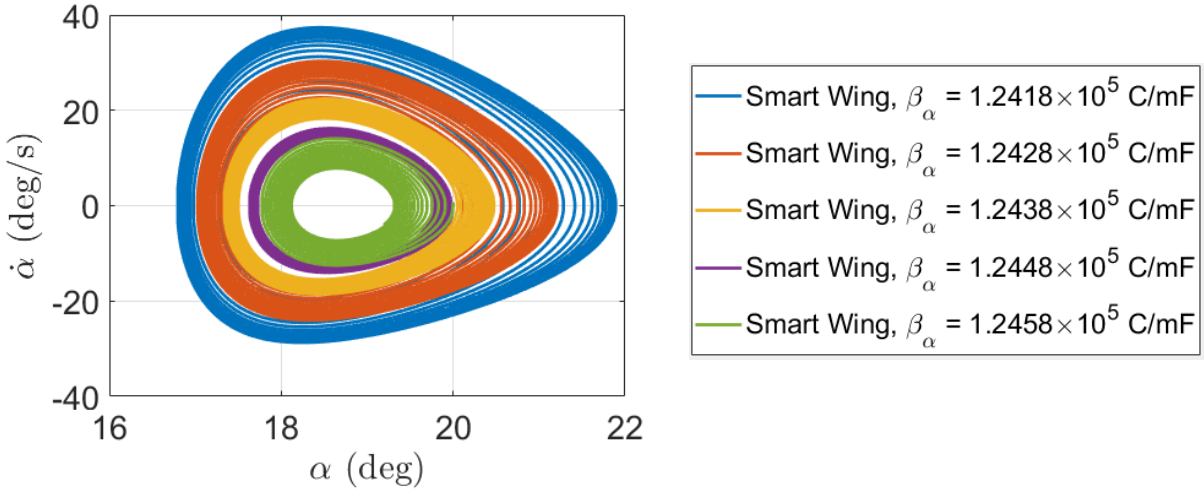

Fig. 81 Phase plane for pitching velocity versus pitch angle for different β_α

Finally, the phase plane for pitch electric current versus pitch electric charge during the LCO has been depicted in Figure 82 for different coupling of the piezoelectric patch which indicates the load response of the smart wing is independent on the coupling of the piezoelectric patch.

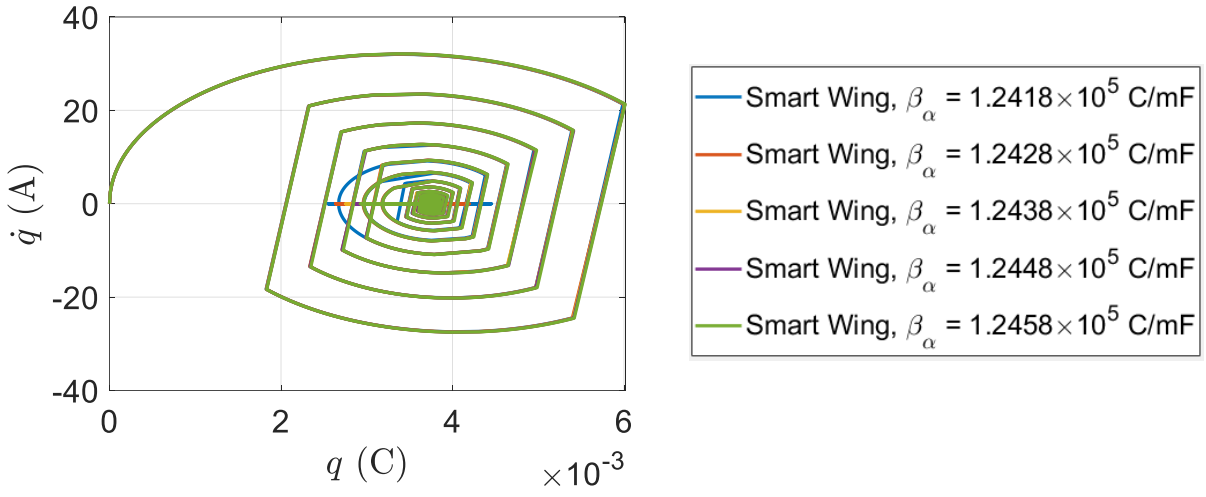

Fig. 82 Phase plane for pitch electric current versus pitch electric charge for different β_α

In summary, according to the parametric study results, the electrical system results can be affected with respect to different coupling values and remain unchanged, as shown in this sub-section.

6. Conclusions

In this paper, it has been shown that how the stall flutter phenomenon can be alleviated and eliminated using a small inductor by implementing a piezoelectric patch. The main contribution of this work is to represent a way to alleviate or eliminate the stall flutter on a regular 2D wing by using a passive aeroelastic control including piezoelectric patches and shunt circuits in which the size of the required inductance is small. The results indicate a considerable improvement in dynamic aeroelastic behavior of a 2D wing.

Appendix

A.1 Leishman-Beddoes model

If a wing has pitching around the quarter chord $x_f = c/4$, $\bar{\alpha}$ is equal to the geometric pitch angle, means $\bar{\alpha} = \alpha$. By considering these assumptions, an additional circulatory pitching moment term is added to the Leishman-Beddoes model as the following function

$$\phi_{q_M}^C = 1 - e^{-b_5 \beta^2 Ut/b} \tag{A.1}$$

where $b_5 = 0.5$. Because of having compressibility effects and added mass as impulsive loads, Leishman and Beddoes is related to non-circulatory contributions to the aerodynamic loads. These non-circulatory contributions can be represented as follows

$$\phi_{\bar{\alpha}}^I = e^{-t/K_{\bar{\alpha}} T_I} \tag{A.2a}$$

$$\phi_q^I = e^{-t/K_q T_I} \tag{A.2b}$$

$$\phi_{\bar{\alpha}_M}^I = A_3 e^{-t/b_3 K_{\bar{\alpha}_M} T_I} + A_4 e^{-t/b_4 K_{\bar{\alpha}_M} T_I} \tag{A.2c}$$

$$\phi_{q_M}^I = e^{-t/K_{q_M} T_I} \tag{A.2d}$$

where $T_I = c/a_\infty$, a_∞ is the free stream sound speed, the I superscript represents impulsive aerodynamic step responses and

$$K_{\bar{\alpha}} = \frac{1}{(1 - M_\infty) + \pi \beta M_\infty^2 (A_1 b_1 + A_2 b_2)} \tag{A.3a}$$

$$K_q = \frac{1}{(1 - M_\infty) + 2\pi \beta M_\infty^2 (A_1 b_1 + A_2 b_2)} \tag{A.3b}$$

$$K_{\bar{\alpha}_M} = \frac{A_3 b_4 + A_4 b_3}{b_3 b_4 (1 - M_\infty)} \tag{A.3c}$$

$$K_{q_M} = \frac{7}{15(1 - M_\infty) + 3\pi \beta M_\infty^2 b_5} \tag{A.3d}$$

where $A_3 = 1.5$, $A_4 = -0.5$, $b_3 = 0.25$, and $b_4 = 0.1$.

The total aerodynamic loads of attached flow can be written as

$$c_n^p = c_n^C + c_n^I \tag{A.4}$$

$$c_m^p = c_m^C + c_m^I \tag{A.5}$$

Superscript p denotes potential flow and presents the total load, normal force or moment, in unsteady attached flow conditions. The circulatory and impulsive load contributions in state space form can be represented as below [67]

$$c_n^C = c_{n_\alpha}\alpha_E \tag{A.6a}$$

$$c_n^I = \frac{4}{M_\infty}\dot{x}_3 + \frac{1}{M_\infty}\dot{x}_4 \tag{A.6b}$$

$$c_m^C = c_n^C\left(\frac{1}{4} - \frac{x_{ac}(M_\infty)}{c}\right) \tag{A.6c}$$

$$c_m^I = \frac{A_3}{M_\infty b_3 K_{\bar{\alpha}_M} T_I}x_5 + \frac{A_4}{M_\infty b_4 K_{\bar{\alpha}_M} T_I}x_6 - \frac{\pi}{16}\frac{U}{b}\beta x_7 - \frac{7}{12M_\infty}\dot{x}_8 - \frac{1}{M_\infty}\bar{\alpha} \tag{A.6d}$$

where α_E is an effective angle of attack in unsteady flow which can be written in the following form

$$\alpha_E = \beta^2\frac{U}{b}(A_1 b_1 x_1 + A_2 b_2 x_2) \tag{A.7}$$

In Eq. (A.6c), $x_{ac}(M_\infty)$ represents the aerodynamic center static position which is a function of Mach number. Moreover, c_{n_α} denotes the normal force coefficient curve slope against α during attached flow conditions. Considering small values of the angle of attack at attached flow, $c_{n_\alpha} = c_{l_\alpha}$, which is the classical lift curve slope. Since this slope is a function of Mach number, for each airfoil, it can be measured in static wind tunnel tests. However, an alternative way is to use the Prandtl-Glauert value as

$$c_{n_\alpha}(M_\infty) = \frac{2\pi}{\beta} \tag{A.8}$$

In addition, x_1 to x_8 represent aerodynamic states similar to the w_1 to w_6 states in Eq. (23) in Ref. [80]. Overall, for each of the exponential terms in Eq. (22) in Ref. [80] and Eqs. (A.1) and (A.2), there are eight aerodynamic states. Because of writing the compressibility and added

mass contributions to the aerodynamic loads means the impulsive loads in terms of step response functions, there is high number of aerodynamic states in compared to the one in Ref. [80]. In fact, in the Wagner model of Ref. [80], per each degree of freedom, there are only two aerodynamic states and there are no compressibility terms and the added mass terms appear as linear functions of the structural states. The Leishman-Beddoes aerodynamic states can be obtained by solving the following set of first order linear ordinary differential equations

$$\dot{x}_1 = -\frac{U}{b}\beta^2 b_1 x_1 + \bar{\alpha} + \frac{1}{2}q \tag{A.9a}$$

$$\dot{x}_2 = -\frac{U}{b}\beta^2 b_2 x_2 + \bar{\alpha} + \frac{1}{2}q \tag{A.9b}$$

$$\dot{x}_3 = -\frac{1}{K_{\bar{\alpha}} T_I} x_3 + \bar{\alpha} \tag{A.9c}$$

$$\dot{x}_4 = -\frac{1}{K_q T_I} x_4 + q \tag{A.9d}$$

$$\dot{x}_5 = -\frac{1}{b_3 K_{\bar{\alpha}_M} T_I} x_5 + \bar{\alpha} \tag{A.9e}$$

$$\dot{x}_6 = -\frac{1}{b_4 K_{\bar{\alpha}_M} T_I} x_6 + \bar{\alpha} \tag{A.9f}$$

$$\dot{x}_7 = -b_5 \frac{U}{b}\beta^2 x_7 + q \tag{A.9g}$$

$$\dot{x}_8 = -\frac{1}{K_{q_M} T_I} x_8 + q \tag{A.9h}$$

The potential aerodynamic force coefficients c_n^p and c_m^p can be obtained by combining Eqs. (A.4), (A.5) and (A.9) into a state space system as follows

$$\begin{cases} \dot{\mathbf{x}} = \boldsymbol{A}\mathbf{x} + \boldsymbol{B}\boldsymbol{u} \\ \boldsymbol{y}^p = \boldsymbol{C}\mathbf{x} + \boldsymbol{D}\boldsymbol{u} \end{cases} \tag{A.10}$$

where the kinematic variables $\bar{\alpha}(t)$ and $q(t)$ are inputs, $\mathbf{x} = [x_1 \quad x_2 \quad \cdots \quad x_8]^T$, $\mathbf{u} = [\bar{\alpha} \quad q]^T$ and $\mathbf{y}^p = [c_n^p \quad c_m^p]^T$. Furthermore, matrices $\boldsymbol{A}$, $\boldsymbol{B}$, $\boldsymbol{C}$, and $\boldsymbol{D}$ are defined as follows. Matrix $\boldsymbol{A}$ is a diagonal 8×8 matrix with the main diagonal components as

$$a_{11} = -\frac{U}{b}\beta^2 b_1 \tag{A.11a}$$

$$a_{22} = -\frac{U}{b}\beta^2 b_2 b_1 \tag{A.11b}$$

$$a_{33} = -\frac{1}{K_{\bar{\alpha}} T_I} b_1 \tag{A.11c}$$

$$a_{44} = -\frac{1}{K_q T_I} b_1 \tag{A.11d}$$

$$a_{55} = -\frac{1}{b_3 K_{\bar{\alpha}_M} T_I} b_1 \tag{A.11e}$$

$$a_{66} = -\frac{1}{b_4 K_{\bar{\alpha}_M} T_I} b_1 \tag{A.11f}$$

$$a_{77} = -b_5 \frac{U}{b}\beta^2 \tag{A.11g}$$

$$a_{88} = -\frac{1}{K_{q_M} T_I} \tag{A.11h}$$

matrix $\boldsymbol{B}$ is

$$\boldsymbol{B} = \begin{bmatrix} 1 & 1 & 1 & 0 & 1 & 1 & 0 & 0 \\ 0.5 & 0.5 & 0 & 1 & 0 & 0 & 1 & 1 \end{bmatrix} \tag{A.12}$$

matrix $\boldsymbol{C}$ is a 2×8 matrix with the components as

$$c_{11} = c_{n_\alpha}\beta^2 \frac{U}{b} A_1 b_1 \tag{A.13a}$$

$$c_{12} = c_{n_\alpha}\beta^2 \frac{U}{b} A_2 b_2 \tag{A.13b}$$

$$c_{13} = -\frac{4}{M_\infty K_\alpha T_I} \tag{A.13c}$$

$$c_{14} = -\frac{1}{M_\infty K_q T_I} \tag{A.13d}$$

$$c_{21} = c_{11}\left(\frac{1}{4} - \frac{x_{ac}(M_\infty)}{c}\right) \tag{A.13e}$$

$$c_{22} = c_{12}\left(\frac{1}{4} - \frac{x_{ac}(M_\infty)}{c}\right) \tag{A.13f}$$

$$c_{25} = \frac{A_3}{M_\infty b_3 K_{\bar{\alpha}_M} T_I} \tag{A.13g}$$

$$c_{26} = \frac{A_4}{M_\infty b_4 K_{\bar{\alpha}_M} T_I} \tag{A.13h}$$

$$c_{27} = -\frac{\pi}{16}\frac{U}{b}\beta \tag{A.13i}$$

$$c_{28} = \frac{7}{12 M_\infty K_q T_I} \tag{A.13k}$$

the remaining components of matrix $\boldsymbol{C}$ are zero. Finally, matrix $\boldsymbol{D}$ is a 2×2 with the following components.

$$\boldsymbol{D} = \begin{bmatrix} \frac{4}{M_\infty} & \frac{1}{M_\infty} \\ \frac{-1}{M_\infty} & \frac{-7}{12 M_\infty} \end{bmatrix} \tag{A.14}$$

In Eqs. (A.4) to (A.9), there is no airfoil-specific information except c_{n_α} as the lift curve slope. In the Leishman-Beddoes model, flow separation can be taken into account by considering contributions of leading edge and trailing edge separation and the leading edge vortex (LEV) to the aerodynamic loads. By comparing a critical normal force coefficient $c_{n_1}(M_\infty)$ to the potential normal force coefficient c_n^p, one can determine the leading edge separation onset. Due to stall delay in dynamic case leading to inaccuracy of direct comparison between $c_{n_1}(M_\infty)$ and c_n^p, a time-delayed version of c_n^p, x_9 is used in the Leishman-Beddoes model [64].

$$\dot{x}_9 = \frac{c_n^p(t) - x_9}{T_p} \tag{A.15}$$

In fact, Eq. (A.7) indicates that x_9 has time delay T_p to c_n^p. Thus, the leading edge separation criterion can add an additional state as $x_9(t) > c_{n_1}$ for the leading edge flow separation and $x_9(t) < c_{n_1}$ for the leading edge flow reattachment. To determine the value of critical normal force coefficient c_{n_1} and the time delay coefficient T_p, one needs to perform dynamic stall experiments for each Mach number and airfoil section. Although at very low Mach numbers,

the Leishman-Beddoes leading edge stall criterion cannot provide dynamic stall, a modified criterion for such flow speed was developed by Sheng et al. for wind turbine blades [66].

To determine trailing edge separation, one can use quasi-steady considerations. The static lift or normal force can be expressed by Kirchhoff theory as a function of the separation point chordwise position f. The following equation can be used to approximate this position.

$$f(\alpha) = \begin{cases} 1 - 0.3e^{(\alpha-\alpha_1)/S_1} & \text{if} \quad \alpha \leq \alpha_1 \\ 0.04 + 0.66e^{(\alpha_1-\alpha)/S_2} & \text{if} \quad \alpha > \alpha_1 \end{cases} \tag{A.16}$$

where α is the angle of attack in static form and S_1 and S_2 are constant values which need to be obtained for each airfoil and Mach number through a wind tunnel test. The second static angle of attack α_1 has $f = 0.7$, it means the separation point is located at $0.7c$. The angle α_1 is obtained through a static wind tunnel test. After having the separation point position for a given angle of attack, the corresponding lift coefficient can be calculated as

$$c_n(\alpha) = c_{n_\alpha}(M_\infty)\left(\frac{1+\sqrt{f}}{2}\right)^2 \tag{A.17}$$

In dynamic situations, in the Leishman-Beddoes model, the angle α in Eq. (A.12) is replaced by an effective angle of attack as follows

$$\alpha_f(t) = \frac{x_9(t)}{c_{n_\alpha}(M_\infty)} \tag{A.18}$$

To find the unsteady separation point position, one needs to substitute Eq. (A.10) into Eq. (A.12)

$$f(x_9) = \begin{cases} 1 - 0.3e^{\left(\frac{x_9(t)}{c_{n_\alpha}(M_\infty)} - \alpha_1\right)/S_1} & \text{if} \quad \dfrac{x_9(t)}{c_{n_\alpha}(M_\infty)} \leq \alpha_1 \\ 0.04 + 0.66e^{\left(\alpha_1 - \frac{x_9(t)}{c_{n_\alpha}(M_\infty)}\right)/S_2} & \text{if} \quad \dfrac{x_9(t)}{c_{n_\alpha}(M_\infty)} > \alpha_1 \end{cases} \tag{A.19}$$

This model creates an additional time delay to $f(x_9)$ to consider the unsteadiness effect of the boundary layer response. An additional state x_{10} needs to be considered to indicate the delayed unsteady separation point position

$$\dot{x}_{10} = \frac{f(x_9) - x_9}{T_f} \tag{A.20}$$

where T_f is additional time delay coefficient which needs to be obtained by dynamic wind tunnel tests. The corresponding normal force for the trailing edge separation point position can be calculated as

$$c_n^f(t) = c_n^c \left(\frac{1 + \sqrt{x_{10}}}{2} \right)^2 \tag{A.21}$$

where c_n^c is the potential flow normal force circulatory component in Eq. (A.6). The corresponding pitching moment of the trailing edge separation point position can be approximated by

$$c_m^f = (K_0 + K_1(1 - x_{10}) + K_2 \sin \pi x_{10}^{\kappa}) c_n^c \left(\frac{1 + \sqrt{x_{10}}}{2} \right)^2 \tag{A.22}$$

where K_0, K_1, K_2, and κ are coefficients related to the stall moment break shape, the pressure center position, and the aerodynamic center position. To determine all these coefficients, one needs to perform static wind tunnel tests. Having the LEV shedding can create extra lift and moment terms which can be represented by the LEV vorticity estimation in the Leishman-Beddoes model. This can be obtained by the difference between the circulatory lift forces in the attached and separated forms.

$$c_v = c_n^c - c_n^f = c_n^c \left(1 - \left(\frac{1 + \sqrt{x_{10}}}{2} \right)^2 \right) \tag{A.23}$$

This vorticity is only relevant after having leading edge separation. In other words, the value of this vorticity before separation is zero, $c_v = 0$. In order to have separation, $x_9(t) > c_{n_1}$, a time instance indicated by t_{v_0}. After passing T_{v_l} seconds, the LEV arrives the trailing edge; this time interval can be measured through dynamic wind tunnel tests.

The LEV lift can be proportional to the vorticity change rate $\dot{c}_v$ [68] as

$$\dot{c}_v = c_{n_\alpha}\frac{U}{b}\beta^2(A_1 b_1 \dot{x}_1 + A_2 b_2 \dot{x}_2)\left(1-\left(\frac{1+\sqrt{x_{10}}}{2}\right)^2\right)$$

$$-c_n^C\left(1+\frac{1}{\sqrt{x_{10}}}\right)\frac{\dot{x}_{10}}{4} \tag{A.24}$$

Though, in a constant time interval T_v called characteristic time constant, the vorticity can be dissipated hence, the vortex lift x_{11} is written in the following differential equation

$$\dot{x}_{11} = \begin{cases} \dot{c}_v - \dfrac{x_{11}}{T_v} & \text{if} \quad t - t_{v_0} \le 2T_{v_l} \\ -\dfrac{x_{11}}{T_v} & \text{if} \quad t - t_{v_0} > 2T_{v_l} \end{cases} \tag{A.25}$$

The LEV lift c_n^v and pitching moment c_m^v can be obtained from

$$c_n^v = x_{11} \tag{A.26}$$

$$c_m^v = \begin{cases} 0 & \text{if} \quad x_9 \le c_{n_1} \\ -0.25\left(1-\cos\pi\left(\dfrac{t-t_{v_0}}{T_{v_l}}\right)\right)x_{11} & \text{if} \quad t - t_{v_0} \le 2T_{v_l} \end{cases} \tag{A.27}$$

The final state in the Leishman-Beddoes model is x_{12} which shows a delayed version of the separation point $f(\bar{\alpha}(t))$ given by Eq. (A.12) and can be implemented to improve the pitching moment representation because of flow reattachment in trailing edge separation. That final state can be calculated by the following ordinary differential equation

$$\dot{x}_{12} = 2\frac{f(\bar{\alpha}(t)) - x_{12}}{T_f} \tag{A.28}$$

In Eq. (A.18), the pitching moment can be obtained by either x_{10} or x_{12} whichever has higher value

$$c_m^f = \begin{cases} (K_0 + K_1(1-x_{10}) + K_2\sin\pi x_{10}^\kappa)c_n^c\left(\dfrac{1+\sqrt{x_{10}}}{2}\right)^2 & \text{if} \quad x_{10} \ge x_{12} \\ (K_0 + K_1(1-x_{12}) + K_2\sin\pi x_{12}^\kappa)c_n^c\left(\dfrac{1+\sqrt{x_{12}}}{2}\right)^2 & \text{if} \quad x_{10} < x_{12} \end{cases} \tag{A.29}$$

Then at every time instance, the total lift and pitching moment are calculated as

$$c_n = c_n^f + c_n^v + c_n^I \tag{A.30a}$$

$$c_m = c_m^f + c_m^v + c_m^I + c_{m_0} \tag{A.30b}$$

where c_{m_0} is the pitching moment in zero lift. Having Eqs. (A.26) provides the complete Leishman-Beddoes dynamic stall model space equations. Equations (A.4), (A.6), (A.20), and (A.28) represent the state equations. The summary of all the states nature is given in Table A.1.

Table A.1 Leishman-Beddoes states summary

State	Nature
$x_1 - x_8$	Aerodynamic states for unsteady attached flow
x_9	Potential normal force coefficient time-delayed version c_n^p, when $x_9 > c_{n_1}$, there is leading edge separation
x_{10}	The unsteady trailing edge separation point chordwise position
x_{11}	The LEV lift
x_{12}	The quasi-steady separation point location time-delayed version, which can affect only the LEV pitching moment

The nonlinear state space equations are given as follows

$$\dot{\mathbf{x}} = \mathbf{f}(\mathbf{x}, \mathbf{u}) \tag{A.31}$$

$$\mathbf{y} = \mathbf{g}(\mathbf{x}, \mathbf{u}) \tag{A.32}$$

where $\mathbf{f}$ is a 12×1 nonlinear functions vector, $\mathbf{g}$ is a 2×1 nonlinear functions vector, $\mathbf{x} = [x_1 \quad x_2 \quad \cdots \quad x_{12}]^T$, $\mathbf{u} = [\bar{\alpha} \quad q]^T$ and $\mathbf{y} = [c_n \quad c_m]^T$. The Leishman-Beddoes model depends on 14 parameter values as $c_{n_\alpha}(M_\infty)$, α_1, S_1, S_2, K_0, K_1, K_2, c_{m_0}, c_{n_1}, κ, T_p, T_f, T_v and T_{v_l}. The value of these parameters can change according to the airfoil type and Mach number, so they need to be determined by wind tunnel test experiments. These values have been provided at different Mach numbers and a Reynolds number of 8×10^6 for the NACA 0012 airfoil by Leishman-Beddoes [69]. The parameter values for other airfoils can be found in the

literature. However, the attached flow parameters as A_1, b_1 and so on are constants therefore, they are independent from Mach number or the airfoil type. In the Leishman-Beddoes, the discontinuous LEV shedding process and the Kirchoff function for the separation point $f(\bar{\alpha})$ or $f(x_9)$ create the major nonlinearity. Since the Kirchoff function is discontinuous, Eqs. (A.16) and (A.18), the following discontinuity boundaries exist, as given in Table A.2.

Table A.2 Discontinuity Boundaries

Flow reattachment or stall onset	$x_9 = c_{n_1}$
Static lift curve break due to the unsteady separation point	$x_9/c_{n_\alpha}(M_\infty) = \alpha_1$
Static lift curve break due to the quasi steady separation point	$\bar{\alpha} = \alpha_1$
Time when having no effect of LEV	$t - t_{v_0} = 2T_{v_l}$
Crossing states x_{10} and x_{12}	$x_{10} = x_{12}$

A.2 Matrix coefficient for equations of motion

The matrix coefficient for the general form of the equations of motion, Eq. (7), can be given as follows

$$\boldsymbol{A} = \begin{bmatrix} I_\alpha & 0 \\ 0 & L_\alpha \end{bmatrix} \tag{A.33}$$

$$\boldsymbol{C} = \begin{bmatrix} C_\alpha & 0 \\ 0 & R_\alpha \end{bmatrix} \tag{A.34}$$

$$\boldsymbol{E} = \begin{bmatrix} K_\alpha & -\beta_\alpha \\ -\beta_\alpha(x_f - x_p) & \dfrac{1}{C_{p\alpha}} \end{bmatrix} \tag{A.35}$$

$$\boldsymbol{F} = \frac{1}{2}\rho U^2 c \begin{bmatrix} -c_n/\cos\alpha \\ cc_m + b(a + 1/2)c_n \end{bmatrix} \tag{A.36}$$

References

[1] Monteiro, T. P., Ramesh, K., Silvestre, F., and Silva, R. G. A., “Coupled framework for limit-cycle oscillations modeling based on leading-edge vortex shedding,” Journal of Fluids and Structures, 99 (2020) 103137.
https://doi.org/10.1016/j.jfluidstructs.2020.103137

[2] Silvestre, F. J., Guimarães Neto, A. B., Bertolin, R. M., Annes da Silva, R. G., and Paglione, P., “Aircraft control based on flexible aircraft dynamics,” Journal of Aircraft, Volume 54, Number 1, 2016.
https://doi.org/10.2514/1.C033834

[3] Theodorsen, T., 1935. General theory of aerodynamic instability and the mechanism of flutter. NACA Rept. 496.
https://ntrs.nasa.gov/citations/19930090935

[4] Theodorsen, T., Garrick, I. E., 1942. Flutter calculations in three degrees of freedom. NACA Rept. 741.
https://ntrs.nasa.gov/citations/19930090938

[5] Wagner, H., “Über die Entstehung des dynamischen Auftriebes von Tragflügeln,” ZaMM, 5 (1), 1925, 17–35.
https://doi.org/10.1002/zamm.19250050103

[6] Denegri, C. M., Dubben, J. A., Maxwell, D. L., “In-flight wing deformation characteristics during limit cycle oscillations,” Journal of Aircraft, 42 (2), 2005, 500–508.
https://doi.org/10.2514/1.1345

[7] Chen, Z., Shi, Z., Chen, S., and Yao, Z., “Stall flutter suppression of NACA 0012 airfoil based on steady blowing,” Journal of Fluids and Structures, 109, 2022, 103472.
https://doi.org/10.1016/j.jfluidstructs.2021.103472

[8] Bollay, W. and Brown, C. D., “Some experimental results on wing flutter,” Journal of Aeronautical Sciences, 8 (8), 1941, 313–318. https://doi.org/10.2514/8.10724

[9] Halfman, R. L., Johnson, H. C., and Haley, S. M., “Evaluation of High-Angle-of-Attack Aerodynamic-Derivative Data and Stall-Flutter Prediction Techniques,” NACA Technical Note TN 2533, 1951.

[10] Rainey, A. G., “Measurement of Aerodynamic Forces for Various Mean Angles of Attach on an Airfoil Oscillating in Pitch and on Two Finite-Span Wings Oscillating in Bending with Emphasis on Damping in the Stall,” NACA Technical Note TN 3643, 1956.

[11] Dimitriadis, G. and Li, J., “Bifurcation behavior of airfoil undergoing stall flutter oscillations in low-speed wind tunnel,” AIAA Journal, 47 (11), 2009, 2577–2596. https://doi.org/10.2514/1.39571

[12] Ramesh, K., Murua, J., and Gopalarathnam, A., “Limit-cycle oscillations in unsteady flows dominated by intermittent leading-edge vortex shedding,” Journal Fluids and Structure, 55, 2015, 84–105. https://doi.org/10.1016/j.jfluidstructs.2015.02.005

[13] Onoue, K., Song, A., Strom, B., Strom, B., and Breuer, K. S., “Large amplitude flow-induced oscillations and energy harvesting using a cyber–physical pitching plate,” Journal Fluids and Structure, 55, 2015, 262–275. https://doi.org/10.1016/j.jfluidstructs.2015.03.004

[14] Vasconcellos, R. M. G., Pereira, D. A., and Marques, F. D., “Characterization of nonlinear behavior of an airfoil under stall-induced pitching oscillations,” Journal of Sound and Vibration, 372, 2016, 283–298. https://doi.org/10.1016/j.jsv.2016.02.046

[15] McCroskey, W. J., Carr, L. W., and McAlister, K. W., “Dynamic stall experiments on oscillating airfoils,” AIAA Journal 14 (1), 1976, 57–63. https://doi.org/10.2514/3.61332

[16] McCroskey and W. J., “Unsteady airfoils,” Annual Review of Fluid Mechanics, 14, 1982, 285–311.

[17] Ericsson, L. E. and Reding, J. P., “Fluid mechanics of dynamic stall. Part I Unsteady flow concepts,” Journal of Fluids and Structure, 2 (1), 1988, 1–33. https://doi.org/10.1016/S0889-9746(88)90116-8

[18] Carr, L. W., “Progress in analysis and prediction of dynamic stall,” Journal of Aircraft, 25 (1), 1988, 6–17. https://doi.org/10.2514/3.45534

[19] Bhat, S. S. and Govardhan, R. N., “Stall flutter of NACA 0012 airfoil at low Reynolds numbers,” Journal Fluids and Structures, 41, 2013, 166–174. https://doi.org/10.1016/j.jfluidstructs.2013.04.001

[20] Wang, Z., Du, L., Zhao, J., Thompson, M. C., and Sun, X., “Flow-induced vibrations of a pitching and plunging airfoil,” Journal of Fluid Mechanics, 885, 2020, A36. https://doi.org/10.1017/jfm.2019.996

[21] Ekaterinaris, J. A. and Platzer, M. F., “Computational prediction of airfoil dynamic stall,” Progress in Aerospace Sciences, 33 (11–12), 1998, 759–846. https://doi.org/10.1016/S0376-0421(97)00012-2

[22] Le Pape, A., Costes, M., Richez, F., Joubert, G., David, F., and Deluc, J.-M., “Dynamic stall control using deployable leading-edge vortex generators,” AIAA Journal, 50 (10), 2012, 2135–2145. https://doi.org/10.2514/1.J051452

[23] Gerontakos, P. and Lee, T., “Dynamic stall flow control via a trailing-edge flap,”. AIAA Journal, 44 (3), 2006, 469–480. https://doi.org/10.2514/1.17263

[24] Tokumaru, P. and Dimotakis, P., “Rotary oscillation control of a cylinder wake,” Journal of Fluid Mechanics, 224, 1991, 77–90. https://doi.org/10.1017/S0022112091001659

[25] Palkin, E., Hadžiabdić, M., Mullyadzhanov, R., and Hanjalić, K., “Control of flow around a cylinder by rotary oscillations at a high subcritical Reynolds number,” Journal of Fluid Mechanics, 855, 2018, 236–266. https://doi.org/10.1017/jfm.2018.639

[26] Lin, J., Towfighi, J., and Rockwell, D., “Near-wake of a circular cylinder: control, by steady and unsteady surface injection,” Journal of Fluids Structures, 9 (6), 1995, 659–669. https://doi.org/10.1006/jfls.1995.1036

[27] Arcas, D. and Redekopp, L., “Aspects of wake vortex control through base blowing/suction,” Physics of Fluids, 16 (2), 2004, 452–456. https://doi.org/10.1063/1.1637354

[28] Amitay, M., Smith, B., and Glezer, A., “Aerodynamic flow control using synthetic jet technology,” In: 36th AIAA Aerospace Sciences Meeting and Exhibit, 1998, p. 208. https://doi.org/10.1007/978-3-540-36085-8_2

[29] Feng, L. H. and Wang, J. J., “Circular cylinder vortex-synchronization control with a synthetic jet positioned at the rear stagnation point,” Journal of Fluid Mechanics, 662, 2010, 232–259. https://doi.org/10.1017/S0022112010003174

[30] Cetiner, O. and Rockwell, D., “Streamwise oscillations of a cylinder in a steady current. Part 1. Locked-on states of vortex formation and loading,” Journal of Fluid Mechanics, 427, 2001, 1–28. https://doi.org/10.1017/S0022112000002214

[31] Carberry, J., Sheridan, J., and Rockwell, D., “Controlled oscillations of a cylinder: a new wake state,” Journal of Fluids Structures, 17 (2), 2003, 337–343. https://doi.org/10.1016/S0889-9746(02)00133-0

[32] Kim, J. and Choi, H., “Distributed forcing of flow over a circular cylinder,” Physics of Fluids, 17 (3), 2005, 033103. https://doi.org/10.1063/1.1850151

[33] Korkischko, I. and Meneghini, J., “Suppression of vortex-induced vibration using moving surface boundary-layer control,” Journal of Fluids and Structures, 34, 2012, 259–270. https://doi.org/10.1016/j.jfluidstructs.2012.05.010

[34] Zhu, H. and Gao, Y., “Vortex-induced vibration suppression of a main circular cylinder with two rotating control rods in its near wake: Effect of the rotation direction,” Journal of Fluids and Structures. 74, 2017, 469–491. https://doi.org/10.1016/j.jfluidstructs.2017.07.004

[35] He, J.-W., Glowinski, R., Metcalfe, R., Nordlander, A., and Periaux, J., “Active control and drag optimization for flow past a circular cylinder: I. Oscillatory cylinder rotation,” Journal of Computational Physics 163 (1), 2000, 83–117 https://doi.org/10.1006/jcph.2000.6556

[36] Homescu, C., Navon, I., and Li, Z., “Suppression of vortex shedding for flow around a circular cylinder using optimal control,” International Journal of Numerical Methods in Fluids, 38 (1), 2002, 43–69.

https://doi.org/10.1002/fld.203

[37] Yao, W. and Jaiman, R., "Feedback control of unstable flow and vortex-induced vibration using the eigensystem realization algorithm," Journal of Fluid Mechanics, 827, 2017, 394–414.
https://doi.org/10.1017/jfm.2017.470

[38] Camarri, S. and Iollo, A., "Feedback control of the vortex-shedding instability based on sensitivity analysis," Physics of Fluids, 22 (9), 2010, 094102.
https://doi.org/10.1063/1.3481148

[39] Jin, B., Illingworth, S. J., and Sandberg, R. D., "Feedback control of vortex shedding using a resolvent-based modelling approach," Journal of Fluid Mechanics, 897, 2020, A26.
https://doi.org/10.1017/jfm.2020.347

[40] Raissi, M., Wang, Z., Triantafyllou, M. S., and Karniadakis, G. E., "Deep learning of vortex-induced vibrations," Journal of Fluid Mechanics, 861, 2019, 119–137.
https://doi.org/10.1017/jfm.2018.872

[41] Ren, F., Wang, C., and Tang, H., "Active control of vortex-induced vibration of a circular cylinder using machine learning," Physics of Fluids, 31 (9), 2019, 093601.
https://doi.org/10.1063/1.5115258

[42] Chizfahm, A. and Jaiman, R., "Data-driven stability analysis and near-wake jet control for the vortex-induced vibration of a sphere," Physics of Fluids, 33 (4), 2021, 044104.
https://doi.org/10.1063/5.0044687

[43] Shih, W., Wang, C., Coles, D., and Roshko, A., "Experiments on flow past rough circular cylinders at large Reynolds numbers," Journal of Wind Engineering Industrial Aerodynamics, 49 (1–3), 1993, 351–368.
https://doi.org/10.1016/0167-6105(93)90030-R

[44] Gao, Y., Fu, S., Wang, J., Song, L., and Chen, Y., "Experimental study of the effects of surface roughness on the vortex-induced vibration response of a flexible cylinder," Ocean Engineering, 103, 2015, 40–54. https://doi.org/10.1016/j.oceaneng.2015.04.052

[45] Anderson, E. and Szewczyk, A., "Effects of a splitter plate on the near wake of a circular cylinder in 2 and 3-dimensional flow configurations," Experimental Fluids, 23 (2), 1997, 161–174. https://doi.org/10.1007/s003480050098

[46] Chehreh, B. B. and Javadi, K., "Flow control around a circular cylinder with swinging thin plates," Journal of Fluids and Structures, 81, 2018, 738–760. https://doi.org/10.1016/j.jfluidstructs.2018.06.010

[47] Sahu, T.R., Furquan, M., and Mittal, S., "Numerical study of flow-induced vibration of a circular cylinder with attached flexible splitter plate at low," Journal of Fluid Mechanics, 880, 2019, 551–593. https://doi.org/10.1017/jfm.2019.699

[48] Duan, F. and Wang, J., "Fluid–structure–sound interaction in noise reduction of a circular cylinder with flexible splitter plate," Journal of Fluid Mechanics, 920, 2021, A6. https://doi.org/10.1017/jfm.2021.403

[49] Hover, F., Tvedt, H., and Triantafyllou, M., "Vortex-induced vibrations of a cylinder with tripping wires," Journal of Fluid Mechanics, 448, 2001, 175–195. https://doi.org/10.1017/S0022112001005985

[50] Quadrante, L. A. R. and Nishi, Y., "Amplification/suppression of flow-induced motions of an elastically mounted circular cylinder by attaching tripping wires," Journal of Fluids and Structures, 48, 2014, 93–102. https://doi.org/10.1016/j.jfluidstructs.2014.02.018

[51] Lim, H. -C. and Lee, S. -J., “Flow control of circular cylinders with longitudinal grooved surfaces,” AIAA Journal, 40 (10), 2002, 2027–2036. https://doi.org/10.2514/2.1535

[52] Huang, S., “VIV suppression of a two-degree-of-freedom circular cylinder and drag reduction of a fixed circular cylinder by the use of helical grooves,” Journal of Fluids and Structures, 27 (7), 2011, 1124–1133. https://doi.org/10.1016/j.jfluidstructs.2011.07.005

[53] Law, Y. and Jaiman, R., “Passive control of vortex-induced vibration by spanwise grooves,” Journal of Fluids and Structures, 83, 2018, 1–26. https://doi.org/10.1016/j.jfluidstructs.2018.08.004

[54] Sui, J., Wang, J., Liang, S., and Tian, Q., “VIV suppression for a large mass-damping cylinder attached with helical strakes,” Journal of Fluids and Structures, 62, 2016, 125–146. https://doi.org/10.1016/j.jfluidstructs.2016.01.005

[55] Kumar, N., Kolahalam, V. K. V., Kantharaj, M., and Manda, S., “Suppression of vortex-induced vibrations using flexible shrouding—An experimental study,” Journal of Fluids Structures, 81, 2018, 479–491. https://doi.org/10.1016/j.jfluidstructs.2018.04.018

[56] Reddy T. S. R. and Kaza K. R. V., “A comparative study of some dynamic stall models,” Technical Memorandum TM 88917, NASA, 1987.

[57] Gangwani S. T., “Synthesized airfoil data method for prediction of dynamic stall and unsteady airloads,” Vertica 8, 1984, 93–118.

[58] Dunn P. and Dugundji J., “Nonlinear stall flutter and divergence analysis of cantilevered graphite/epoxy wings,” AIAA Journal, 30(1), 1992, 153–162. https://doi.org/10.2514/3.10895

[59] Price S. J. and Keleris J. P., “Non-linear dynamics of an airfoil forced to oscillate in dynamic stall,” Journal of Sound and Vibration, 194(2), 1996, 265–283.

[60] Tang D. M. and Dowell E. H., “Comments on the ONERA stall aerodynamic model and its impact on aeroelastic stability,” Journal of Fluids and Structures, 10, 1996, 353–366. https://doi.org/10.1006/jfls.1996.0023

[61] Li X. G. and Fleeter S., “Dynamic stall generated airfoil oscillations,” International Journal of Turbo and Jet Engines 20, 2003, 217–233.

[62] Laxman V. and Venkatesan C., “Chaotic response of an airfoil due to aeroelastic coupling and dynamic stall,” AIAA Journal, 45(1), 2007, 271–280. https://doi.org/10.2514/1.24587

[63] Sarkar S. and Bijl H., “Nonlinear aeroelastic behavior of an oscillating airfoil during stall-induced vibration,” Journal of Fluids and Structures, 24(6), 2008, 757–777. https://doi.org/10.1016/j.jfluidstructs.2007.11.004

[64] Galvanetto U., Peiró J., and Chantharasenawong C., “An assessment of some effects of the nonsmoothness of the leishman-beddoes dynamic stall model on the nonlinear dynamics of a typical aerofoil section,” Journal of Fluids and Structures 24(1), 2008, 151–163. https://doi.org/10.1016/j.jfluidstructs.2007.07.008

[65] Shao S., Zhu Q., Zhang C., and Ni X., “Airfoil aeroelastic flutter analysis based on modified leishman-beddoes model at low mach number,”. Chinese Journal of Aeronautics 24, 2011, 550–557. https://doi.org/10.1016/S1000-9361(11)60064-2

[66] Sheng W., Galbraith R. A. M., and Coton F. N., “A modified dynamic stall model for low mach numbers,” Journal of Solar Energy Engineering, 130(3), 2008, 031013. https://doi.org/10.1115/1.2931509

[67] Leishman J. G. and Beddoes T. S., “State-space representation of unsteady airfoil behaviour,” AIAA Journal, 28(5), 1990, 836–844.
https://doi.org/10.2514/3.25127

[68] Leishman J. G. and Crouse G. L. J., “State-space model for unsteady airfoil behaviour and dynamic stall,” Proceedings of the AIAA/AHS/ASME Structural Dynamics and Materials Conference, number AIAA 89-1319, 1989, Mobile, Alabama.
https://doi.org/10.2514/6.1989-1319

[69] Leishman J. G. and Beddoes T. S., “A generalized model for unsteady airfoil behaviour and dynamic stall using the indicial method,” Proceedings of the 42nd Annual Forum of the American Helicopter Society, Washington, DC., 1986.

[70] Dimitriadis G., Introduction to Nonlinear Aeroelasticity, Wiely: New Jersey, NJ, USA, 2017.
DOI:10.1002/9781118756478

[71] Lossouarn, B., Aucejo, M., Deü, J.-F., and Multon, B., “Design of inductors with high inductance values for resonant piezoelectric damping”, Sensors and Actuators A: Physical 259, 2017, 68-76.
https://doi.org/10.1016/j.sna.2017.03.030

[72] Moosavi R. and Faris E., “Smart Wing Flutter Suppression,” Designs, 6(2), 29, 2022.
https://doi.org/10.3390/designs6020029

[73] Moosavi R., “Smart Blade Flutter Alleviation with Rotational Effect,” Designs, 6(5), 98, 2022.
https://doi.org/10.3390/designs6050098

[74] Moosavi R., “Smart Blade Flutter Alleviation,” Engineering with Computers, 39(6), 2023, 3865–3876.
https://doi.org/10.1007/s00366-023-01832-9

[75] McAlister K. W., Pucci S. L., McCroskey W. J., and Carr L. W. “An experimental study of dynamic stall on advanced airfoil sections,” volume 2. pressure and force data. Technical Memorandum TM 84245, NASA, 1982.

[76] McCroskey W.J., “Inviscid flow field of an unsteady airfoil,” AIAA Journal, 11(8), 1973, 1130–1137.

[77] Ericsson L. E. and Reding J.P., “Unsteady flow concepts for dynamic stall analysis,” Journal of Aircraft 21(8), 1984, 601–606. https://doi.org/10.2514/3.45029

[78] Carr L. W., McAlister K. W., and McCroskey W. J., “Analysis of the development of dynamic stall based on oscillating airfoil experiments,” Technical Note TN D-8382, NASA, 1977.

[79] Chandrasekhara M. S., Wilder M. C., and Carr L. W., “Competing mechanisms of compressible dynamic stall,” AIAA Journal 36(3), 1998, 387–393. https://doi.org/10.2514/2.375

[80] Chantharasenawong C., “Nonlinear Aeroelastic Behaviour of Aerofoils Under Dynamic Stall,” PhD thesis, Imperial College London, 2007.